Light Propagation in Turbid and Condensed Media

by

Xiaohui Ni

A dissertation submitted to the Graduate Faculty in Physics in partial fulfillment of the requirements for the degree of Doctor of Philosophy,

The City University of New York

2006

UMI Number: 3204988

ProQuest Information and Learning Company
300 North Zeeb Road
P.O. Box 1346
Ann Arbor, MI 48106-1346

This manuscript has been read and accepted for the Graduate Faculty in Physics in satisfaction of the dissertation requirement for the degree of Doctor of Philosophy

Date	**Professor: R. R. Alfano** **Chair of Examining Committee**
Date	**Professor: Sultan Catto** **Executive Officer**

Supervisory Committee:

Dr. W. Cai (IUSL)

Prof. S. K. Gayen (Physics)

Prof. A. Gorokhovsky (physics)

Prof. J. L. Birman (Physics)

Dr. W. B. Wang (IUSL)

THE CITY UNIVERSITY OF NEW YORK

Abstract

LIGHT PROPAGATION IN TURBID AND CONDENSED MEDIA

by

Xiaohui Ni

Adviser: Professor R. R. Alfano

The goal of this thesis is to study scattering and transmission of ultrashort optical pulses in turbid and condensed media. Time-resolved polarization, Brillouin precursor propagation and the formation of periodic spatial filament distribution are discussed. Applications of the results of this research will be in medical imaging and free-space optical communications.

In this thesis, I first developed an analytical solution for the time-dependent polarized photon transport equation in a scattering medium using cumulant expansion. By terminating at the second order, I have derived an explicit expression of the polarized light distribution function. Our numerical time-resolved backscattering measurement and results presented a novel circular polarization memory effect in the backscattering from medium containing large size of particles. The application of polarization memory effect in imaging through turbid medium is demonstrated.

I also conducted experiments on ultrashort optical pulses propagation through scattering media. Time-resolved profiles of the transmitted light with parallel and perpendicular to incident polarization are simultaneously measured. Polarization analysis

was used to extract coded information buried within the multiple scattering profile from the early ballistic and snake components passing through the turbid medium.

Generation, propagation and attenuation of Brillouin precursor in a dielectric (dispersive and attenuative) medium described by Lorentz model are of interest since controlling of precursor could enhance medical imaging and also has significant applications for the military. I numerically evaluated the contribution of dispersion and absorption in the formation of Brillouin precursor and proposed a feasible way to observe it in THz region. We disproved a recent claim of observing optical precursor in water and gave an alternative explanation to the distortion of small overtone absorption band on optical pulse.

Nonlinear propagation of ultrafast laser pulse and supercontinuum (SC) generation in bulk materials are also been discussed. Periodic formation of ultraintense light filaments, which has markable transmission properties through optically dense media, are induced with diffraction component. Fringes and rings interference patterns are observed and contributed to the coherent properties of multiple supercontinuum sources.

Dedicated to my wife, Qiongyan Li

Acknowledgements

I am very grateful to my mentor Prof. Alfano for his patient guidance and rigorous training. Most of all to give me the opportunity to work directly with him and the independence he gave me to pursue these and other topics. He motive me to higher level, inspiring me that we can compete with the best researchers in the world. His professional knowledge, sense, especially his passion and ideas on science and technology have been the greatest help in the preparation of this thesis and wealth of knowledge for my future career.

I would like to take this opportunity to thank all the members in IUSL who have observed my mature from a new student to an accomplished researcher during this thesis. Especially thanks to Dr. W. Cai who guided me in the theoretical work. I thank Prof. Q. Xing, Ms. S. Kartazayeva, Mr. M. Alrubauee, Ms. X. Liang, Dr. W. Wang, Prof. S. Gayen, Mr. G. Tang for helping setting up experimental apparatus, and thank Dr. K. Sutkus, L. Gohara, X. Xin for help in preparing the thesis draft. I would like to thank the members of the Physics Department for their help. I thank Prof. J. Birman for useful discussion on light propagation through linear media.

I sincerely thank my family, especially my parents for their consistent support to my education under poor living condition. Without their sacrifices, I cannot complete my study.

This research was made possible from financial support provided in part by NASA, by New York State Science Technology and Academic Research, by Lockheed Martin Corporation, and by NASA University Research Center-Center for Optical Sensing and Imaging at City College of New York.

Light Scattering and Transmission from Various Media

Table of Contents

List of Figures

Chapter 1

Introduction

1.1 Introduction

Multiple scattering is a universal phenomenon. Everyday around us we see examples of multiple scattering of light in random media (for example milk, shaving cream, tooth paste, clouds, fog, white paper and refined sugar among others). Recently, there has been increased interest in the propagation of polarized light in randomly scattering media, such as biological tissues, because of its potential applications, particularly in biomedical imaging and diagnosis. Optical technology offers significant advantages for imaging human tissues because it employs nonionizing radiation and provides a high contrast between early cancers and the host normal tissues. However, the multiple scattering of light in biological tissues deteriorates the imaging resolution, which presents the main challenge associated with optical imaging. Even the single scattering problem has been exactly solved one century ago by Mie and others, the depolarization of light in a random medium is still not completely understood because of the complexity of vector wave multiple scattering. Propagation of light within turbid media has been modeled using the statistical method of Monte Carlo or “diffusion approximation” in highly scattering case. A more accurate analytical description for the scattering of linearly and circularly polarized light in random media is deserved. Techniques to overcome the effect of the multiple scattering on image or signal quality are expected.

1.2 Thesis statement

In this thesis, I studied time-resolved polarization of optical pulses propagation and scattering in turbid media. The efficiency of linearly and circularly polarized light in imaging a target inside a turbid medium is investigated. My experimental results showed that the circularly polarized light can image deeper than linearly polarized light for suspensions containing large size of particles. Analytical solution to transport equation is formulated to quantitatively describe the polarized light scattering. Spatial gating, polarization gating and polarization analysis techniques are used to extract the early ballistic and snake-like light components from the diffusive components for the potential application of wireless optical communication.

Pulse propagation through linear (dielectric-like) media was investigated in the thesis. The formation and algebra attenuation (z^{-n}) of Brillouin precursor will be discussed. The distortion of optical pulse by the overtone absorption band in water is observed.

Next I presented the controlled generation of spatial filaments and supercontinuum by Fresnel diffraction.

The thesis describes pulse propagation in various types of media (scattering, linear, and nonlinear). The purpose of this thesis is to understand how optical signals can penetrate deeper into media. Free-space communications, medical imaging as well as military and homeland security applications will benefit from the outcome of knowledge learned from this thesis.

1.3 Background

1.3.1 Rayleigh Scattering-Mie Scattering –diffraction-geometrical optics

One of the most important examples of interaction at the microscopic scale is the phenomenon of light scattering, which small particles suspended in a medium of a different index of refraction diffuse a portion of the incident radiation in various directions. It is of such great importance in optics that Mark P. Silvrman wrote that, "virtually every aspect of physical optics is an example of light scattering"[1]. Logan [2] provided an excellent survey of history of early studies of the scattering of plane waves by a sphere. Emphasis by Logan is placed upon the relatively unknown contributions of Clebsch, Lorenz, Nicholson, Bromwich, Proudman, Doodson, Kennedy and White.

In my study of light propagation and scattering in turbid media, the scattered light has same frequency as the incident light, a process referred to as elastic scattering. Elastic light scattering theory may be categorized in three different types: Rayleigh scattering, Mie scattering, and non-selective scattering. The size of scattering particle in comparison with the incident wavelength λ is a key parameter. Small and large particles give rise to different and interesting effects. Fig.1.1 shows the scattered light intensity distribution for different sizes of particles. The scattering from small particle is mostly uniform. However, for the particle size comparable or larger than the incident wavelength, the light is more forwardly scattered.

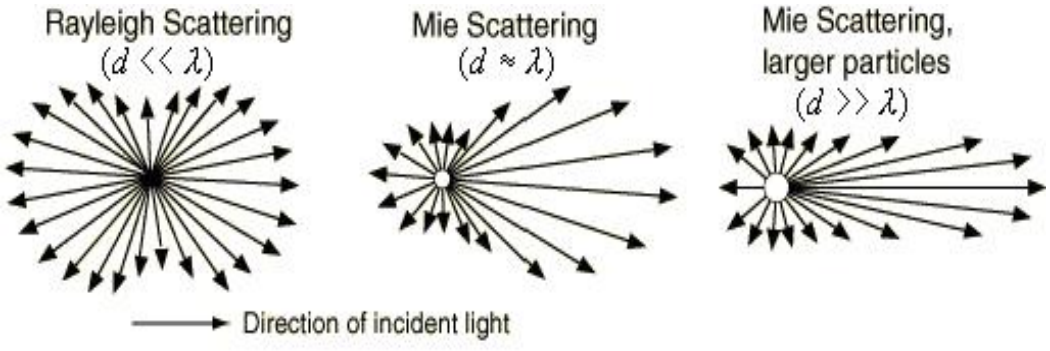

Fig. 1.1 Scattering by different sizes of particles

Rayleigh scattering [3] occurs when the particles causing the scattering are much smaller in size than the wavelengths of the light. The criteria for Rayleigh scattering is that $x << 1$ and $|m|x << 1$, where m is the relative refraction index and x is the size parameter given by

$$x = \frac{2\pi a}{\lambda} \tag{1.1}$$

where a is the spherical particle radius, and λ is the wavelength in the medium.

Rayleigh scattering is wavelength dependent. As the wavelength decreases, scattering increases:

$$I = I_0 \frac{8\pi^4 N\alpha^2}{\lambda^4 R^2}\left(1+\cos^2\theta\right) \quad \propto \quad \frac{1}{\lambda^4} \tag{1.2}$$

The strong wavelength dependence of the scattering ($\sim\lambda^{-4}$) means the blue light is scattered much more strongly than the red light, this is the reason why the sky is blue.

Scattering from particles of about the same size as the wavelength is handled by Mie theory. *Mie theory* also called *Lorenz-Mie theory* is a complete mathematical-physical theory of the scattering of electromagnetic wave by spherical particles, developed by Gustav Mie in 1908 [4]. As an exact solution to the scattering of a plane electromagnetic wave by a dielectric sphere, Mie scattering has no size limitations and may be used for describing most spherical particle systems, including Rayleigh scattering. The modern way to formulate the Mie theory has been outlined by Stratton [5]. In this theory the incident plane wave as well as the scattering field is expanded into radiating spherical vector wave functions. The internal field is expanded into regular spherical vector wave

functions. By enforcing the boundary condition on the spherical surface, the expansion coefficients of the scattered field can be computed.

The Mie solution, given in the form of an infinite series, has a limitation in that it converges very slowly when the radius of the sphere exceeds a few wavelengths. The problem of backscattering is further complicated by the waves existing inside the sphere which could contribute significantly. Among studies on large spheres, a practical development is due to the modified geometrical optics method introduced by Thomas [6]. Based in part on this method, Atlas and Glover [7] derived approximate expressions for backscattered fields and suggested that front and rear axial returns and glory ray are sufficient to account for the total scattered field. Kouyoumjian *et al.* [8] have also applied the modified geometrical optics method to include the contribution of stationary ray (rainbow ray) in the backscattered field. However, It was Inada *et al.*[9,10,11] applied the Watson transformation [12] to the exact Mie series and took the residue contributions into account. In their approach, they derived explicitly the backscattering fields as a sum of geometric optics and diffracted fields. The geometric optics fields which include front and rear axial returns, glory ray and rainbow rays, come from the illuminated region of the sphere. The diffracted fields can be evaluated by finding the poles of the intergrand, and computing the residues. The residue contributions are physically connected with two different types of surface waves; one type is a “creeping wave” analogous to that of a perfectly conducting sphere, which encircles the dielectric sphere, and the other type is a wave which enters the sphere and then emerges as a surface wave. The latter is unique to a dielectric sphere.

Mie theory, a rigorous method, while providing accurate results, does not lead to an understanding of the physical phenomena or scattering from other than spherical shapes as geometrical optics and diffracted fields. Fig.1.2 shows a physical model of scattering by dielectric sphere based on the diffraction-geometrical optics.

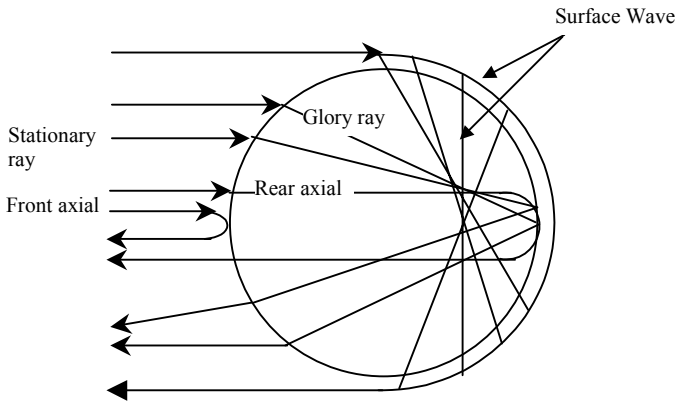

Fig.1.2 Schematic illustration of different scattering mechanism for a large sphere

In Fig.1.2, we just show one reflection inside the sphere for glory ray, there also exists two or more reflection (short cuts). Glory is usually observed as a bright and often colorful halo in the backscattered sunlight from water droplets; it is frequently seen around the shadow of an airplane flying above cloud.

We will discuss the scattering of an optical pulse based partly on Mie theory in this thesis. An interesting question is what happens to the scattering of ultafshort pulse from a sphere based on geometrical optics. It has been recognized since the 1950s that the late time response to an impulse signal provides an intuitive and potentially simple way to identify targets [14,15]. Cheville, etc [16,17] have measured the delayed response associated with the creeping wave on the cylinder and have thereby determined that the propagation velocity is c, the velocity of light in free-space. The relatively short wavelengths of the THz pulse permit target features of less 1 mm to be observed, making

this technique ideal for ranging measurements. It is the first direct time-domain confirmation of the applicability of diffraction-geometrical optics approximations for the propagation of creeping waves external to the dielectric cylinder. Prof. Alfano suggested that we may observe the self-phase-modulation (SPM) [18] in the creeping wave from a glass ball, this idea is deserved to be explored.

1.3.2 Mie theory and polarization parameters

In this section, we present a brief account of the Mie solution for the convenience of later chapters. More detailed derivations are found in many standard textbooks [19,20,21,22].

Considering a light beam impinging on a spherical particle along a direction **S**, we choose a reference plane through the direction of propagation. The electric field vector is represented by:

$$\vec{E} = \mathrm{Re}\left[E_l \vec{l} + E_r \vec{r}\right] \tag{1.3}$$

where $\mathbf{E}_l = a_1 \exp(i\delta_1)$, the component parallel to the reference plane ($E_{\|}$) , and $\mathbf{E}_r = a_2 \exp(i\delta_2)$, the component perpendicular to the reference plane ($E_{\perp}$). Four real components I, Q, U, V were introduced by Stokes[23] and represented by:

$$\mathbf{I} = \begin{pmatrix} I \\ Q \\ U \\ V \end{pmatrix} \tag{1.4}$$

The component ***I*** is the total intensity:

$$I = |a_1|^2 + |a_2|^2 = E_l E_l^* + E_r E_r^* = |E_{\|}|^2 + |E_{\perp}|^2 \tag{1.4a}$$

The component ***Q*** describe a linear polarization:

$$Q = a_1^2 - a_2^2 = E_l E_l^{\,*} - E_r E_r^{\,*} = \left|E_{\|}\right|^2 - \left|E_{\perp}\right|^2 \tag{1.4b}$$

The component ***U*** describes a linear polarization 45^o relative to the reference plane:

$$U = 2a_1 a_2 \cos\delta = E_l E_r^{\,*} + E_r E_l^{\,*} = \left|E\left(45^0\right)\right|^2 - \left|E\left(-45^0\right)\right|^2 \tag{1.4c}$$

where

$$E\left(\pm 45^0\right) = \left(E_{\|} \pm E_{\perp}\right)/\sqrt{2}$$

The last component ***V*** is the difference between the intensities of the right- and left-handed circularly polarized light.

$$V = 2a_1 a_2 \sin\delta = i\left(E_l E_r^{\,*} - E_r E_l^{\,*}\right) = \left|E_R\right|^2 - \left|E_L\right|^2 \tag{1.4d}$$

where the right- and left-circular components of field are

$$E_L = \left(E_{\|} + iE_{\perp}\right)/\sqrt{2} \qquad E_R = \left(E_{\|} - E_{\perp}\right)/\sqrt{2}$$

In Eq. (1.4), $\delta = \delta_1 - \delta_2$.

The Stokes parameters are real numbers and satisfy the relation:

$$I^2 \geq Q^2 + U^2 + V^2 \tag{1.5}$$

To give further physical meaning to these Stokes symbols, we note that **I** = [1 0 0 0], where

$$Q = U = V = 0$$

represents the case of unpolarized light.

The vector **I** = [1 0 0 1], where

$$Q = U = 0,\ V = 1$$

represents right-handed circularly polarized light.

The parallel, perpendicular, right-handed (RH), left-handed (LH) circularly polarized light is represented using Stokes parameter as:

$$I_{\parallel} = (I+Q)/2, \quad I_{\perp} = (I-Q)/2, \quad I_R = (I+V)/2, \quad I_L = (I-V)/2 \qquad (1.6)$$

The remaining degree of linear and circular polarization P_l and P_c, respectively, are defined with Stokes parameters as

$$P_l = \frac{I_{\parallel}}{I} = \frac{I+Q}{2I} \quad , \quad P_c = \frac{I_R}{I} = \frac{I+V}{2I} \qquad (1.7)$$

Based on these notations (Equ.1.1-1.7), we first described the scattering of electric vector $\mathbf{E}_l$, $\mathbf{E}_r$ by a sphere using amplitude function **S**, then we gave an expression with **S** for the elements of scattering phase matrix, which described the scattering of the Stokes parameters by a sphere.

In the far-field zone (i.e., at the large distance r from a sphere), the solution of the vector wave equation can be obtained as

$$\begin{bmatrix} E_l^s \\ E_r^s \end{bmatrix} = \frac{\exp(-ikr+ikz)}{ikr} \begin{bmatrix} S_2 & S_3 \\ S_4 & S_1 \end{bmatrix} \begin{bmatrix} E_l^i \\ E_r^i \end{bmatrix} \qquad (1.8)$$

The scattering matrix describes the relation between incident and scattered electric field component perpendicular and parallel the scattering plane. The four amplitude function, S_1, S_2, S_3, and S_4, all functions of θ (scattering angle) and φ (azimuth angle), form the scattering matrix **S**(θ, φ) of four element. It is a fundamental equation of scattered radiation including polarization in the far field.

For spheres, the non-diagonal scattering amplitude functions $S_3 = S_4 = 0$. Thus, for spheres it reduces to

$$\begin{bmatrix} E_l^s \\ E_r^s \end{bmatrix} = \frac{\exp(-ikr+ikz)}{ikr} \begin{bmatrix} S_2 & 0 \\ 0 & S_1 \end{bmatrix} \begin{bmatrix} E_l^i \\ E_r^i \end{bmatrix} \qquad (1.9)$$

where exp(*ikz*) is the incident plane wave, and $\frac{\exp(-ikr)}{ikr}$ is the outgoing scattered wave.

The amplitude functions S_1 and S_2 depend only on the scattering angle

$$S_1(\theta)=\sum_{n=1}^{\infty}\frac{2n+1}{n(n+1)}\left[a_n\pi_n(\cos\theta)+b_n\tau_n(\cos\theta)\right] \tag{1.10}$$

$$S_2(\theta)=\sum_{n=1}^{\infty}\frac{2n+1}{n(n+1)}\left[b_n\pi_n(\cos\theta)+a_n\tau_n(\cos\theta)\right] \tag{1.11}$$

where π_n and τ_n are Mie angular functions

$$\pi_n(\cos\theta)=\frac{1}{\sin(\theta)}P_n^1(\cos\theta) \tag{1.12}$$

$$\tau_n(\cos\theta)=\frac{d}{d\theta}P_n^1(\cos\theta) \tag{1.13}$$

where P_n^1 are the associated polynomials.

The coefficients a_n are related to the amplitudes of the electric oscillations, while the coefficients b_n are related to the amplitudes of the oscillations of a magnetic type.[5, p415]

$$a_n=\frac{m\psi_n(mx)\psi_n'(x)-\psi_n(x)\psi_n'(mx)}{m\psi_n(mx)\xi_n'(x)-\xi_n(x)\psi_n'(mx)} \tag{1.14}$$

$$b_n=\frac{m\psi_n(x)\psi_n'(mx)-\psi_n(mx)\psi_n'(x)}{m\xi_n(x)\psi_n'(mx)-\psi_n(mx)\xi_n'(x)} \tag{1.15}$$

where $x=ka=2\pi a/\lambda$, a is the radius of the sphere, k is the propagation constant in free space, m is the refractive index of the sphere material relative to its surrounding medium. Ψ and ξ are defined as:

$$\psi_n(z) = zj_n(z) \quad \text{and} \quad \xi_n(z) = zh_n^{(2)}(z)$$

where j_n is the Bessel function and $h_n^{(2)}$ is the spherical Bessel function.

The scattering cross section σ_s is given by

$$\sigma_s = \frac{2\pi}{k^2}\sum_{n=1}^{\infty}(2n+1)\left(|a_n|^2 + |b_n|^2\right) \tag{1.16}$$

The anisotropic scattering of light by an particle can be characterized by an anisotropic factor g, which is the mean cosine of the scattering directions [g in (-1,1) g<0: backward scattering g>0: forward scattering g=0:isotropic scattering]

$$g = \langle \cos\theta \rangle = \frac{\int_{4\pi} p(\theta,\varphi)\cos\theta d\Omega}{\int_{4\pi} p(\theta,\varphi) d\Omega} \tag{1.17}$$

where $p(\theta, \varphi)$ is the phase function, which is the probability of light being scattered in the direction (θ, φ) by a scatter. The phase function is a measure of the anisotropy of the scattering. It provides a factor for each direction with which the incoming intensity has to be multiplied to give the outgoing intensity. Hence, for isotropic scattering, the phase function $p = 1$ for all directions.

In many practical cases, the following Henyey-Greenstein formula gives a good approximation for the phase function.

$$p(g,\theta) = \frac{1-g^2}{\left(1+g^2-2g\cos(\theta)\right)^{2/3}} \tag{1.18}$$

The original introduction of the Henyey-Greenstein (H-G) phase function, is used to describe scattering by interstellar gas and dust [24]. The H-G phase function turns out to be very general, and is used to describe photon scattering in many media by late authors.

The properties of light scattering by a random media are characterized by three key length parameters: the scattering mean free path l_s, the transport mean free path l_t, and the absorption length l_a. l_s is the mean distance between scatterings

$$l_s = 1 \Big/ (n\sigma_s) \tag{1.19}$$

where n is the number density of the scatterer in the medium. The

$$l_t = l_s \Big/ (1-g) \tag{1.20}$$

describes the average distance photons travel before deviating significantly from their orignal direction of propagation.

The Stokes parameters uniquely characterize the electromagnetic waves. Let $\boldsymbol{I}_0$, $\boldsymbol{Q}_0$, $\boldsymbol{U}_0$, $\boldsymbol{V}_0$ be the Stokes parameters of the incident field and I, Q, U, V be the Stokes parameters of scattered radiation

$$\begin{bmatrix} I \\ Q \\ U \\ V \end{bmatrix} = \frac{\sigma_s}{4\pi r^2} P \begin{bmatrix} I_0 \\ Q_0 \\ U_0 \\ V_0 \end{bmatrix} \tag{1.21}$$

where $\boldsymbol{P}$ is the scattering phase matrix.

In general, for a particle of any shape, the scattering phase matrix consists of 16 independent elements, but for a sphere, this number reduces to four [19]. For spheres,

$$\begin{bmatrix} I \\ Q \\ U \\ V \end{bmatrix} = \frac{\sigma_s}{4\pi r^2} \begin{bmatrix} P_{11} & P_{12} & 0 & 0 \\ P_{12} & P_{11} & 0 & 0 \\ 0 & 0 & P_{33} & -P_{34} \\ 0 & 0 & P_{34} & P_{33} \end{bmatrix} \begin{bmatrix} I_0 \\ Q_0 \\ U_0 \\ V_0 \end{bmatrix} \tag{1.22}$$

where each element of the scattering phase matrix is expressed via the scattering amplitude $S_1(\theta)$ and $S_2(\theta)$.

$$P_{11} = \frac{2\pi}{k^2 \sigma_s}\left[S_1 S_1^{*} + S_2 S_2^{*}\right] \tag{1.23a}$$

$$P_{12} = \frac{2\pi}{k^2 \sigma_s}\left[S_2 S_2^{*} - S_1 S_1^{*}\right] \tag{1.23b}$$

$$P_{33} = \frac{2\pi}{k^2 \sigma_s}\left[S_2 S_1^{*} + S_1 S_2^{*}\right] \tag{1.23c}$$

$$-P_{34} = \frac{2\pi}{k^2 \sigma_s}\left[S_1 S_2^{*} - S_2 S_1^{*}\right] \tag{1.23d}$$

The problem of determining the scattering properties of polarized light experimentally is made more tractable by considering not the transformation of electric fields, but that of the Stokes parameters in Equ.(1.22). By making measurement to determine the four independent elements (P_{11}, P_{12}, P_{33}, P_{34}), the scattering of polarized light by single spherical particle is completely characterized. In the other hand, computation of the single scattering of polarized light is made simple by calculating the four independent scattering phase matrix elements according to Equ.1.23(a)-(d). In chapter 2, we will expand the scattering phase matrix ***P*** by general spherical function. In chapter 3, we will use formula 1.21(a)-(d) to calculate the angular distribution of scattered circularly polarized light for different particle sizes (see Fig.3.4 in chapter 3).

1.3.3 Diffusion Equation

Light scattering in turbid media can be described by wave theory, which starts with Maxwell's equation, or transport theory, which deals directly with the transport of power through turbid media. Because the mathematical complexities of wave equation, transport theory has now been widely used to describe light scattering in random media. Before a detail description of transport theory in the late chapter, we review the diffusion

approximation of the transport theory for a highly scattering medium The "diffusion approximation" is now well established for modeling the light propagation in highly scattering and absorption media. The essential approximation underlying the diffusion approach is that after going through a large number of scattering events the phases of the scattered waves are randomized so that any interference effects in the medium can be neglected. As a result, only the light intensity needs to be considered in the description of light propagation [25]. The diffuse light intensity of a pulse is given by the following diffusion equation[26][27][28]

$$\frac{\partial I(r,t)}{\partial t} = \nabla\left(D\nabla I(r,t)\right) - \nu\mu_a I(r,t) + q^{(0)}(r,t) \tag{1.24}$$

where $q^{(0)}(\mathbf{r},t) = \delta(\mathbf{r})\delta(t)$ represent the impulse incident source at t = 0 and position $\mathbf{r} = 0$. $D = \nu/[3\mu_s(1-g)]$ is the diffusion coefficient (see cai's argument about this constant[29]), and ν is the speed of light in the scattering medium. The transmitted pulse can be described by the solution of diffusion Eq.(1.24) for the slab geometry, the solution is given by [30]

$$I_z(t) = \frac{1}{4d^2 t}\sum_{m=1}^{\infty} m \sin\left(\frac{m\pi z}{d}\right)\exp\left[-Dt\left(\frac{m\pi}{d}\right)^2\right]\exp\left(\frac{-\nu t}{l_a}\right) \tag{1.25}$$

where $d = z + 2z_0$, $z_0 = 0.71 l_{tr}$ is the extrapolation length, and z is the thickness of the slab. In obtaining the above solution, perfectly absorbing boundary conditions at the extrapolated surfaces are used in Equ.(1.24). The transport length and the absorption length can be calculated by numerically fitting the experimental temporal profile to Equ.(1.24) [31][32].

The diffusion equation describes the diffuse wave in space; but it cannot describe the early part of the scattered pulse profile [one need 10 l_t at least to be described by DA (33)]. It can be an excellent approximation for large z / l_t [33] and smaller g factor [25]. An analytic solution for the scalar transport equation has been developed by Cai [34,35] which provided a more accurate description of photon distribution in space as well as photon velocity direction. In next chapter, we will study the time-resolved polarized light transport equation.

References:

1. M. P. Silverman, *Waves and grains* (Princeton U.P., Princeton, NJ,1998) pp.288.
2. Nelson A. Logan, *Survey of some early studies of the scattering of plane waves by a sphere*, Selected papers on light scattering, Milton Kerker, editor, 3 (1988).
3. L. Rayleigh, Phil. Mag. **41**, 447 (1871).
4. G. Mie, Ann. Phys. **25**, 377 (1908).
5. J. A. Stratton, *Electromagnetic Theory* (McGraw-Hill, New York, 1941).
6. D. T. Thomas, "Scattering by plasma and dielectric bodies", Ph.D. dissertation, Ohio State University, Columbus, Antenna Lab. Rept., no. 1116 (1962).
7. D. Atlas and K. M. Glover, "Backscattering by dielectric spheres with and without metal caps", Proc. Inter-Disciplinary Conf. Electromagnetic scattering (Potsdam, N. Y., 1962).
8. R. G. Kouyoumjian, L. Peters, Jr., and D. T. Thomas, IEEE Trans. Ant. Prop., AP-**11**, 690 (1963).
9. H. Inada, Appl. Opt. **13**, 1928 (1974).
10. H. Inada, Appl. Opt. **12**, 1516 (1973).
11. H. Inada, M. A. Plonus, IEEE Trans. Ant. Prop. **AP-18**, 89 (1970).
12. G. N. Watson, Proc. Roy. Soc. London, **A95**, 83 (1918).
13. H. Inada, M. A. Plonus, IEEE Trans. Ant. Prop. **AP-18**, 649 (1970).
14. P. S. Ray and J. J. Stephens, Radio Sci. **9**, 43 (1974).
15. J. Rheinstein, IEEE Trans. Ant. Prop. **AP-16**, 89 (1968).
16. R. A. Chevile and D. Grischkowsky, Appl. Phys. Lett. **67**, 1960 (1995) .

17. R. A. Cheville, R. W. McGowan, and D. R. Grischkowsky, IEEE Trans. Ant. Prop. **45**, 1518 (1997).

18. R. R. Alfano and S. L. Shapiro, Phys. Rev. Lett. **24**, 592 (1970).

19. H. C. van de Hulst, *Light scattering by small particles* (Dover, New York, 1981).

20. M. Kerker, *The scattering of light and other electromagnetic radiation* (Academic, New York, 1969).

21. F. Bohren, D. R. Huffmann, *Absorption and scattering of light by small particles* (Wiley-Innterscience, New York, 1983).

22. M. I. Mishchenko, L. D. Travis, and A. A. Lacis, *Scattering, Absorption, and Emission of light by Small Particles* (Cambridge University Press, UK, 2002).

23. G. C. Stokes, Trans. Cambridge Philos. Soc. **9**, 399 (1852).

24. L. G. Henyey, J. L. Greenstein, The Astrophysical Journal, **93**, 70 (1941).

25. A. Ishimaru, Appl. Opt. **28**, 2210 (1989).

26. A. Ishimaru, *Theory and application of wave propagation in random media* (NJ:IEEE Press, Piscataway, 1997).

27. P. M. Morse and H. Feshbach, *Methods of the theoretical physics* (McGraw-Hill, New York, 1953).

28. J. Crank, *The mathematics of diffusion* (Clarendon Press, Oxford, 1956).

29. W. Cai, M. Xu, M. Lax, and R. R. Alfano, Opt. Lett. **27**, 731 (2002).

30. M. Lax, V. Narayanamurti, and R. C. Fulton, "Classical diffusive photon transport in a slab", in Proc. Symp. on Laser Optics and Condensed Matter, Leningrad, June 1987, edited by J. L. Birman and H. Z. Cummins (Plenum, New York) pp.229.

31. R. Garg, R. K. Prud'homme, A. Aksay, F. Liu, and R. R. Alfano, J. Opt. Soc. Am. A **15**, 932 (1998).

32. R. Garg, R. K. Prud'homme, A. Aksay, F. Liu, and R. R. Alfano, J. Mater. Res. **13**, 3463 (1998).

33. K. M. Yoo, F. Liu, and R. R. Alfano, Phys. Rev. Lett. **64**, 2647 (1990).

34. W. Cai, M. Lax, and R. R. Alfano, Phys. Rev. E **61**, 3871 (2000).

35. W. Cai, M. Xu, and R. R. Alfano, Phys. Rev. E **71**, 041202 (2005).

Chapter 2

Theoretical Study of Polarized Light Transport in Random Media

2.1 Introduction

Understanding polarization phenomenon in a multiple scattering medium is important because of its possible applications in biomedical media [1,2,3,4], cloud monitoring [5], and communications [6]. A theoretical understanding of propagation of polarized light in scattering media became practically important. This subject has been investigated for many years since the polarized photon transport equation (PPTE) was formulated by Gans [7] and Chandrasekhar[8]. To my knowledge, a numerical solution of the PPTE by Chebyshev spectral method has just been obtained by Kim [9] with certain approximation. Monte-Carlo simulation is still the main tool of choice in recent theoretical investigation of light polarization in multiple scattering media [4,10].

In this section, we presented a new method to obtain an analytical solution of the time-dependent PPTE in an infinite uniform medium using a circular representation of the polarized light and cumulant expansion.

The cumulant expansion has been developed by W. Cai at CCNY to describe polarized photon transport equation [11,12,13]. The solution is expressed in the angular distribution $\boldsymbol{F}(\mathbf{s},t)$, the first cumulants (the center of the distribution), the second cumulant (half-width of the spread of the distribution), and an Gaussian polarized photon spatial distribution $\boldsymbol{I}(\boldsymbol{r},\boldsymbol{s},t)$ as function of position $\boldsymbol{r}$, light direction $\mathbf{s}$, and time t.

Section 2.2 is an extension of the theoretical derivation based on W. Cai's previous theoretical work[12]. Section.2.3 presents our recent numerical calculation of the

backscattering of the circularly polarized light based on the analytical expression obtained in Section 2.2. Polarization memory of circularly polarized light is predicted from our calculation and its physical explanation and application will be discussed in the late chapter.

2.2 Analytical solution of the polarized photon transport equation

In Stokes representation (SP), the polarized light is described by a 4 components vector $\mathbf{I}^{SP} = [I,Q,U,V]$ (see chapter 1.3). In this section, we gave an analytical expression of the parallel component $I_{\parallel} = (I + Q)/2$, the perpendicular component $I_{\perp} = (I - Q)/2$, the right-handed circular polarization $I_R = (I + V)/2$, and the left-handed circular polarization $I_L = (I - V)/2$ (see chapter 1, section 1.3 for detail defination of I, Q, U, V, $I_{\parallel}$, $I_{\perp}$, I_R, I_L) for polarized light backscattered from a turbid medium.

The transport equation for the polarized photon distribution function $\mathbf{I}(\mathbf{r},\mathbf{s},t)$ in an infinite uniform medium, from a point pulse light source, $\mathbf{I}^{(0)}\delta(\mathbf{r}-\mathbf{r}_0)\delta(\mathbf{s}-\mathbf{s}_0)\delta(t-0)$ is given by

$$\begin{aligned} &\partial I^{SP}(r,s,t)/\partial t + cs\cdot\nabla_r I^{SP}(r,s,t) + \mu_a I^{SP}(r,s,t) = \\ &\quad \mu_s \int P(s,s')\left[I^{SP}(r,s',t) - I^{SP}(r,s,t)\right]ds' + I^{SP(0)}\delta(r-r_0)\delta(s-s_0)\delta(t-0) \end{aligned} \tag{2.1}$$

where vector $\mathbf{I}(\mathbf{r},\mathbf{s},t)$ has four polarization components, c is the light speed in the medium, μ_s is the scattering rate, μ_a is the absorption rate, and $\mathbf{P}(\mathbf{s},\mathbf{s}')$ is the 4×4 phase matrix [14], which describes the probability that the polarized light in the direction $\mathbf{s}'(\theta',\phi')$ will be scattered to the direction $\mathbf{s}(\theta,\phi)$. A meridian plane parallel to the z-axis and the light direction $\mathbf{s}$, is used as plane of reference for the description of the polarization state. With

a rotation of reference plane through an angle α≥0 (in the counterclockwise direction, when looking in the direction of propagation) $\mathbf{I}^{SP}$ varies as

$$\mathbf{I}'^{SP} = L^{SP}(\alpha)\mathbf{I}^{SP} \tag{2.2a}$$

This relation is given by

$$\begin{bmatrix} I' \\ Q' \\ U' \\ V' \end{bmatrix} = \begin{bmatrix} 1 & 0 & 0 & 0 \\ 0 & \cos 2\alpha & \sin 2\alpha & 0 \\ 0 & -\sin 2\alpha & \cos 2\alpha & 0 \\ 0 & 0 & 0 & 1 \end{bmatrix} \begin{bmatrix} I \\ Q \\ U \\ V \end{bmatrix} \tag{2.2b}$$

One has to be careful that all the Stokes parameters are refered to the same reference plane of the propagation direction. Therefore, a double multiplication by the transformation matrix L is necessary, first before scattering to refer the incident light to the scattering plane, then after scattering to change from the scattering plane to the meridian plane of the scattering direction. With fixed coordinates, zenith angle θ and azimuth ϕ, the phase matrix for scattering from a direction (θ', ϕ') to a direction (θ, ϕ) is given by:

$$\mathbf{P}(\mathbf{s}, \mathbf{s}') = \mathbf{L}(\pi - \chi)\mathbf{P}(\cos\Theta)\mathbf{L}(-\chi') \tag{2.3}$$

where χ' and χ are the two rotation angles. Θ is the scattering angle between light rays before $[\mathbf{s}(\theta, \phi)]$ and after scattering $[\mathbf{s}'(\theta', \phi')]$. The matrices $\mathbf{L}(-\chi')$ and $\mathbf{L}(\pi - \chi)$ are those required to rotate meridian planes before and after scattering onto or from a local scattering plane, as shown in Fig. 1. The intrinsic property of scattering is described by the 4×4 scattering matrix $\mathbf{P}(\cos\Theta)$ (see chapter 1.3 for detail about scattering matrix), which is assumed to be only dependent on $\cos\Theta = \mathbf{s}\cdot\mathbf{s}'$.

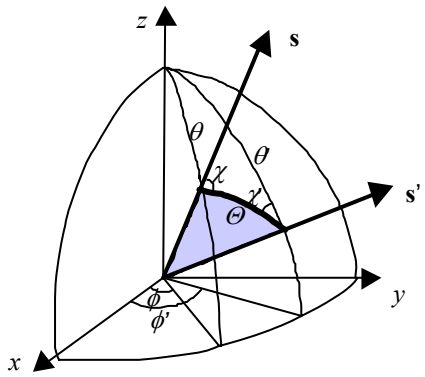

Fig.2.1 Geometry of the scattering plane and the reference planes related to the incident ray, s'(θ',ϕ'), and the scattered ray, s(θ,ϕ). The dark plane is the scattering plane. χ is the angle between the meridian plan (s,z) and the scattering plane. χ' is the angle between the meridian plane (s',z) and the scattering plane.

Rotation of co-ordinate axes often occurs when dealing with polarized light. It is therefore, important to investigate whether it can be done in a simpler way, for instance, by using a representation of the polarized light in which L(α) is diagonal, rather than Eq.(2.2).

A circular representation (CP) was presented by Hovenier [15], where $\mathbf{I}^{\mathrm{CP}} = [I_2, I_0, I_{-0}, I_{-2}]$, where $I_0 = (I + V)/2$, $I_{-0} = (I - V)/2$, $I_2 = (Q + iU)/2$, and $I_{-2} = (Q - iU)/2$. The relation between $\mathbf{I}^{CP}$ and $\mathbf{I}^{SP}$ is given by

$$\mathbf{I}^{\mathrm{CP}} = T\,\mathbf{I}^{\mathrm{SP}} \tag{2.4a}$$

with

$$T = \frac{1}{2}\begin{bmatrix} 0 & 1 & i & 0 \\ 1 & 0 & 0 & 1 \\ 1 & 0 & 0 & -1 \\ 0 & 1 & -i & 0 \end{bmatrix} \qquad \text{and} \qquad T^{-1} = \begin{bmatrix} 0 & 1 & 1 & 0 \\ 1 & 0 & 0 & 1 \\ -i & 0 & 0 & i \\ 0 & 1 & -1 & 0 \end{bmatrix} \tag{2.4b}$$

or

$$\begin{bmatrix} (Q+iU)/2 \\ (I+V)/2 \\ (I-V)/2 \\ (Q-iU)/2 \end{bmatrix} = \frac{1}{2}\begin{bmatrix} 0 & 1 & i & 0 \\ 1 & 0 & 0 & 1 \\ 1 & 0 & 0 & -1 \\ 0 & 1 & -i & 0 \end{bmatrix}\begin{bmatrix} I \\ Q \\ U \\ V \end{bmatrix} \tag{2.4c}$$

where T is the matrix to transfer vector $\mathbf{I}$ from Stokes representation ($\mathbf{I}^{SP}$) to circular representation ($\mathbf{I}^{CP}$). In CP a rotation of the reference plane through an angle α around the light direction causes can now be written as

$$I'^{CP} = L^{CP}(\alpha)I^{CP} = TI'^{SP} = TL^{SP}(\alpha)I^{SP} = TL^{SP}(\alpha)T^{-1}I^{CP} \tag{2.5a}$$

where

$$L^{CP}(\alpha) = TL^{SP}(\alpha)T^{-1} = \begin{bmatrix} e^{-i2\alpha} & 0 & 0 & 0 \\ 0 & 1 & 0 & 0 \\ 0 & 0 & 1 & 0 \\ 0 & 0 & 0 & e^{i2\alpha} \end{bmatrix} \tag{2.5b}$$

For the phase matrix, transform between two representations is $\mathbf{P}^{CP} = \mathbf{T}\mathbf{P}^{SP}\mathbf{T}^{-1}$.

On solving the transport equation [Equ.(2.1)], a well-known procedure is the expansion of the phase function in Legendre polynomials (see Ref.11 as an example). The transport equation is therefore splitted into independent equations, one for each Fourier component. For Mie scattering, the amplitude function is expressed in associated legendre function [see Equ.(1.10)-(1.13)] and the coefficients of the Legendre polynomial expansions can be obtained directly from the Mie coefficients a_n and b_n [see Equ.(1.14) and (1.15)]. The elements of the scattering matrix for polarized light can also be expanded in a series of Legendre polynomials. Kuščer and Ribarič [16], however, showed that an expansion in generalized spherical functions (GSF) is more appropriate. Elements of the CP phase matrix in the scattering plane, $P_{mn}^{CP}(\Theta)$ [see Equ.(1.21)-(1.23) for definition of phase matrix], can be expanded by GSF [17]:

$$P_{mn}^{CP}(\cos\Theta)=\frac{1}{4\pi}\sum_{l}p_{mn}^{l}P_{m,n}^{l}(\cos\Theta) \tag{2.6}$$

with m,n = 2,0,-0,-2, and $l \geq \max(|m|,|n|)$. The detail definition of the generalized spherical functions $P_{m,n}^{l}$ are discussed in the appendix of Ref.15. The generalized spherical functions are usually in radiative transfer theory, these functions also appear to in the study of angular momentum in quantum mechanics [18,19]. The functions $P_{m,n}^{l}(\cos\Theta)$ are connected to Wigner d-function in angular momentum as:

$$d_{m,n}^{j}(\cos\Theta)=i^{m-n}P_{m,n}^{j}(\cos\Theta), \qquad 0\leq\Theta<\pi \tag{2.7}$$

The coefficients p_{mn}^{l} in Equ. (2.6) provide an intrinsic description of the scattering mechanism. They have properties: (i) $p_{mm}^{l}=p_{m-m}^{l}$ are real; (ii) $p_{mn}^{l}=p_{nm}^{l}=p_{-m-n}^{l}$; (iii) $p_{20}^{l}=\left[p_{2-0}^{l}\right]^{*}$. Therefore, for each $l \geq 2$, there are six independent real elements: p_{00}^{l}, p_{22}^{l}, p_{0-0}^{l}, p_{2-2}^{l}, Re[p_{20}^{l}], and Im[p_{20}^{l}]. For l = 0,1, only p_{00}^{l} and p_{0-0}^{l} are nonzero. These numerical coefficients can be calculated using Mie theory for spherical scatterers. We have $p_{00}^{l}=(\alpha_1^l+\alpha_4^l)/2$, $p_{0-0}^{l}=(\alpha_1^l-\alpha_4^l)/2$, $p_{22}^{l}=(\alpha_2^l+\alpha_3^l)/2$, $p_{2-2}^{l}=(\alpha_2^l-\alpha_3^l)/2$, $\mathrm{Re}[p_{20}^{l}]=\beta_1^l$, $\mathrm{Im}[p_{20}^{l}]=\beta_2^l$, where the coefficients $\alpha_{1,2,3,4}^{l}$ and $\beta_{1,2}^{l}$ are formulated in Eqs.(4.81)-(4.86) in the book titled "Scattering, absorption, and emission of light by small particles" [20] by Mishchenko, and the Mie program provided in this book is used in our computation.

The above discussion introduced the circular representation of the polarized light and expanded the phase matrix in the generalized spherical functions. Based on those discussions, an analytical solution for time-dependent polarized photon transport equation [Equ. (2.1)] is studied in Appendix A. An exact angular distribution is obtained and a

cumulant expansion is derived for the polarized photon distribution function. By a cutoff at the second cumulant order, a Gaussian analytical approximation expression of the polarized photon spatial distribution is obtained as a function of the direction of light (**s**) and time (t) [see Equ.(A.34)]:

$$I_\nu(r,s,t)=\frac{F_\nu(s,t)}{(4\pi)^{3/2}}\frac{1}{[\det D_\nu]^{1/2}}\exp\left\{-\frac{1}{4}\left[(D_\nu)^{-1}\right]_{\alpha\beta}\left(r_\alpha-R^c_{\nu,\alpha}\right)\left(r_\beta-R^c_{\nu,\beta}\right)\right\} \qquad (2.8)$$

where the source is incident along z and $\nu=\|,\perp,R,L$, representing parallel, perpendicular, right-handed (RH), left-handed (LH) circularly polarized light, respectively.[see Equ.(1.6)]. The factor of the exponential function are summation with α, β = x, y, z.

Explicit expressions of all the terms in Equ.(2.8) are presented in the Appendix A. In Equ.(2.8), $r_\alpha = x, y, z$ is the coordinate of the detector. **s** is the direction of the detected scattered light. F_v(**s**,t) is the angular distribution of scattered light, which is defined in Equ.(A.3) and explicitly expressed in Equ.(A.9-A.11). $R^c_{\nu,\alpha}$ represents the position of the average center of the distribution [Equ.(A26)], and D_v is related to the half-width of the spread of the distribution [Equ. (A.33)]. The parallel ($\nu=\|$), perpendicular ($\nu=\perp$), right-handed ($\nu=R$) and left-handed ($\nu=L$) circularly polarized scattered light at position r_α(x,y,z) and final direction **s** can be obtained as a dependent of t from Equ. (2.8).

The following is an example for how to use Equ.2.8, supposed a right-handed circularly [$\mathbf{I}^{SP}$ = (1 0 0 1)] polarized light is incident along z to a random media at position (x, y, z) = (0, 0, 0), the time dependence of the right-handed circularly polarized backscattered light (ν = R, **s** = -1) at the position (x, y, z) = (-d, 0, 0) is calculated as the following steps: at fixed time and direction **s** = -1, first we calculated the angular

distribution $\mathbf{F}^{CP}$ in ciruclar representation [Equ. (A.9)]. Then substitute the transfer matrix T [Equ. (2.4b)], $\mathbf{F}^{CP}$ and the input Stokes parameter $\mathbf{I}^{SP}$ = [1 0 0 1] into the Equ.(A.11), we can obtain the angular distribution in Stokes representation $\mathbf{F}^{SP}$ = $\left[F_I^{SP}, F_Q^{SP}, F_U^{SP}, F_V^{SP}\right]$. The angular distribution $F_\nu(\mathbf{s},t)$ (ν = R) for the right-handed backscattered light in Equ.(2.8) is obtained by $F_R(s,t) = \left[F_I^{SP}(s,t) + F_V^{SP}(s,t)\right]/2$. Using the same steps we obtained $R_{R,\alpha}^c$, D_R from Equ.(A.24), (A.22), (A.26), (A.31), (A.29), (A.33). After we obtain F_R, $R_{R,\alpha}^c$, D_R, $\mathbf{r}$ = (-*d*, 0, 0) is substituted into Equ. (2.8) to obtain the right-handed backscattered light (I_R) at (x, y, z) = (-d, 0, 0) and fixed time *t*. Change the time *t* and repeat the previous steps we can obtain the time-resolved profile of the right-handed backscattered light at position (x, y, z) = (-d, 0, 0).

2.3 Numerical results of the polarized photon intensity distribution

Section 2.2 gave a general description of intensity distribution of scattered light. As an example, we studied the depolarization of circularly polarized light in a turbid medium. The depolarization of linear polarized light has been widely studied (see references 13, 14, 15 in Chapter 3). However, the backscattering properties of circularly polarized light deserve a more carefully consideration. In this section, we present the backscattering properties of circularly polarized light using the analytical solution we developed in Chapter.2.2. The incident wavelength in the following calculations is 610nm. The sample is prepared with polystyrene particles (refraction index is 1.59) inside the water. The results in the following paragraphs have been scaled to use the transport mean free path l_{tr} as the unit of length and the flight time for one transport mean free path in the medium l_{tr} / c as the unit of time (for example, if l_{tr} = 1cm, l_{tr} / c corresponds to

33.3ps). The program to obtain the results is presented in the Appendix B, the instruction for the usage of the program is also presented there.

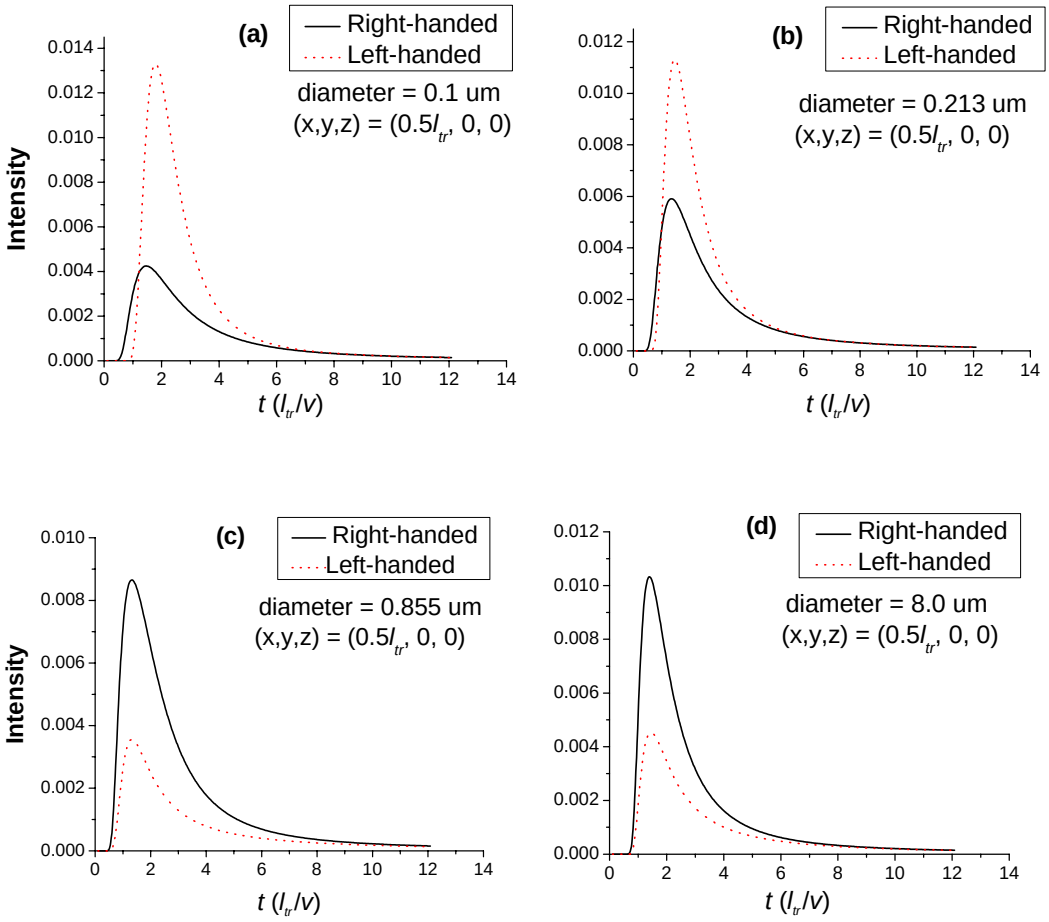

Fig.2.2 Particle size dependence of time-resolved profile of the right-handed (solid) and left-handed (dotted) backscattered (180^o) photon intensities at position (x, y, z) = (0.5l_{tr}, 0, 0) in an infinite medium containing particles of different diameters: 0.1 μm (a), 0.213 μm (b), 0.855 μm (c), 8.0 μm (d). The source is incident along the positive z axis at the origin of coordinate (x, y, z) = (0, 0, 0) and at time zero. The initial Stokes parameter I=[1 0 0 1] represents input right-handed circularly polarized light. The time is normalized to a unit l_{tr}/c.

First, we calculate the intensity distribution of backscattered light for scattering media containing different size of particles:0.213 μm, 0.855 μm, 2.89 μm, 8.0 μm (diameter). The source is incident to an infinite medium along the positive z axis at the origin of the

coordinate system (x,y,z) = (0,0,0) and at time zero. The initial Stokes parameter I = [1, 0, 0, 1] (see Chapter 1 for notation) represents a right-handed circularly polarized light. An detector centering at position (x,y,z) = ($0.5l_{tr}$, 0, 0) receives the backscattering intensity $I(\mathbf{r},\mathbf{s},t)$ at an angle $\theta = 180^{o}$.

Fig.2.2(a)-(d) shows the particle size evolution of the temporal profile of the backscattered right- (solid curve) and left-handed (dotted curve) circularly polarized light obtained from Equ.(2.8). For small size of particles (0.1 μm), the backscattered light is dominated with left-handed circularly polarized light, the helicity is flipped in the backscattered light [Fig.2.2(a)]. With the increase of particle size (0.213 μm), the intensity difference between right- and left-handed circularly backscattered light reduced [Fig.2.2(b)]. For large size of particle (0.855 μm, 8.0 μm), however, the helicity is maintained and the backscattered light is dominated with right-handed circularly polarized light. A physical model will be presented in Chapter 3 to explain the preculiar behavior of helicity in the circularly polarized light obtained from our analytical solution.

Fig.2.3 shows the particle size dependence of right-handed (RH) and left-handed (dotted) backscattered (180^{o}) photon intensity for a right-handed circularly polarized incident light. The intensity is obtained from the peak value of time-resolved profiles.

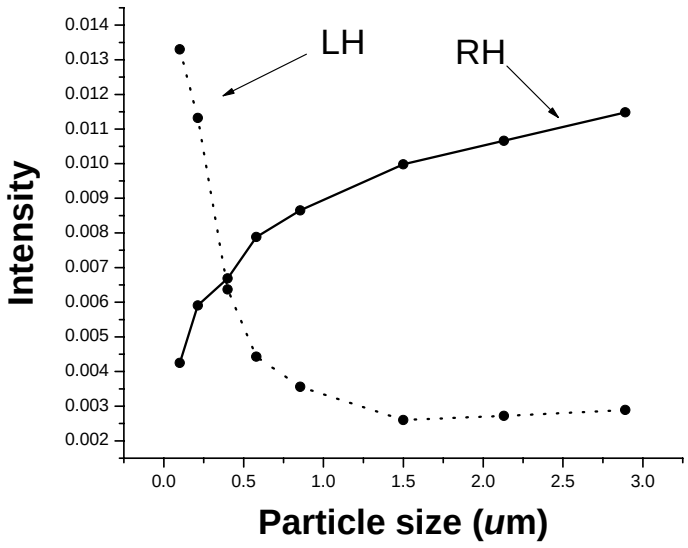

Fig. 2.3 Particle size dependence of right-handed (RH) and left-handed (dotted) backscattered (180^o) photon intensity at position (x, y, z) = ($0.5l_{tr}$, 0, 0) in an infinite medium. The source is incident along the positive z axis at the origin of coordinate (x, y, z) = (0, 0, 0). The initial Stokes parameter I=[1 0 0 1] represents input right-handed circularly polarized light.

We also obtained the particle concentration dependence of the backscattered light distribution for particle diameter D = 0.7 μm with different transport mean free path (l_{tr}). Fig.2.4 shows the time-resolved profile of the backscattered (180^o) photon intensity at position(d_0, 0, 0) in an infinite medium of different transport mean free path (l_{tr}): 10 d_0, 5 d_0, 1 d_0, where d_0 is a constant value used to rescale the transport mean free path and time. The source is incident along the positive z axis at the origin of coordinate (x,y,z) = (0, 0, 0) and at time zero. The time is normalized to a unit d_0/c. At a low concentration (l_{tr} =10 d_0), Fig.2.4(a) shows that the backscattered light is dominated by the helicity flipped light. However, with the increase of particle concentration, the intensity difference between helicity flipped and helicity preserved light is reduced, the intensity of the

helicity preserved photon exceeded the helicity flipped photon at l_{tr} =5 d_0 and occupied larger portion in the backscattered light at l_{tr} =1 d_0.

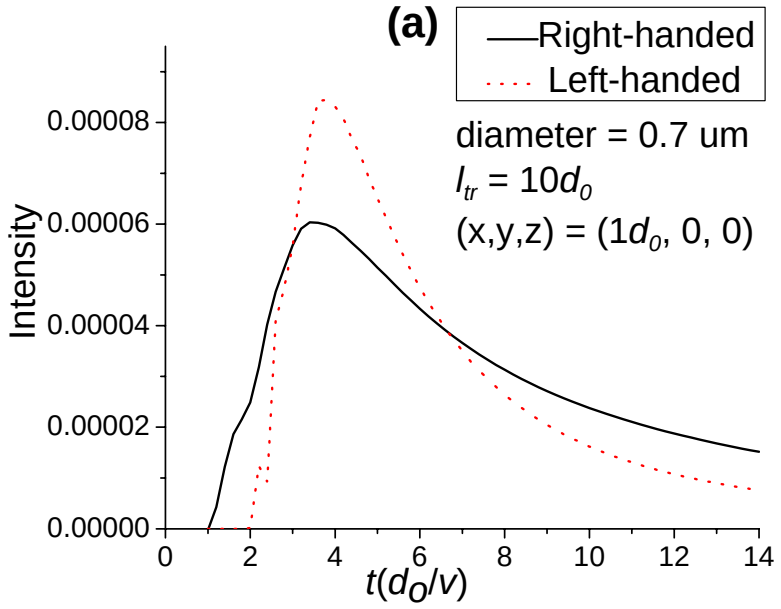

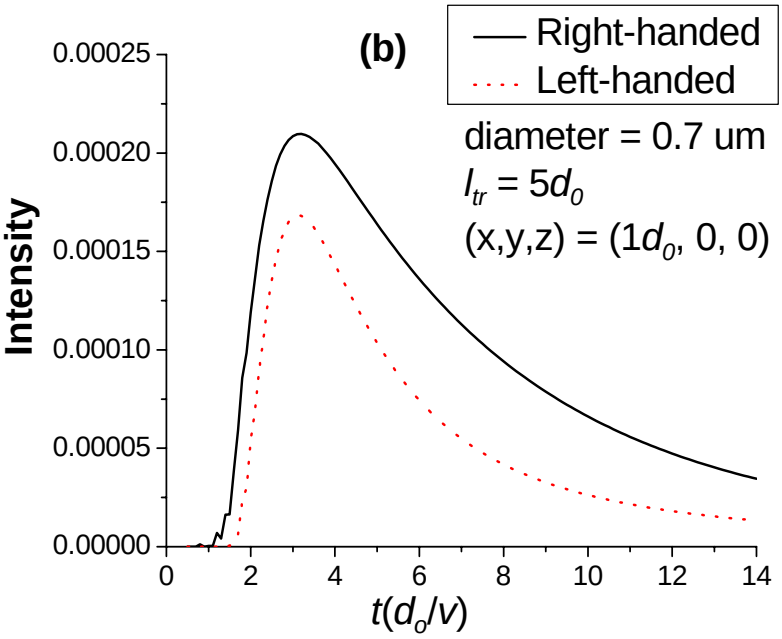

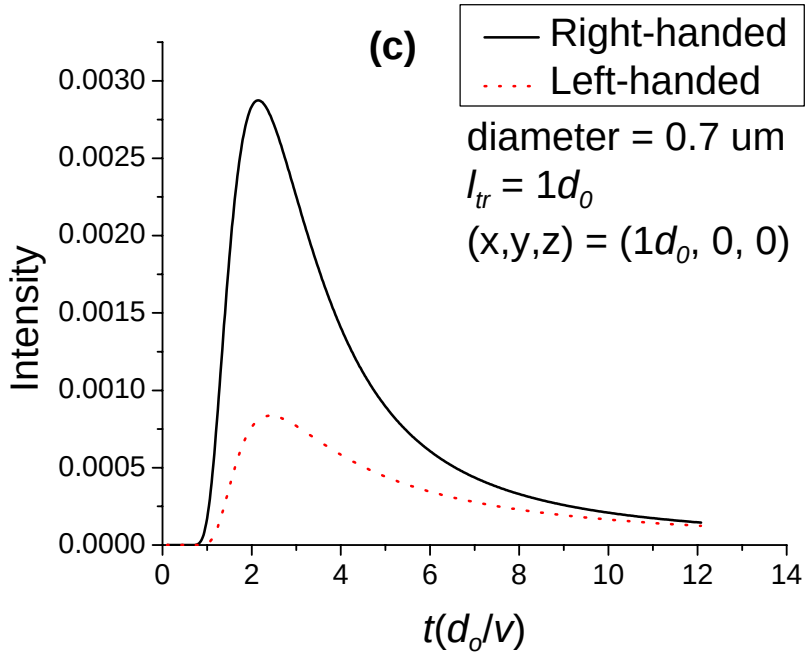

Fig.2.4 Concentration evolution of time-resolved profile of the right-handed (solid curve) and left-handed (dotted curve) backscattered (180°) photon intensity at position(d_0, 0, 0) in an infinite medium of different transport mean free path: l_{tr} = 10 d_0, 5 d_0, 1 d_0, where d_0 is a constant value used to rescale the transport mean free path and time. The source is incident along the positive z axis at the origin of coordinate (0, 0, 0) and at time zero. The input Stokes parameter **I** = [1 0 0 1] represents the right-handed circularly polarized light. The time is normalized to a unit d_0/c.

Fig.2.5 shows the time-resolved profile of the angular dependent photon intensity distribution at position (l_{tr}, 0, 0) and cosine of scattering angle corresponding to –1.0, -0.9, -0.8. The source is incident along the positive z axis at the origin of coordinate (x, y, z) = (0, 0, 0) and at time zero. The time is normalized to a unit l_{tr}/c. The incident light is right-handed circularly polarized. Fig.2.5 (a)-(c) shows that the helicity is preserved for all the three large scattering angles (cosθ = -1, -0.9, -0.8). With the decrease of scattering angle (cosθ = -1 to cosθ = -0.8), half-width of the scattered light is narrowed.

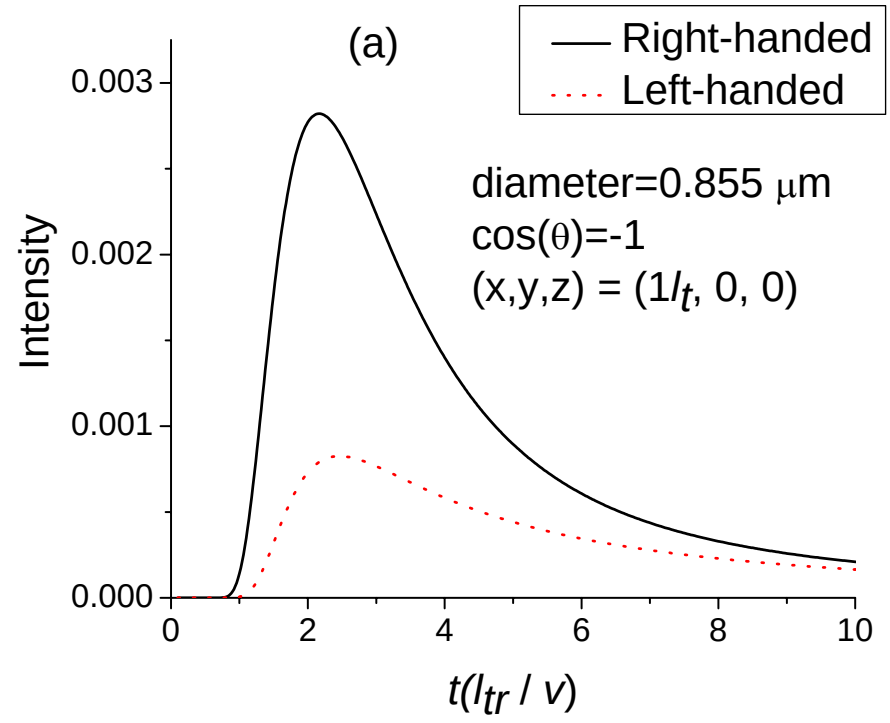
(a)
Right-handed
Left-handed
diameter=0.855 μm
cos(θ)=-1
(x,y,z) = (1/t, 0, 0)
Intensity
0.003
0.002
0.001
0.000
0
2
4
6
8
10
t(l_tr / v)

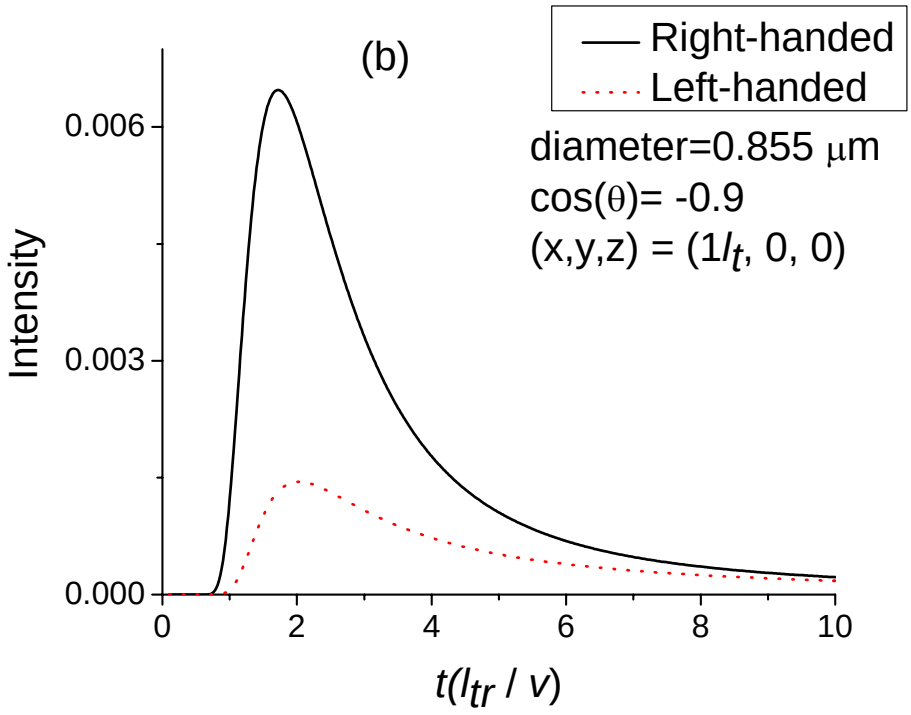
(b)
Right-handed
Left-handed
diameter=0.855 μm
cos(θ)= -0.9
(x,y,z) = (1/t, 0, 0)
Intensity
0.006
0.003
0.000
0
2
4
6
8
10
t(l_tr / v)

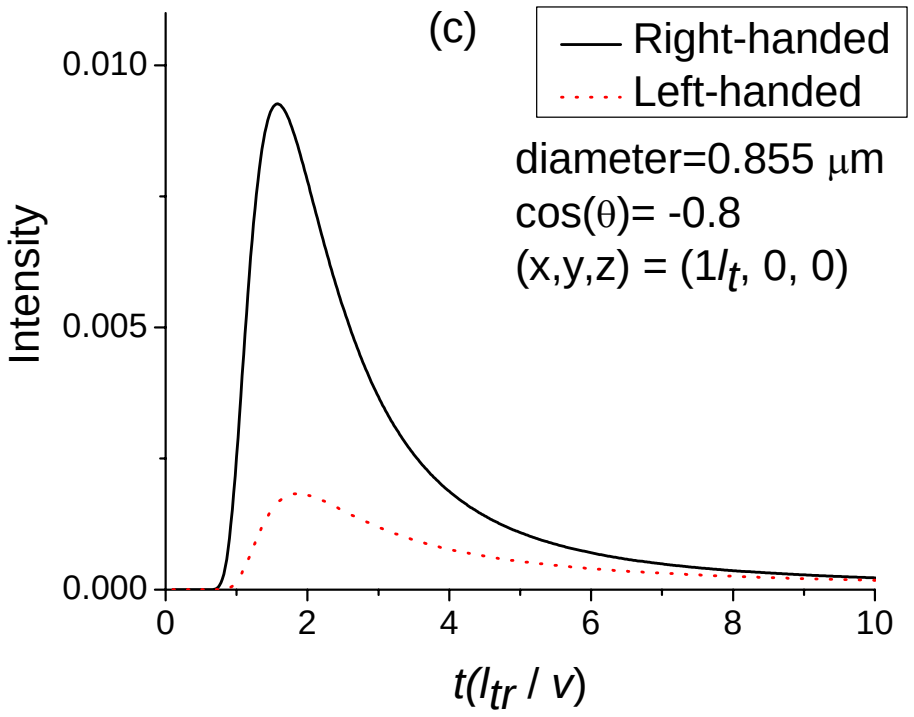

Fig.2.5 Scattering direction evolution of time-resolved profile of photon intensity at position (x, y, z) = (l_{tr}, 0, 0) and different cosine of scattering angle:-1.0, -0.9, -0.8. The source is incident along the positive *z* axis at the origin of coordinate (x,y,z) = (0, 0, 0) and at time zero. The time is normalized to a unit l_{tr}/c. The incident Stokes parameter I = [1 0 0 1] represents the right-handed circularly polarized light.

Here in this section, we have presented particle size, particle concentration and angular evolution of backscattering of circularly polarized light using our analytical solution to vector transport equation. The physical explanation and application of the circular polarization memory calculated in the section will be discussed in Chapter 3. We will fit the experimental measurements with the analytical solution we presented in this section in Chapter 3 (see Fig.3.7). A more detail discussion on the backscattering of circularly polarized light will be given then.

2.4 Conclusion

In this Chapter, we present an analytical solution of the time-dependent polarized photon transport equation in an infinite medium. Using a cumulant expansion, we can analytical calculate the spatial cumulants up to an arbitrary high order. By terminating at the second order, we have derived an explicit expression of the polarized light intensity distribution. This expression is quantitatively accurate up to the second order cumultant approximation. The central limit theorem claims that after enough collision events, all cumulants higher than second approach small values, and the Gaussian spatial distribution calculated approaches accuracy in detail.

Our results are given in terms of a distribution with coefficients that can be calculated algebraically. We performed numerical calculation for backscattering of circularly polarized light in scattering media. The particle size and particle concentration dependence of backscattered helicity are presented and consistent with our experimental data in Chapter 3.

References:

1. S. G. Demos and R. R. Alfano, Appl. Opt. **36**, 150 (1997).
2. S. G. Demos and R. R. Alfano, Opt. Lett. **21**, 161 (1996).
3. A. H. Hielscher, A. A. Eick, J. R. Mourant, and I. J. Bigo, Appl. Opt. **26**, 125 (1997).
4. B. D. Cameron, M. J. Rakovic, M. Mehrubeoglu, G. Kattawar, S. Rastegar, L. V. Wang, and G. Cote, Opt. Lett. **23**, 485 (1998).
5. S. R. Pal and A. I. Carswell, Appl. Opt. **24**, 3464 (1985).
6. X. Ni and R. R. Alfano, Appl. Opt. **42**, 6980 (2003).
7. R. Gans, Ann. Phys. (Leipzig) **75**, 1 (1925).
8. S. Chandrasekhar, *Radiative Transfer* (Clarendon, Oxford, 1950).
9. A. D. Kim and M. Moscoso, SIAM J. Comput. Sci. **23**, 2075 (2002).
10. Ambirajan, D. C. Look, J. Quant. Spectrosc. Radiat. Transfer. **58**, 171 (1997).
11. W. Cai, M. Lax, R. R. Alfano, Phys. Rev. E. **61**, 3871 (2000).
12. W. Cai, M. Lax, R. R. Alfano, Phys. Rev. E. **63**, 016606 (2000).
13. W. Cai, M. Xu, R. R. Alfano, Phys. Rev. E **71**, 041202 (2005).
14. H. C. van de Hulst, *Light Scattering by Small Particles* (Dover Publications, New York, 1981).
15. J. W. Hovenier, C. V. M. van der Mee, Astron. Astrophys. **128**, 1 (1983).
16. I. Kuščer, M. Ribarič, Optica Acta **6**, 42 (1959).
17. W. A. de Rooij and C. C. A. H. van der Stap, Astron. Astrophys. **131**, 237 (1984).

18. E. P. Wigner, *Group theory and its application to the quantum mechanics of atomic spectra* (Academic Press, New York, 1959).
19. B. M. Brink, G. M. Satchler, *Angular Momentum* (Clarendon Press, Oxford, 1962).
20. M. I. Mishchenko, L. D. Travis, A. A. Lacis, *Scattering, absorption, and emission of light by small particles* (Cambridge University Press, Cambridge, 2002).

Chapter 3

Backscattering of polarized light from turbid media

3.1 Introduction

Imaging an object hidden in a highly scattering medium is one of the challenging problems in many fields. Light propagating through a turbid medium undergoes multiple scattering, which randomizes the direction of propagation, phase, and polarization of the incident light. The image quality is affected by multiple scattering process. Over the years various techniques have been introduced to overcome this problem, such as time-resolved techniques[1,2], frequency-domain techniques[3], nonlinear optical techniques[4], optical low-coherence[5], confocal fluorescence microscopy[6], and active imaging[7,8]. Most these methods are difficult to implement due to the sophisticated mathematical problems or complicated experimental setups. Polarization imaging technique[9,10,11,12] has been well developed and can be easily deployed. It improves the image contrast by selecting the polarization state of the transmitted or backscattered light. The depolarization of scattered light from the turbid medium should be considered.

This chapter introduces time-resolved technology to study the depolarization of linearly and circularly polarized light backscattered from random media with different particle sizes and concentrations to determine the best technique to improve imaging. Circular polarization memory effect is observed and applied to improve the image contrast for a target inside the turbid media, which can be used to biomedical imaging problems (i.e. blood scattering).

3.2 Time-resolved backscattering measurement of linearly and circularly polarized light

The depolarization of a well defined incident polarization state from a medium depends on the sizes of the suspending particles[13,14,15]. For small particles in a medium (particle diameter a < wavelength λ), the transport mean free path (l_{tr}) approximately equals to the scattering mean free path (l_s) and the scattering is isotropic. Linear polarization can be persisted longer than circular in the transmitted light[15]. While for large particles ($a \geq \lambda$), $l_{tr} > l_s$ the scattering is highly forward and anisotropic; the depolarization length for a circularly polarized light is larger than corresponding length for an incident linearly polarized light for the transmitted light[14,15].

In this section, we investigate the time-resolved profiles of backscattering of circularly and linearly polarized light in two limits, a target inside the medium containing small spherical particles (a = 0.213 μm) and large spherical particles (a = 8 μm) in comparison with the wavelength of light (λ = 0.61 μm). The co-polarized and cross-polarized components are recorded simultaneously in time giving a clearer picture on the linear and circular polarization dependence of the temporal backscattered light profiles from the medium and from the target object. Based on the analysis of the temporal polarization profiles, the effectiveness of linear and circular polarization discrimination in imaging a target inside the turbid medium is presented.

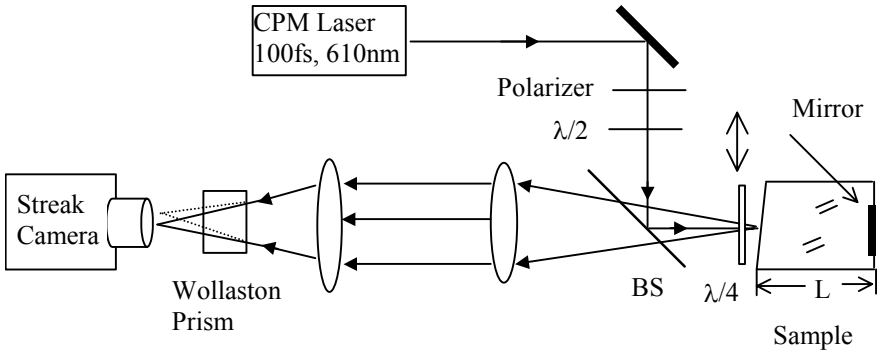

Fig. 3.1 Schematic diagram of the time-resolved backscattering measurement

The time-resolved polarization setup is schematically shown in Fig 3.1. The sample of the turbid medium comprises of polystyrene particles (refractive index n = 1.59) suspending inside the deionized water in a 6 cm (L) × 6 cm (W) × 10 cm (H) glass cell. The front wall of the cell is anti-reflection coated with a small wedge angle from the optical axis avoiding specular reflection from the front wall back towards the streak camera. A mirror is placed inside the cell on the back wall of the cell to act as a target object. Ultrafast laser pulses of 100 fs are generated at a repetition rate of 82 MHz by a colliding pulse mode-locked dye-laser system. The laser power is ~5mw at a wavelength centered at 610 nm. The polarizer and the half-waveplate ensure the linear polarization of the input laser pulses. The quarter-waveplate before the sample can be move in or out of the front of the sample. When the quarter-wave plate is positioned before the sample, the incident linear polarized light will be changed to circularly polarized light to impinge the sample, the backscattered light passes through the quarter-waveplate again and will be turned into linear polarized light. Without the quarter-waveplate, the linear polarized light is used for the measurements. A Wollaston prism was used to separate the co-polarized and cross-polarized backscattered light. For circular polarization measurement, right-

handed circularly polarized light was incident on the sample. The time-resolved profiles of the backscattered light are recorded by a Hamamatsu 2 ps streak camera.

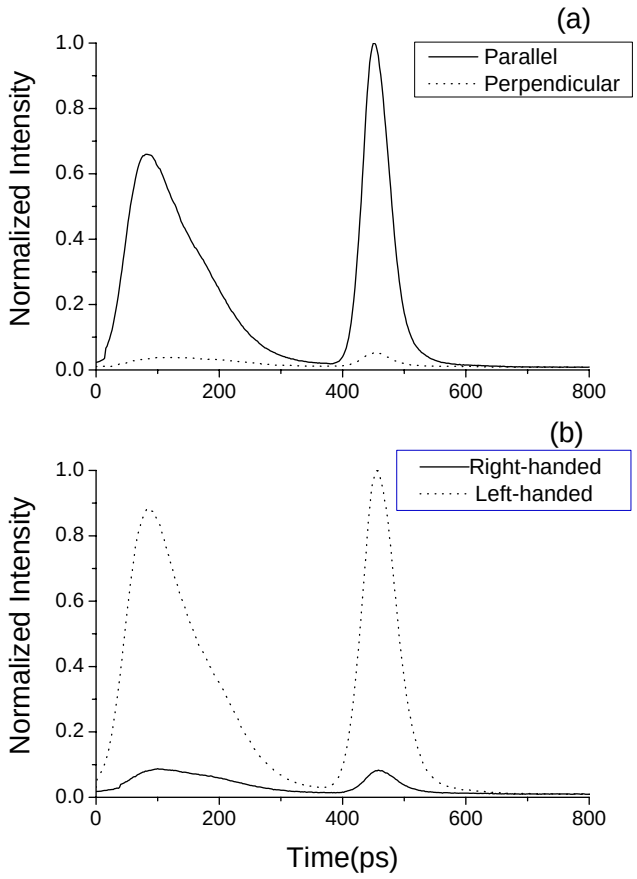

Fig. 3.2 Time-resolved profiles for co-polarized (solid) and cross-polarized (dotted curve) backscattered light from a turbid medium containing small particles with the diameter d = 0.213 μm. The scattering coefficient μ_s = 0.61 cm^{-1}. In Fig. 3a and Fig. 3b, the sample is illuminated with linearly and right-handed circularly polarized light, respectively. First peak in the profile is the backscattered light from the turbid medium. The second peak is the backscattered light from the mirror target at the back wall of the sample cell.

The time-resolved profiles of the backscattered light from the medium containing particles with diameters of 0.213 μm (anisotropy factor g = 0.389) for small particles and

8 μm (g = 0.911) for large particles are shown in Figs. 3.2 and 3.3, respectively. The first peak corresponds to the backscattered light from the turbid medium and the second peak corresponds to the backscattered light from a mirror target. The solid line is the co-polarized backscattered light (parallel to incident polarization or right-handed circular light) and the dotted line is the cross-polarized backscattered light (perpendicular to incident polarization or left-handed circular light). Both curves are normalized by the largest peak value among the four peaks (two peaks from co-polarized backscattered light and two peaks from cross-polarized backscattered light).

In Fig. 3.2(a), the small particle medium (scattering coefficient μ_s = 0.61cm^{-1}) is illuminated by linear polarized light. The backscattering light from the medium and mirror target is dominated by co-polarized light (solid curve). In Fig. 3.2(b), right-handed circularly polarized light impinges on the small particles solution. The profiles show that the backscattered light from the medium is dominated by left-handed circularly polarized light (dotted curve), the same handedness as the backscattered light from the mirror target (the reflected circularly polarized light from the mirror target is helicity flipped). In this case, polarization imaging will be hindered for both linearly and circularly polarized light. The strong backscattered signal from the target has the same polarization as the large backscattered light background. Since most of the target depolarizes the incident light (materials and geometrical properties) and the backscattered light from the medium is highly polarized, polarization imaging based on the backscattered polarized light perpendicular to the incident polarization or same helicity as the incident light may provide an enhancement of the contrast between the target and its background.

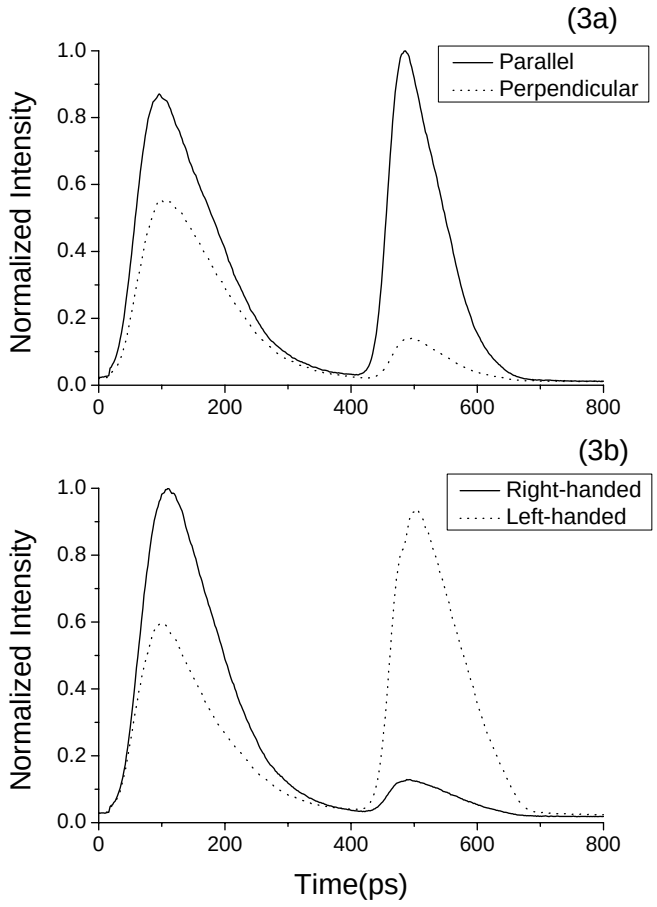

Fig. 3.3 Time-resolved profiles for co-polarized (solid) and cross-polarized (dotted curve) backscattered light from a turbid medium containing large particles with the diameter d = 8 μm. The scattering coefficient μ_s = 1.54 cm^{-1}. In Fig. 3a and Fig. 3b, the sample is illuminated with linearly and right-handed circularly polarized light, respectively.

The depolarization properties for backscattering profiles are markedly different for the large particles medium (μ_s = 1.54 cm^{-1}) case as shown in Fig. 3.3. The input linear polarization still mainly exists in the co-polarized backscattered light (solid curve) as shown in Fig.3.3(a). However, for the input right-hand circularly polarized light, Fig.

3.3(b) shows the dominated backscattered light from the host medium has the same handedness as the incident light (solid curve).

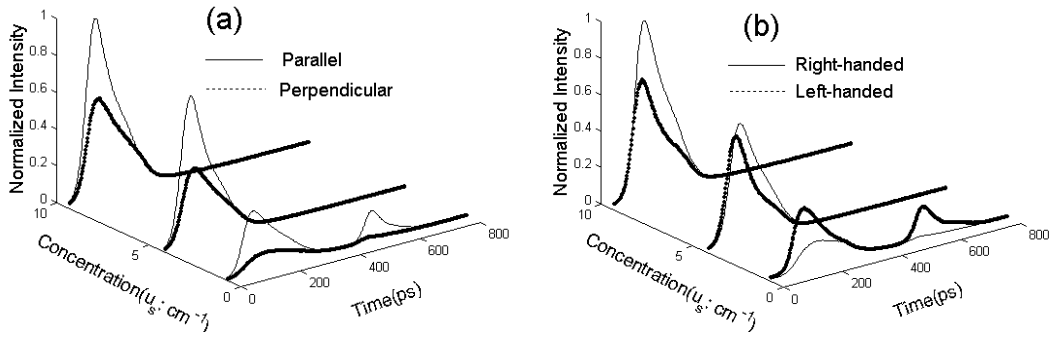

Fig. 3.4 Time-resolved evolution for co-polarized (solid) and cross-polarized (dotted curve) backscattered light from different scatterer concentration (μ_s = 0.71 cm^{-1}, 4.19 cm^{-1}, 9.29 cm^{-1}) media containing particles with the diameter d = 2.895 μm. The sample is illuminated with linearly and right-handed circularly polarized light, respectively.

Fig. 3.4 illustrates the evolution of the backscattered linearly [Fig. 3.4(a)] and circularly [Fig. 3.4(b)] polarized light at different scatterer concentration (μ_s = 0.71 cm^{-1}, 4.10 cm^{-1}, 9.29 cm^{-1}). The particle sizes of 2.89 μm are used in this measurement. At lower concentration (μ_s = 0.71cm^{-1}), the backscattered light is dominated by helicity reversed photon. With the increase of scatterer concentration, the proportion of polarization maintaining light increases as the arising of the number of scattering events. The same helicty light dominated the backscattered light after the attenuation of the target information below the threshold of detection. The difference between the polarization maintaining light and the cross-polarized light keeps growing with the further increase of concentration. The late formation of polarization maintaining in comparison with the 8 μm particle can be accounted for by the dependence of the angular distribution of the

scattered light on the size of the scatterers. For much smaller particles (d = 0.216 μm), the increase of scatter concentration cannot even produce the reversal of polarization. The backscattered light is always dominated with light of reversed helicity.

3.3 Physical model of circular polarization memory effect

Both our experimental data and analytical solution (see Chapter 2) show the helicity flipped in the backscattering of circularly polarized light from small particle suspensions and helicity preserved in the large particle suspensions. To understand why this is so, we first examined scattering by a single sphere using Mie theory (see Chapter 1.2).

Fig.3.5 shows the single scattering of right-handed circularly polarized light. We plot Stokes parameter V [see Equ. (1.4d) for definition of V] computed by Mie theory as a function of the cosine of the scattering angle Θ that correspond to backscattering for m = 1.19 for particles with a) diameter d = 0.213 μm; b) 0.855 μm; c) 2.0 μm; d) 8.0 μm. The incident pulse that we used to compute this quantity is right-handed circularly polarized with unit power. A positive value of V corresponds to right-handed circularly polarized light. The helicity is flipped ($V < 0$) around the near backward direction in the backscattered light from small particle (0.213 μm). These helicity flipped photon has a

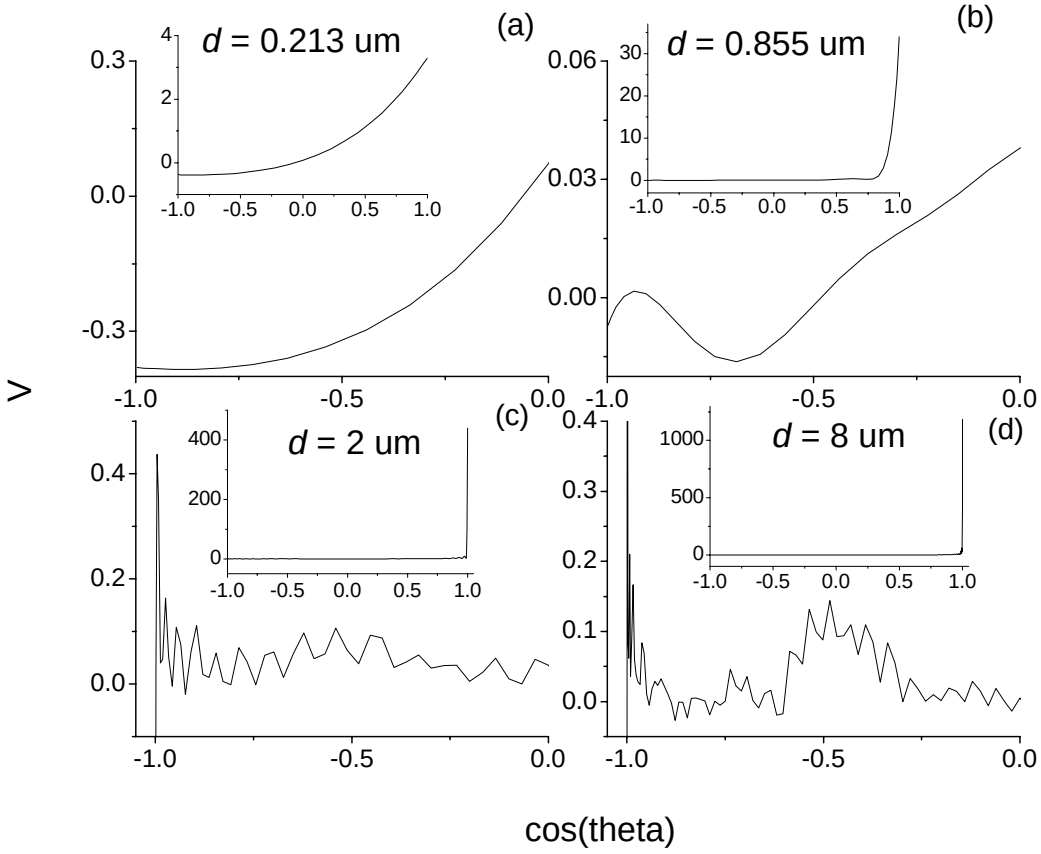

Fig. 3.5 Single scattering of input right-handed circularly polarized light. Stokes parameter *V* ("+": right-handed; "-": left-handed) computed by Mie theory for m =1.19 plotted as a function of the cosine of scattering angle Θ (90^o to 180^o) for backscattering. Four particle sizes are plotted: a) diameter d=0.213 μm; b) 0.855 μm; c) 2.0 μm; d) 8.0 μm. The scattering angle range is from 0^o to 180^o in the inset.

significant portion in the total scattered light. However, with the increase of particle sizes [Fig.3.5(b)-(c)], the helicity in the near backward direction is oscillating, the light is mostly forward scattered, the backward scattered occupied an ignorable portion in the total scattered light distribution.

Fig.3.6 is a pictorial representation of scattering of right-handed circularly polarized light by small particle suspensions and large particles suspensions. Right-handed

circularly polarized light impinges the turbid medium containing large size of particles [Fig.3.6(b)]. Single scattering event of large particle is most near-forward, the polarization memory [13] of right-handed polarized light comes from a sequence of smooth forward propagation trajectories that the incident light has experienced before contributing to the backscattered light. The circular polarization decays much slower than the linear polarization after those forward trajectories. While the reversed helicity for the small particle suspensions can be explained as single- or low-order scattering favors the reversed helicity and contributes to mainly portion of the backscattered light.

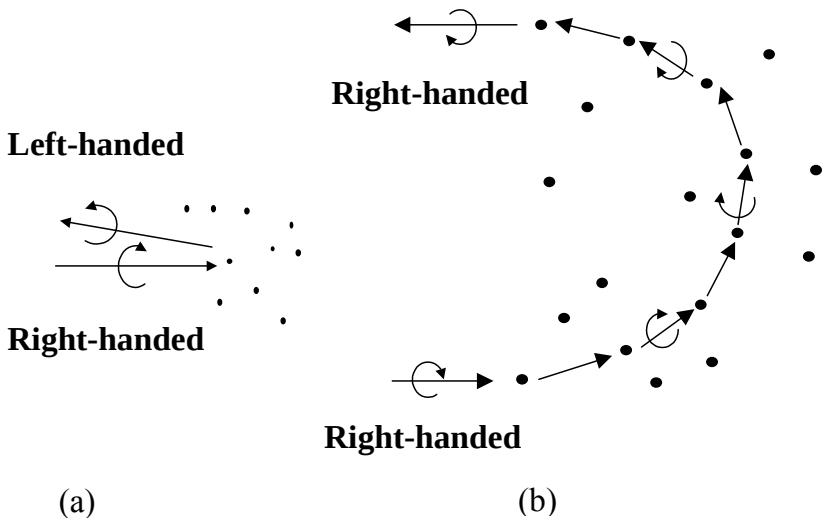

Fig.3.6 Pictorial representation of scattering of right-handed circularly polarized light by small particle suspensions and large particles suspensions.

A pictorial representation of backscattering of circularly polarized light in large particle suspensions containing a reflective object is shown in Fig.3.7. Right-handed circularly polarized light impinges the turbid medium containing large size of particles. The backscattered light without experiencing the reflection from the object comprises of mostly right-handed circularly polarized light and acts as the noise for the object information. The backscattered light that has experienced one reflection from the object

comprises of mostly left-handed circularly polarized light and acts as the useful object information, the specular reflection from the object reverses the incident helicity.

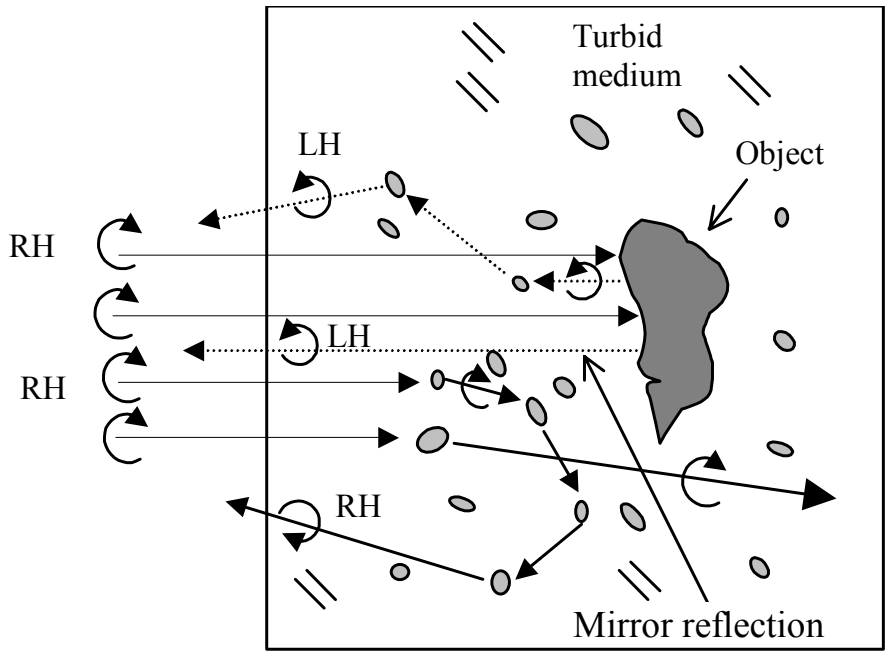

Fig. 3.7 A pictorial representation of backscattering of circularly polarized light in large particle suspensions containing a reflective object (RH: right-handed ; LH: left-handed). The incident right-handed circularly polarized light experiences a sequence of near forward scattering events before contributing to the backscattered light, helicity is preserved in these procedure. Reflection from the object reverses the helicity.

In Fig.3.8, we compared our experimental results of backscattering from large particle suspensions with theoretical calculation we presented in Chapter 2. The scattering parameters are the same as Fig.3.3: diameter $d = 8\ \mu$m and scattering coefficient $\mu_s = 1.54$ cm^{-1}. The incident light is right-handed circularly polarized. The square and dash symbols refer to experimentally measured right-handed (RH) and left-handed (LH) circularly polarized light, respectively. The solid and dot curves are calculated right-handed (RH) and left-handed (LH) circularly polarized light based on Equ.(2.18). Both experimental

and theoretical results show that the scattered light is dominated with light of same helicity as the incident light. The theoretical results agree quantitatively with experimental measurement. The difference came from unmatched boundary condition. In experimental measurement, the medium is prepared in sample cell, however, in current stage, our theoretical solution can just deal with the situation of infinite medium.

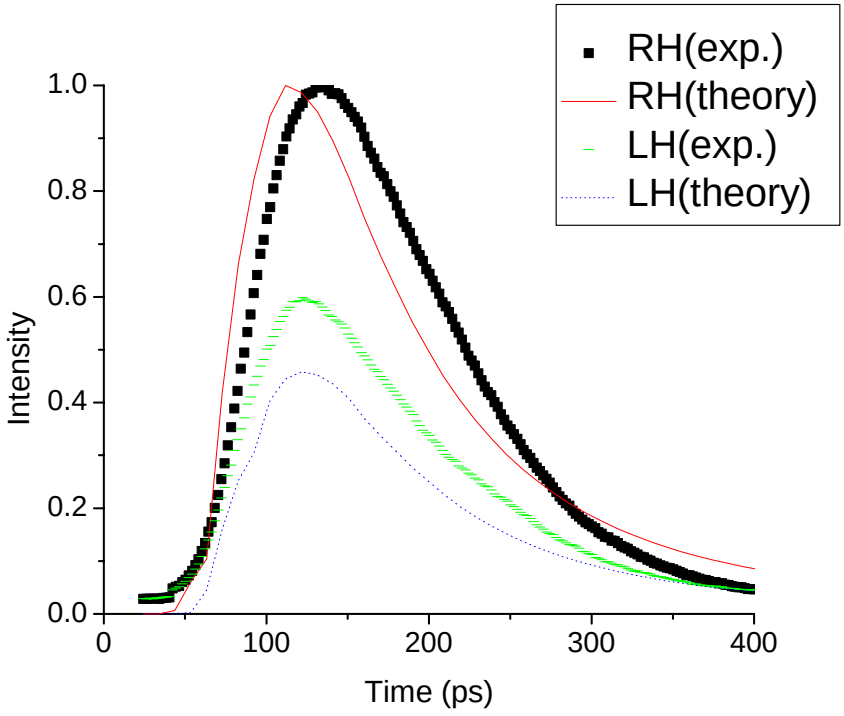

Fig.3.8 Comparison of theoretical and experimentally measured normalized intensity distribution of backscattered light. The incident light is right-handed circularly polarized light. The square and dash symbols refer to experimentally measured right-handed (RH) and left-handed (LH) circularly polarized light, respectively. The solid and dot curves are calculated right-handed (RH) and left-handed (LH) circularly polarized light based on Equ.(2.18). The scattering parameters are the same as Fig.3.3: diameter $d = 8\ \mu$m and scattering coefficient $\mu_s = 1.54\ \text{cm}^{-1}$

A closer examination of the polarization memory in the large particle suspensions indicated that the polarization memory strongly depends on the anisotropic factor g (see chapter 1.2 for the definition of g) of the particle and concentration of the suspensions. Our analytical solution can give the full evolution of polarization memory effect with these two parameters.

3.4 Polarization memory imaging

As we discussed in the previous sections, the depolarization properties of the backscattered light are quite different. For small particles ($a < \lambda$), the backscattering light is mostly contributed from the single scattering at large angle. In this case, linear polarization can preserve significant in the backscattered light, whereas the backscattering reverse the helicity of circular polarization and the backscattered light is predominated with light of opposite helicity (cross-polarized component). For large particles, the incident light experiences a sequence of near-forward scattering events before contributing to the backscattered light. The linearly polarized light is depolarized rapidly in this process, while helicity of the circularly incident light can be maintained[13,16].

Polarization memory of circular polarization provides an effective method for improving imaging of deep target since the target information and the strong backscattering background light have different helicity. These results suggest that continuous or time-resolved imaging with the cross-polarized backscattered light of the incident circularly polarized light can greatly improve the contrast of the image compared with co-polarized backscattered light or total intensity. Linear polarization imaging in this

case will still face the difficult that major target information and strong backscattering light background has the same polarization. As it is shown in Figs. 3.3(a) and (b), the contrast represented by the backscattered light from the target and from the medium is much lower in the linear co-polarized backscattered light (1.1 calculated from the backscattered peak of the object and host medium) than in the circular cross-polarized light (1.6). Perpendicular or same helicity imaging based on the depolarization properties of the target is not effective imaging technique in the large particles medium since the depolarized light from the medium is strong. Opposite helicity gives an improvement for imaging.

In this section, we present experimental data for the evolution of linearly and circularly backscattered polarization at different concentrations of small (0.202 μm in diameter less than incident wavelength, anisotropic factor g = 0.322) and large (10.143 μm in diameter larger than incident wavelength, g = 0.895) polystyrene particles using CW laser. The condition for the effectiveness of polarimetric discrimination to image a highly reflective target inside a turbid medium is considered and the improvement of a target image in large particle suspensions, registered by CCD-camera, is demonstrated using circularly polarized light.

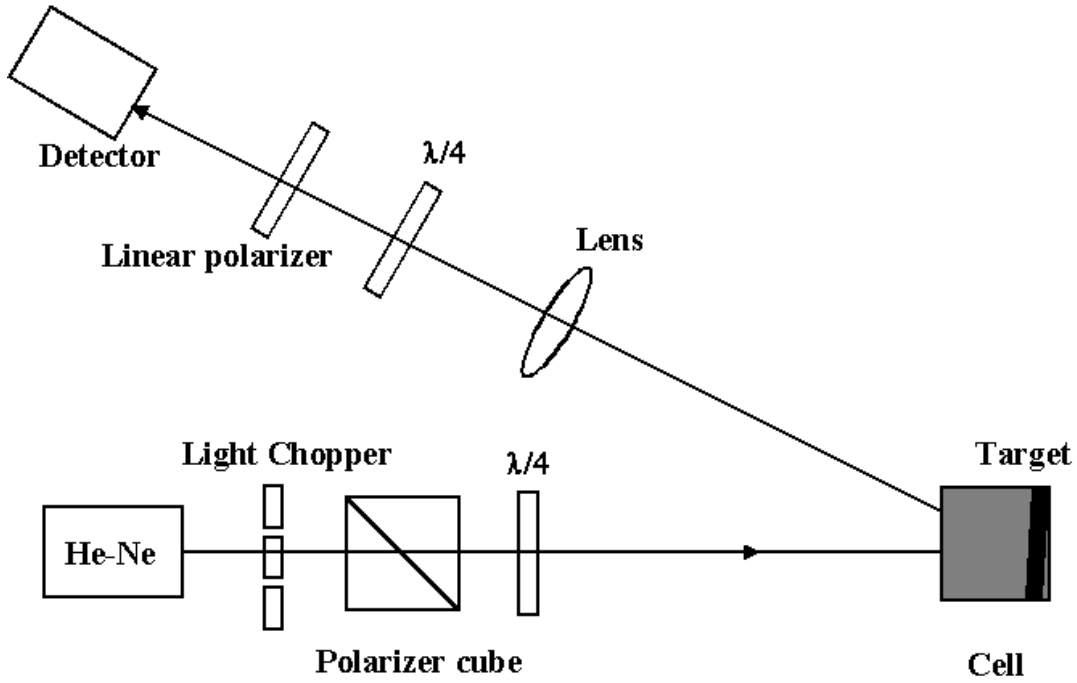

Fig. 3.9 Experimental arrangement for the backscattering imaging with He-Ne laser

The experimental layout is shown schematically in Fig.3.9. We prepared the samples of the turbid medium by diluting polystyrene particles into deionized water contained in a glass cell of square base cross section (3cm × 3cm). Samples containing particles of the diameter of 0.202 μm and 10.143 μm are used in this experiment, respectively. The cell is illuminated by He-Ne laser operating at 632.8 nm, chopped at 200 Hz. The diameter of the laser beam is 3 mm. The quarter-wave plates, polarizer and analyzer ensure either linear or circular polarization for incident and backscattered light. The photodiode, positioned approximately 4^0 off the backscattering direction, is used with a lock-in amplifier to measure the intensity of the light. For imaging purpose, the 1951 USAF glass slide positive resolution target (chrome pattern on clear background) is inserted inside the medium as the target. A cooled CCD camera (Photometrics Inc.) replacing the photodiode is used to record the image.

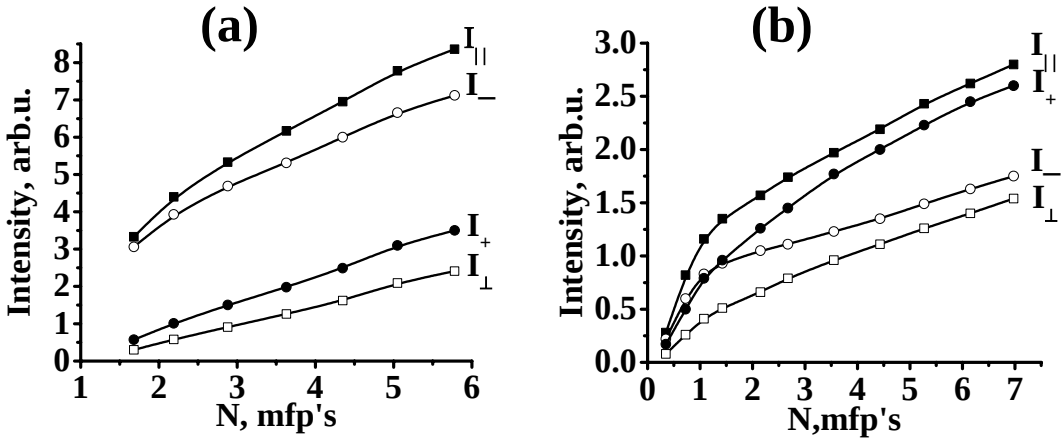

Fig.3.10 Dependence of the intensities of the backscattered light from a turbid medium on the number of scattering mean free paths (N, mfp's). $I_{||}$ represents the linearly co-polarized backscattered light; $I_{\perp}$ represents the linearly cross-polarized backscattered light; I_{+} represents the circularly co-polarized backscattered light; I_ represents the circularly cross-polarized backscattered light. In (a) and (b), the sample contains polystyrene particles with the sizes of 0.202 μm and 10.143 μm in diameter, respectively.

The intensity of backscattered light was measured for the four polarization channels: two linear polarization channels - parallel ($I_{||}$ - linearly co-polarized light) and perpendicular ($I_{\perp}$ - linearly cross-polarized light) to the polarization of the incident light, and two circular polarization channels - the helicity is the same as the incident light (I_{+} - circularly co-polarized light) and the opposite (I_ - circularly cross-polarized light). Dependences of the intensities of these four channels on the number N of scattering mean free paths (mfp's) are shown for 0.202-μm-diameter particles [Fig. 3.10(a)] and for 10.143-μm-diameter particles [Fig. 3.10(b)]. The number of scattering mfp's is calculated by $N= L\times\mu_s$, where L is the distance between the front surface of the cell and the target, μ_s is the scattering coefficient.

In Fig. 3.10(a) (small particle suspensions), $I_{\parallel}$ and $I_{\_}$ are larger than $I_{\perp}$ and I_{+}, respectively. This difference is due to the fact that there exists high contribution in the backscattered light from single or few scattering events. These large angles scattering contribution prefers the parallel polarization or opposite helicity. Fig. 3.10(b) (large particle suspensions) shows that linearly co-polarized light still dominates in the backscattered light from the large particle suspensions for all numbers of scattering N mfp's. The backscattered circular polarization is consisted preferentially of light of same helicity at higher concentration in comparison with the opposite helicity at lower concentration. This helicity reversal comes from the polarization memory effect. In the case of large particles, the light is scattered predominantly in the forward direction and contributes to the backscattered light from a return pathway. Helicity is maintained at the small angles scattering processes. The contribution of those return pathway light in the backscattered light increases with the increasing of suspensions concentration, which eventually leads to the appearance of polarization memory effect.

The measured backscattered light shown in Fig. 3.10 acts as the background noise impeding optical imaging of an object in a turbid medium. Polarization imaging technique can achieve a better image resolution over image based on total intensity by filtering out part of the diffusively backscattered light. Consequently the choice of input and detected polarization states is based on the requirement to maximize the contrast, which depends on the signal from the target and the backscattered light from the turbid medium. The polarization memory effect shown in Fig. 3.10(b) plays an important role for this purpose. When the sample is illuminated with polarized light, the reflectance from the target persists mainly the parallel to incident polarization or opposite helicity.

The linearly polarized light image can be obtained by selecting out the co-polarized light with an analyzer. As we can see from Fig.3.10, this technique is limited by the strongly background coming from the backscattered light of the turbid medium. However, by the use of circularly polarized light, the helicity persists on the backscattered light from the medium in the region N > 1.3 in Fig.3.10 (b) whereas target information is contained in the helicity reversed backscattered light. Opposite helicity imaging in this region takes advantage of low background light [$I_{\perp}$ in Fig. 3.10(b)] accompanied with main target information. Contrast of image using circularly polarized light can be improved with respect to the initial linearly polarized light image.

Figs.3.11 and 3.12 show images of the target inside the turbid medium consisting of small particles (0.202 μm) and large particles (10.143 μm), respectively. Figs. 3.11(a), and 3.12(a) show images obtained with linearly co-polarized light. Figs. 3.11(b), and 3.12(b) show images with circularly cross-polarized light. The curves represent the intensity profile along a window crossing the middle of the image. No obvious improvement is indicated with the selection of linear or circular polarization for the small particles solution (Fig. 3.11). The contrast, defined by the difference between the maximum intensity of the central bar of the target and minimum intensity for the left background divided by their sum, is equal to 0.09 for both cases of images of the target located 4.1 mfp's from the surface on which the light impinges. However, a significant enhancement of the image contrast is observed for the large particle solution (Fig.3.12) for the image with circularly cross-polarized light as we expected. In this case (Fig. 3.12), the target is located 8.4 mfp's from the surface and the contrast of image with linearly co-polarized light is equal to 0.03 in comparison with 0.1 for circularly cross-polarized light.

The polarization memory of the diffusive backscattered circularly polarized light leads to this improvement.

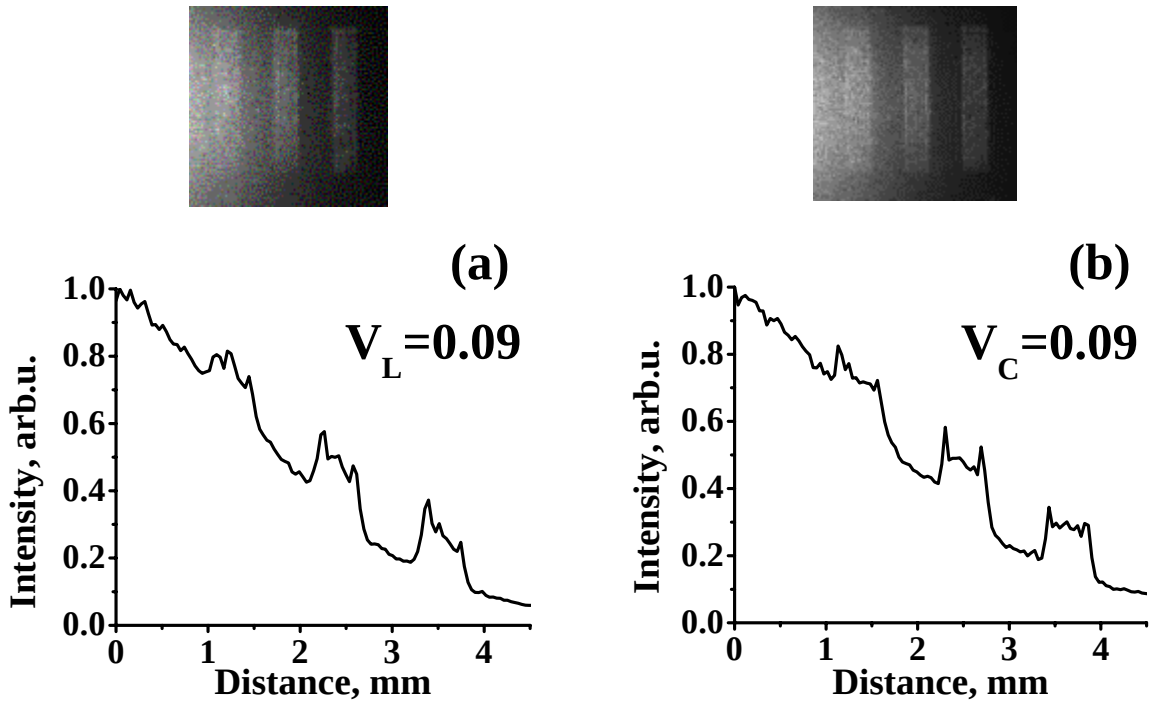

Fig. 3.11 Images and intensities profile on the CCD-camera of the high reflective target inside the turbid medium containing small particles with the diameter d = 0.202 μm. Linearly co-polarized light (a) and circularly cross-polarized light (b) in the backscattered light are selected out to image, respectively. The number of scattering mean free path (N, mf'p's) is equal to 4.1.

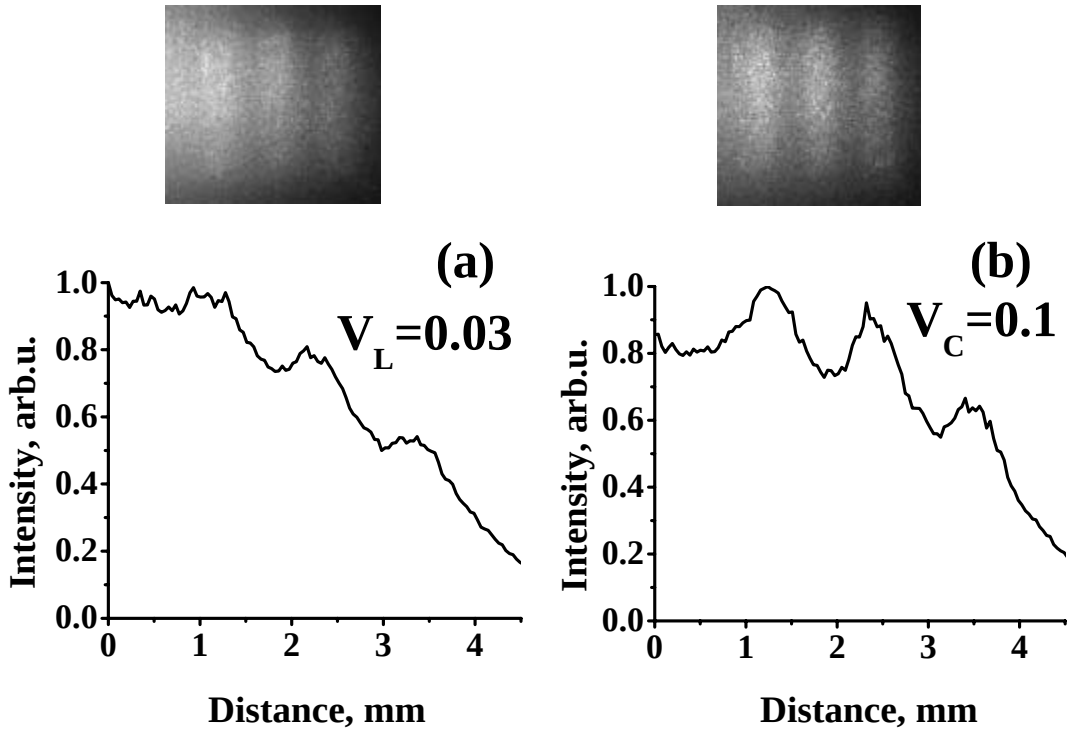

Fig. 3.12 Images and intensities profile on the CCD-camera of the high reflective target inside the turbid medium containing large particles with the diameter d = 10.143 μm. Linearly co-polarized light (a) and circularly cross-polarized light (b) in the backscattered light are selected out to image, respectively. The number of scattering mean free path (N, mfp's) is equal to 8.4.

The imaging technique described here, which uses helicity flipped circularly polarized light, can be used to penetrate deeply inside the turbid medium containing large scatterers and obtain a better image of the reflective target object. To advance this technique to real world applications, it should be employed in combination with other gating techniques (Fourier space, time, and wavelength). Since generally the target itself can depolarize the light, the optimum choice of polarization based upon the value of the polarization component backscattered from the target and the medium itself. In some

cases, imaging with linearly cross-polarized or circularly co-polarized light can be used for a highly depolarized target.

3.5 Conclusion

In conclusion, circularly polarized light is better for imaging objects inside large particle suspensions due to slowly decay of circular polarization and helicity reversal of specular reflection. We have shown the differences exist between the time-resolved backscattering of circularly and linearly polarized light from medium with different particle sizes, with particular interest paid to the polarization memory of the circularly polarized light. We have clearly demonstrated that imaging of a reflective target inside large particle scattering suspensions using polarization memory with circularly cross-polarized light provides a significant improvement in comparison with linear polarization states. The large particle chosen in this study has similar anisotropic factor as atmospheric environments like aerosols, heavy fog, cumulus, and seawater as well as biological tissues. For atmospheric applications, the multiple scattered light experiences less absorption from the host medium (air) than medical and biological media, which can further improve the imaging contrast using circular polarization preserved multiple scattered light. A most important application for polarization memory effect is to better image the artery wall and assess plaque composition through blood field. The scattering from the large particles like red blood cells with an average diameter of 7.65 μm in the blood is reduced due to polarization memory [17] using circularly polarized light.

References:

1. L. Wang, P. P. Ho, G. Liu, G. Zhang, and R. R. Alfano, Science **253**, 769 (1991)
2. D. Huang, E. A. Swanson, C. P. Lin, J. S. Schuman, W. G. Stinson, W. Chang, M. R. Hee, T. Flotte, K. Gregory, C. A. Puliafito, and J. G. Fujimoto, Science **254**, 1178 (1991).
3. M. A. O'Leary, D. A. Boas, B. Chance, and A. G. Yodh, Opt. Lett. **20**,426 (1995).
4. Y. Guo, H. E. Savage, F. Liu, S. P. Schantz, P. P. Ho, and R. R. Alfano, Proc. Natl. Acad. Sci. **96**, 10854 (1999).
5. A. Schmidt, R. Corey, and P. Saulnier, Opt. Lett. **20**, 404 (1995).
6. B. R. Masters, A. Kriete, and J. Kukulies, Appl. Opt. **32**, 592 (1993).
7. P. Clemenceau, A. Dogariu, J. S. Stryjewski, *Polarization active imaging*, in *Laser Radar Technology and Applications V*, G. W. Kamerman, U. N. Singh, C. H. Werner, and V. V. Molebny, Eds., Proc. SPIE **4035**, 401 (2000).
8. P. Y. Gerligand, M. H. Smith, R. A. Chipman, Opt. Express **4**, 420 (1999).
9. S. G. Demos, R. R. Alfano, Appl. Opt. **36**, 150 (1997).
10. S. P. Morgan, M. E. Ridgway, Opt. Express **7**, 395 (2000).
11. G. D. Lewis, D. L. Jordan, and P. J. Roberts, Appl. Opt. **38**, 3937 (1999).
12. G. D. Gilbert, J. C. Pernicka, Appl. Opt. **6**, 741 (1967).
13. F. C. MacKintosh, J. X. Zhu, D. J. Pine, D. A. Weitz, Phys. Rev. B. **40**, 9342 (1989).
14. E. E. Gorodnichev, A. I. Kuzovlev, and D. B. Rogozkin, JETP Lett. **68**, 22 (1998).

15. D. Bicout, C. Brosseau, A. S. Martinez, and J. M. Schmitt, Phys. Rev. E **49**, 1767 (1994).

16. A. D. Kim, M. Moscoso, Opt. Let. **27**, 1589 (2002).

17. R. R. Alfano and X. Ni, "Methods to improve backscattering imaging through large particle suspensions using circular polarization memory", U.S. Patent Application Serial No. #60/675,479 (Provisional patent application).

Chapter 4

Coded Pulse Propagation in Turbid Media

4.1 Introduction

Ballistic and snake-like photons can carry the original information of the incident pulse. Beer's law indicates an exponential decay of the ballistic pulse and diffusion equation describes the diffuse light which degrades the information. Theoretical description of photon in the intermediate region (ballistic to diffuse) is still a challenging problem. The Gaussian distribution we used in Chapter 2 is accurate at long times and in the backscattering case, since many collisions lead to a Gaussian distribution according to central limit theorem. Computation of high-order cumulants or a different-shaped distribution form are needed to modify the theory to describe the intermediate region component.

In this chapter, we study the laser pulse propagation through scattering media using the time-resolved techniques. Spatial gating, polarization gating and polarization analysis are presented to extract the early ballistic and snake-like components from the diffusive components on code information pulse train. The potential application for those techniques in wireless optical communication through cloudy and foggy media is demonstrated.

4.2 Free-space ballistic laser propagation of a pulse coded data stream through fog

Free space optical (FSO) technology has been in existence for nearly four decades. Recently, FSO has experienced an unprecedented growth due to needs of the "last mile"

users who have demanded high speed data connectivity in the home and office [1,2]. Although microwave and radio based systems are attempting to provide a solution to eliminate the bottleneck restricting high speed data connectivity into home and offices, wireless optical communication possess much higher bandwidth in access(0.1-1 Gbps). The market size for FSO is expected to grow to a multi-billion dollars level by 2006 [2]. FSO can be implemented with wavelength division multiplexing with ultra-wide supercontinuum band tunable fs laser sources. The large available bandwidth for wireless optical communication can operate without licensing which limits the future of radio or microwave systems. Fiber-optic system can provide even a higher bandwidth (2.5Gbps-40Gbps) link which is competitive with free space optical communication. As the optical fiber attenuate the signal in a predictable rate, it is possible to amplify and compensate the signal. Fiber optical communication is preferred for long haul system and backbone networks. For metro-network, free space optical communication has the advantage of low cost of the equipment, easy and fast deployment and flexible service rollouts in any network topology. FSO offers even larger bandwidth into tera-peta bit/s range.

Unfortunately, the scattering and absorption under different weather conditions attenuate the transmitted wireless optical signal with an unexpected way which limits its application in long haul system. The major disadvantage comes from multiple scattering, which will broaden the signal temporal response. The broadened signals will overlap with each other which lead to a degradation of information and limit the ultimate bandwidth that can be used. Pulse laser source, which represents the signal ‘1’ with a much narrower laser pulse, owns several advantages over modulated CW laser in transmitting signals through atmospheric environment. The narrow pulse has much higher energy intensity,

so the signal can survive a longer distance before has been attenuated. When an ultrafast laser pulse propagates through a turbid media (cloud, fog, or smog), the detected pulse was broadened into early and diffusive components in the temporal domain. The early component includes ballistic component[3] and snake component[4] which is usually buried in the diffusive light background from the previous pulses. The ballistic and snake components carry the original data information sent by the source and are considered as the signals. Several techniques can be used to discriminate the data signal[5,6] from the diffusive light which acts as the noise. The space gate and polarization gate use the randomization properties of the propagation direction and polarization of the diffusion light due to the multiple scattering. A space gate is used to restrict the angular emission along the received direction that excludes diffusive photons from directions other than that from the source. The polarization gate makes use of the fact that ballistic and snake photons retain their polarization memory while diffusion component is depolarized by the scattering events of an incident beam of polarized light. Time gate technique [7], which needs a reference light to select out the ballistic and snake component, can be achieved using a timing auto-tracking pulse beam which is also used to help compensate for building sway.

In this section, we investigate the extraction of a 10 GHz pulse coded train after passing through a fog medium using space and polarization gates. To select the ballistic component, the off-axis diffusive component is rejected by the apertures in the incident light direction. A polarization analyzer is used to extract the ballistic photons with polarization parallel to incident polarization and to filter out the diffusive photons with

different polarization. Combine these two techniques, we will demonstrate a significant improvement in the ballistic pulse signal detection passing through dense fog media.

The attenuation of the ballistic light passing through the atmosphere is described by:

$$I = I_0 \exp(-\mu_T L_m) \tag{4.1}$$

where I and I_0 is the detected and source light intensity, respectively; μ_T is the extinction coefficient (the sum of extinction coefficients due to the light scattering and absorption from the particles $\mu_T = \mu_s+\mu_a$); and L_m is the distance between the light source and detector.

The visibility[8,9] (S_v) is a measure of the effect of obscurants in the atmosphere. The visibility through the fog is the maximum distance of human eye to be able to see a large dark object. It is determined primarily by the object's visual contrast with the background. The contrast is caused by differences of both color and brightness (intensity), but since atmospheric visibility in cloud, fog and smog is restricted by large particles that scatter all colors equally, and since most objects are dark compared to the sky, we consider only brightness differences. Thus, the contrast of object for eye, or the brightness difference between the object and the background divided by the brightness of the background is

$$Contrast = \frac{\left|I_{object} - I_{background}\right|}{I_{background}} \tag{4.2}$$

The limit of visibility, S_v occurs when the contrast equals 0.02, or when

$$0.02 = \frac{\left|I_{object} - I_{background}\right|}{I_{background}} = \exp(-\mu_t S_v) \tag{4.3}$$

Solving for the distance, S_v, yields,

$$S_v = \frac{3.9}{\mu_T} = 3.9 l_T \tag{4.4}$$

where l_T is the total extinction mean free path(the sum of l_T due to the scattering mean free path and the absorption mean free path $\mu_T = 1/l_T = 1/l_s + 1/l_a$)

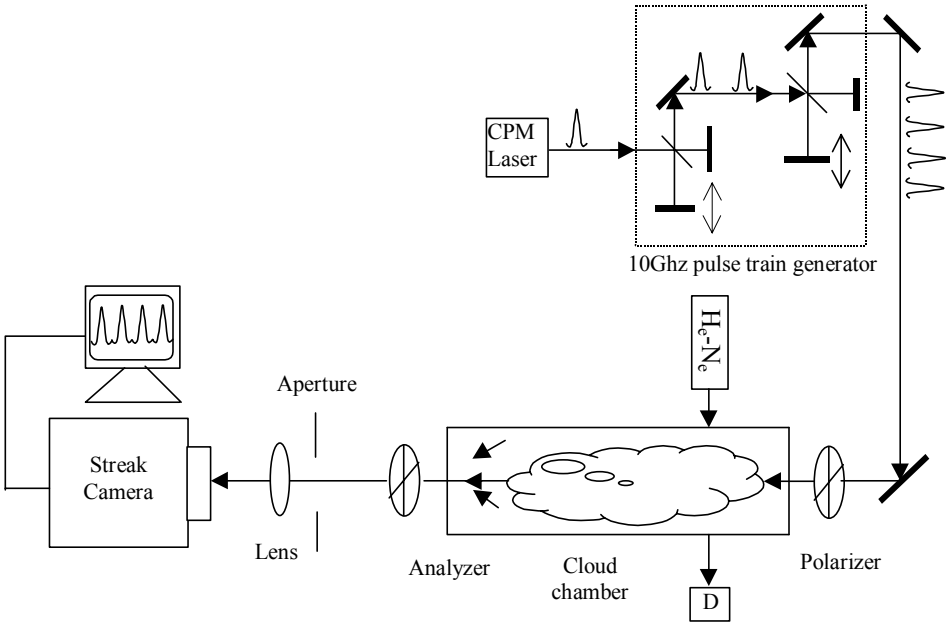

Fig. 4.1 Schematic diagram of the experimental setup for pulse going through cloud chamber

The experimental arrangement to test the gating method is shown in Fig. 4.1. Ultrafast 100 fs laser pulses are generated at a repetition rate of 82 MHz by a colliding pulse mode-locked dye-laser (CPM) system. The laser power is set at 5 mW at a wavelength centered at 620 nm. The polarized laser beam is collimated and incident into a 182 cm × 15 cm cylindrical fog chamber using nebulizers and commercial fog generators (UL Fogger 700 by NESS). Two sets of Michelson- interferometer-like setup are used to generate a pulse train of four pulses. These four pulses are the signals. The duration between two pulses can be adjusted by changing the distance of the arms in the setup. We set the duration to 100 ps in this experiment, corresponding to a repeat rate of

10 GHz. The analyzer can be used to select out the transmitted light parallel to the incident polarization state. A lens of 5 cm focus length is used to focus the ballistic and scattered light in the transmitted direction to the slit of the streak camera. One aperture before the streak camera combined with the slit inside the streak camera act as the spatial gate. The spatial, temporal, and polarization profiles of the pulse train are recorded by the Hamamatsu streak camera. A He-Ne laser and a power meter are arranged to simultaneously monitor the density of fog and estimate the beam attenuation. The length of the chamber is 182 cm. The visibility of the fog is calculated from Equ. (4.1) and Equ. (4.4) when across the chamber of 15 cm:

$$S_v = \frac{3.9 L_m}{\ln I_0 - \ln I} \tag{4.5}$$

where L_m is the diameter of the chamber which is 15 cm. The experiment is done in heavy fog for distance of 182 cm where $L / l_T = 31$ is the number of scattering events.

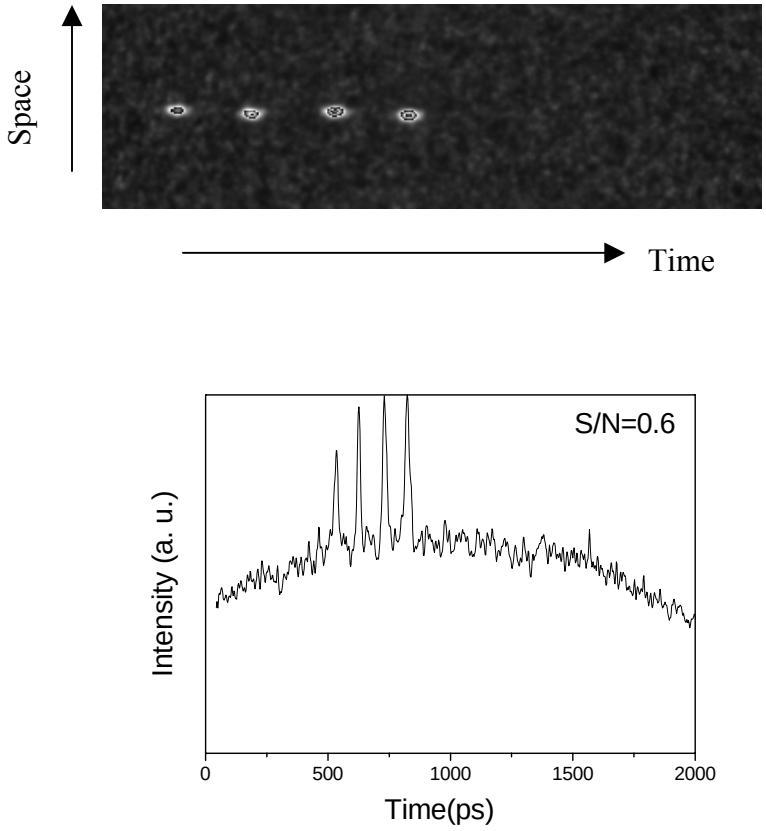

Fig. 4.2 Temporal profiles of the pulse train measured with a streak camera. Profiles are recorded without analyzer and with a wider streak camera slit(120 channels).

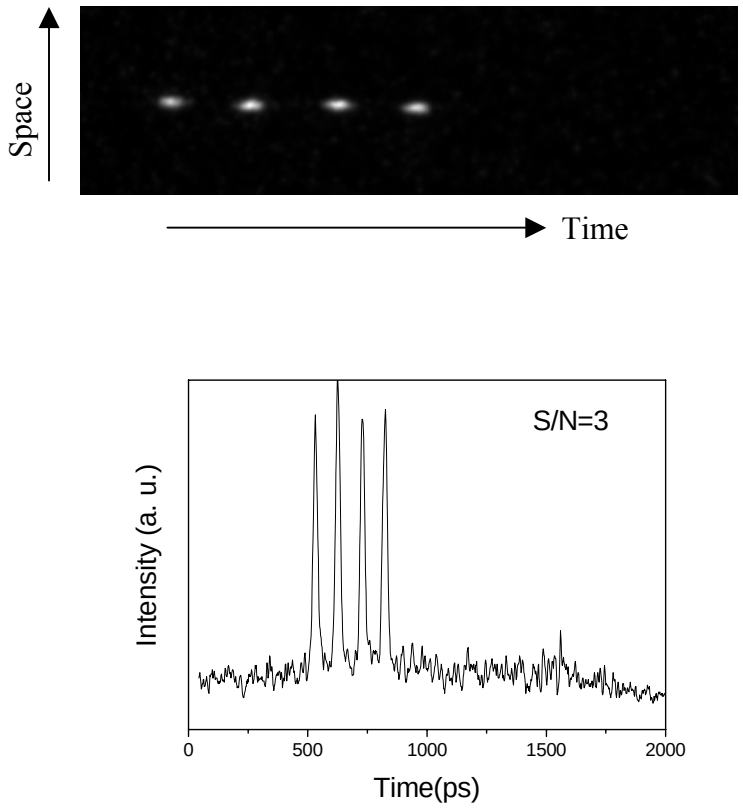

Fig. 4.3 Temporal profiles of the pulse train recorded with analyzer oriented parallel to polarizer axis and with a wider streak camera slit(120 channels).

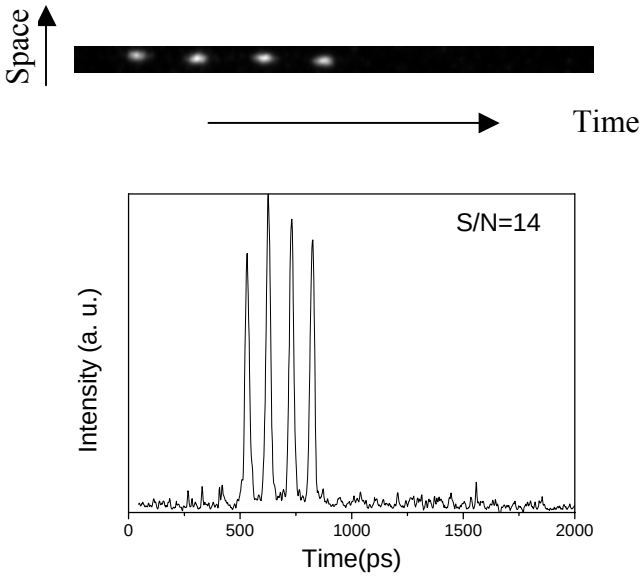

Fig. 4.4 Temporal profiles of pulse train recorded with analyzer oriented parallel to polarizer axis and with space gate of a narrower streak camera slit(16 channels)

A lab scale "test" experiment was performed using a much denser atmosphere environment due to the long visibility in the atmosphere. One can rescale our results from the laboratory environment to atmosphere environment in which the S_v is much larger and the scattering concentration is much lower.

Fig. 4.2 to Fig. 4.3 shows the recorded profiles of the pulse train in the dense situation of S_v = 22.7 cm (l_t = 5.8 cm) under different gate conditions. The horizontal direction represents the time and the vertical direction represents the space. The curve is the accumulated intensity of the received light along the space (vertical direction). Figs. 4.2 shows the temporal intensity profiles recorded by the streak camera with a wider slit (120 channels) without analyzer. The background noise, which is contributed by the multiple scattered light, impairs the transmitted information obviously. The signal to noise ratio (S/N) ~ 0.6 is low in this case. The diffuse background noise before the first ballistic

pulse arrived is contributed from the previous four pulses due to the 82MHz repetition rate of the CPM. Fig. 4.3 illustrates the temporal profiles, respectively, when a polarization filter selects out the parallel component of the signal. The background noise in the latter case where S/N = 3 is greatly reduced in comparison to the result illustrated in Fig. 4.2. This improvement arises from reduction of the background noise of the perpendicular to incident polarization component which is reduced by the analyzer. Additionally, some noise is reduced by the analyzer to a level below the threshold of the intensity which the streak camera can detect. The S/N is increased from 0.6 to 3. The temporal profile in Figs. 4.4 uses a space gate by selecting out a narrower spatial window (16 channels as compared to 120 channels as illustrated in Figs. 4.2), together with the aperture space gate and polarization filter. The slit cut mostly the off-axis light which has gone through the aperture due to the finite size of the apertures. There is a marked reduction in background noise and an enhancement in S/N to 14.

These results demonstrate that 10GHz signals going through a distance corresponding to 8.0 S_v can be clearly extracted. Considering the hazy weather (visibility<2.8km) and foggy weather (visibility<500m)[10], these distance ranges are excellent for local optical network. As a ‘last mile’ solution, the prospect to improve optical wireless using space and polarization gates for the application of optical wireless communication is very promising. Further experiments for longer transmission distance need to use the polarization analysis technique[11] which can eliminate the effect from the part of diffusion component that propagation in the incident light direction and maintain the same polarization state. The laser wavelength is another key parameter that will effect the signal transmission distance. Compared with the visible light center at 620 nm, near

infrared lasers will experience less atmospheric attenuation and an additional improvement by a slight absorption [12]. Self-mode-locked Cr^{4+}-doped lasers [13] can generate 50-fs pulses tunable from 1240 to 1270, and from 1350 to 1550 nm. These tunable lasers are ideal pulse laser sources for future free space wireless optical communication applications.

4.3 Time-resolved polarization to extract coded information from early ballistic and snake component through cloudy turbid media

Time-resolved polarization analysis can provide another novel approach to extract the early component of light in time for FSO application or underwater application. This approach is based on the depolarization property of the diffusive component of the signals and polarization property of the early ballistic and snake components of the signals. The ballistic photons are coherent scattered photons which propagate in the incident direction and traverse the shortest path. The snake-like photons scatter slightly in the forward direction and retain polarization properties, arrive later than ballistic and earlier than diffusive photons. Depolarization of an incident polarized beam occurs because of multiple scattering processes[14,15,16], where the direction of light in the scattering plane are randomly changed when photons interact with the randomly distributed scatterers. For linear polarized light, the depolarization distance [14,15] is on the order of transport length l_{tr}, the distance to randomize the direction of the light. One can define the polarization time difference function $\Delta I\ (t)$ between parallel light and perpendicular light:

$$\Delta I\ (t) = I_{\parallel}(t) - I_{\perp}(t) \tag{4.6}$$

where $I_{\|}(t)$ and $I_{\perp}(t)$ are the components parallel and perpendicular to incident polarization. For light completely depolarized by multiple scattering, the polarization difference ΔI (t) will be near zero. This occurs from the diffusive component (I_D) of the signals and the unpolarized natural light background. For extreme scattering case:

$$I_{\|}(t) \cong I_{B,S}(t) + I_D(t)/2 \tag{4.7}$$

and

$$I_{\perp}(t) \cong I_D(t)/2 \tag{4.8}$$

where $I_{B,S}(t)$ are ballistic and snake components and I_D is the diffusive component; therefore,

$$\Delta I(t) = I_{\|}(t) - I_{\perp}(t) = I_{B,S}(t) \tag{4.9}$$

The non-zero value of $\Delta I(t)$ occurs from early ballistic and snake components of the signals. The information is carried by ballistic and snake components.

In the past, a polarization analysis has been experimentally studied for the time-resolved [16] and for the continuous wave (CW) [17,18,19,20] cases. In these past experiments, the parallel polarized signal and the perpendicular polarized signal were separately recorded for different measurements. The results were then subtracted to obtain ΔI. For extracting the early component of light signals, one needs a technique to perform a time-resolved polarization analysis for both $I_{\|}(t)$ and $I_{\perp}(t)$ for light arrival. This approach can significantly improve the signal to noise ratio arising from changes in medium and laser pulse characteristics.

In this section, time-resolved polarization measurements and analysis for extracting information at the same time for a single and multiple pulses passing through a turbid medium is reported. This work demonstrates the improvement to extract information

from the early ballistic and snake components which can be distinguished and clearly extracted for single and multiple coded pulses through a turbid medium.

The experimental arrangement is shown schematically in Fig 4.5. Ultrafast laser pulses of 100fs are generated at a repetition rate of 82MHz by a colliding pulse mode-locked dye-laser system. The laser power is 5mw at a wavelength centered at 620nm. The laser beam, polarized by a Glan prism, is collimated and incidented into a sample of the turbid media contained in a 6cm(L)×6cm(W)×10cm(H) glass cell. The beam scattered out from the cell is measured by a polarization analyzer, which consists of a Wollaston prism combined with a synchroscan streak camera. The Wollaston prism splits the incident light into two polarized beams. One beam is parallel polarized and the another is perpendicular polarized to the incident pulse. The time profiles of the two polarized beams of light are recorded by a streak camera and analyzed using a computer. The intensity for $I_{\|}(t)$ and $I_{\perp}(t)$ is measured simultaneously. The accuracy in this experiment for change is $\Delta I / I \cong$ 0.01 to 0.03.

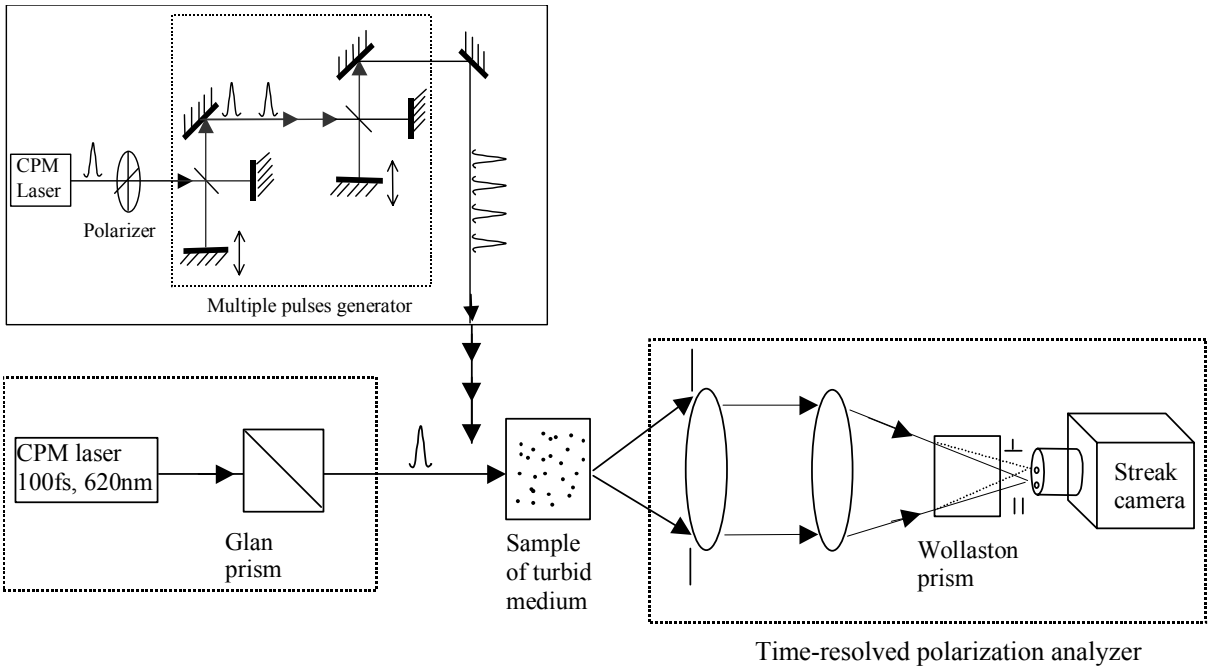

Fig. 4.5 Schematic diagram of the experimental arrangement for polarization analysis

The sample consist of diluted polystyrene solutions with relative refractive index m=1.20. Two kind of sizes of polystyrene particles in our experiment are used. The small particles with the diameter d=0.213μm have anisotropic factor g = 0.39 and the scattering cross section $\sigma_s = 0.376 \times 10^{-2}$ μm^2 computed according to Mie scattering formula [see chapter 1.2]. The large particles with the diameter d=0.855μm have the anisotropic factor g = 0.906 and the scattering cross section σ_s = 1.2265 μm^2. The scattering length is obtained by $l_s = 1/(\rho\, \sigma_s)$, where ρ is the density of particles counted by concentration of polystyrene, and the transport mean free length is $l_{tr} = l_s /(1 - g)$. The sample thickness L / l_s gives the scattering events inside the sample. For multiple pulses experiments, a mirror array system is used to produce a series of 4 coded pulses, as shown in the insert of Fig. 4.5. The duration between two pulses was set to 200 ps.

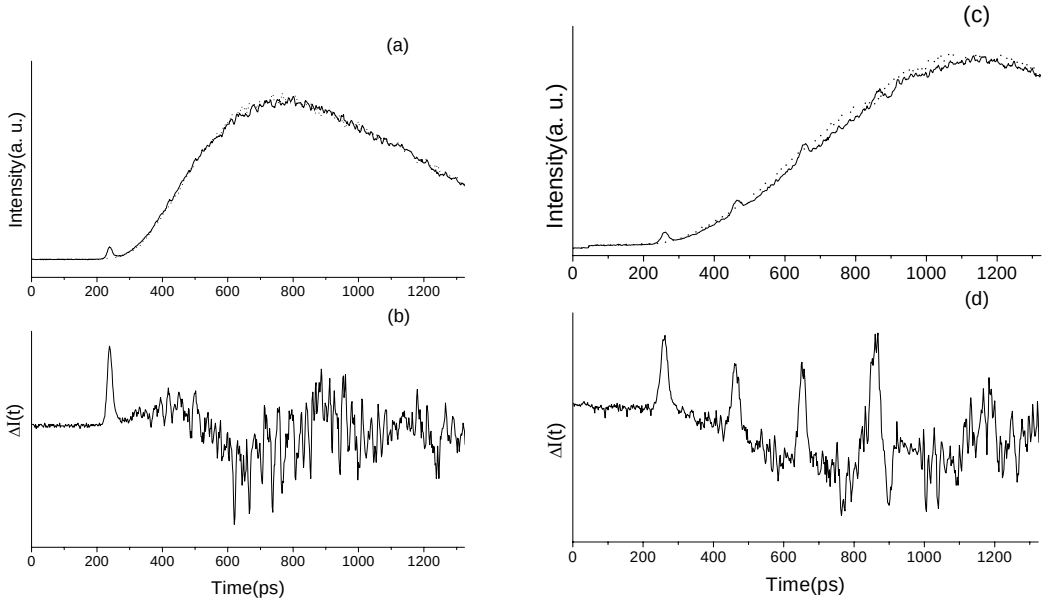

Fig. 4.6 Time-resolved profiles of received light through a turbid medium containing small particles with the diameter d = 0.213 μm. Fig. 4.6a shows the time-resolved profile for $I_{\parallel}(t)$ parallel (solid curve) and $I_{\perp}(t)$ perpendicular branches (dotted curve) of the received light for a single pulse; Fig. 4.6b shows the polarization difference ΔI (t). In this experiment for a single pulse, the scattering length l_s = 0.434 cm and the transport mean free length l_{tr} = 0.711 cm. Fig. 4.6c shows the time-resolved profile for parallel (solid curve) and perpendicular branches (dotted curve) of the received light for a series of 4 pulses and Fig. 4.6d shows the corresponding $\Delta I(t)$. In this experiment for pulse train, l_s = 0.463 cm and l_{tr} = 0.759 cm, the number of scattering events L / l_s is 13.

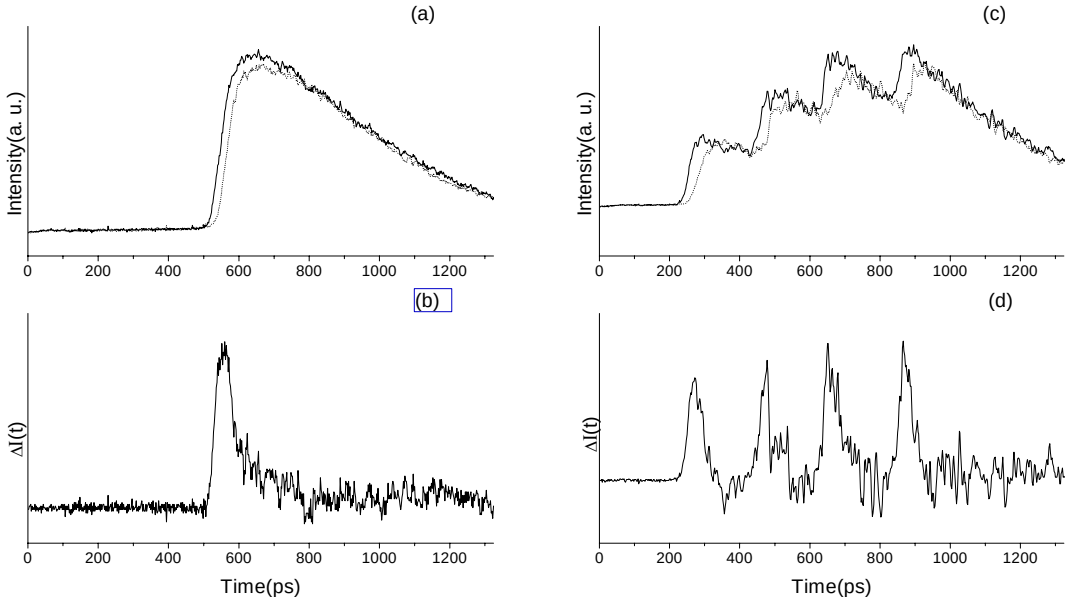

Fig. 4.7 Time-resolved profiles of received light through a turbid medium containing large particles with d = 0.855 μm. Fig. 4.7a shows the time-resolved profile for $I_{\parallel}(t)$ parallel (solid curve) and $I_{\perp}(t)$ perpendicular branches (dotted curve) of the received light for a single pulse; Fig. 4.7b shows the corresponding $\Delta I(t)$. In this experiment for single pulse, l_s = 0.063 cm, and l_{tr} = 0.67 cm. Fig. 4.7c shows the time-resolved profile for parallel (solid curve) and perpendicular branches (dotted curve) of the received light for a series of 4 pulses and Fig. 4.7d shows the polarization difference $\Delta I(t)$. In this experiment for pulse train, l_s = 0.086 cm and l_{tr} = 0.91 cm, the number of scattering events L / l_s is 70.

The experimental results for small and large sizes of polystyrene particles are shown in Figs. 4.6 and 7, respectively. In these experiments, the early signals are reduced due to multiple scattering inside the turbid solution as compared to the large diffusive component. When L / l_s = 12.9 for small particles and L / l_s = 69.8 for large particles, the information is overlapped by the diffusive light. As shown in Figs 4.6 and Fig. 4.7, using a time-resolved polarization analysis, the unpolarized diffusive component and natural light background for small and large particles are greatly reduced, these weak early signals are clearly extracted, and multiple pulses are distinguished. The experimental

results show evidence that the time-resolved polarization analysis provides a powerful technique to extract useful information in a light beam passing through a turbid medium.

From the differences shown in the time-resolved profiles in Fig. 4.6b, Fig 4.6d, Fig 4.7b and Fig. 4.7d, the ballistic signals are the main early component for small scatterers, and the snake signals are the main early component for large scatterers. Coexistence of the ballistic component and the scattered component is seen when the size of scatterers is much smaller than the wavelength of light, but is hardly seen when the size of scatterers is comparable to or larger than the wavelength of light. This phenomena occur because that scattering on a small particle is nearly isotropic, characterized by the small anisotropic factor g, while scattering on a large particle is strongly forward-like, characterized by $g \sim 1$. The transport mean free path l_{tr} is not much larger than the scattering length l_s in the case of small scatterers, while $l_{tr} >> l_s$ in the case of large scatterers. Beside the absorption effect, the ballistic component exponentially decay as $\exp(-L/ l_s)$ after traveling a distance L from the light source. The scattered component is characterized by l_{tr}, this result is supported by the fact that the diffusive constant $D = cl_{tr}/3$ by diffusion approximation or recently developed cumulant solution of the radiative transfer equation [21]. If one considers two cases with the similar magnitude of scattered component (that means their l_{tr} are nearly same), the ballistic component for the case of small scatterers could be strong enough to be seen, but too weak to be measured for the case of large scatterers. In the Fig 4.6, the size of the scatterer is small, so the ballistic component is obvious to been seen. In the Fig. 4.7, the ballistic peak becomes weak to be detected, what extracted is the component after a few scattering events but still flight along the forward direction denoted as the snake-like component.

In the atmosphere [22,23] from satellite to earth, the main light scattering events are with ice-crystals and large water drops in clouds, sizes of which are often larger than wavelength in visible and infrared region. Typically, the anisotropic factor $g \sim 0.9$ for cloud which is similar to the parameters of large particles in our experiments. To obtain an estimate of the value l_{tr}, we use the average mass density of cloud, about $0.06 g/m^3$, and the average radius of water drops, $a = 4$ μm. The density of water drops ρ is $\sim 2\times10^8$ / m^3. The scattering cross section $\sigma_s = 2\pi a^2$ estimated using the large sphere limit. The scattering length $l_s = 1/\rho\sigma_s \sim 50$m. Considering the anisotropic factor $g \sim 0.9$, the average value of $l_{tr} \sim 500$ m. According to the results(shown in Fig 4.7), the transmission distance of 6.6 $l_{tr} \sim 3.3$ km coded signal can be extracted using polarization analysis for the applications of optical wireless communication and target detection in the atmosphere. This range is excellent for local networks. Noise in the measured polarization data consists of intrinsic noise of light, that is the fluctuation of $\Delta I(t)$ from zero for unpolarized component in light, and measurement noise due to errors produced in the polarization analyzer. In order to extract a small polarized component from large unpolarized component, techniques in reducing measurement noise is essential. The polarization analysis approach present here can definitely improve free space optical wireless between source and detector over local networks.

4.4 Conclusion

In this chapter, we have demonstrated that spatial gating, polarization gating and polarization analysis can be used to efficiently enhance the signal-to-noise by reducing the diffusive background from the ballistic and snake-like component. A 10GHz pulse

train is extracted after going through a distance corresponding to 8.0 S_v or 6.6 l_{tr}.. These results show a promising application over local network or underwater covert communication using ultrashort pulses. Further work in the forward signal detection will use circularly polarized light, which depolarizes slower than the linearly polarized light [15].

References

1. D. Killinger, Opt. Photon. News **13** 10, 36 (2002).
2. A. Acampora, Scientific American, 49 (July, 2002).
3. K. M. Yoo and R. R. Alfano, Opt. Lett. **15,** 320 (1990).
4. L. Wang, P. P. Ho, C. Liu, G. Zhang, and R. R. Alfano, Science **253,** 769 (1991).
5. J. J. Dolne, K. M. Yoo, F. Liu and R. R. Alfano, Laser Life Sci. **6**, 131 (1994).
6. H. Horinaka, K. Hashimoto, K. Wada, Y. Cho, and M. Osawa, Opt. Lett. **20,** 1501 (1995).
7. L. Wang, P. P. Ho, X. Liang, H. Dai, and R. R. Alfano, Opt. Lett. **18**, 241 (1993).
8. K. C. Young, *Microphysical Processes in Clounds* (Oxford University Press, New York, 1993).
9. Kuo-Nan Liou, *An Introduction to Atmospheric Radiation* (Academic Press, New York, 1980).
10. I. Kim, R. Stieger, J. A. Koontz, C. Moursund, M. Barclay, P. Adhikari, J. Schuster, E. Korevaar, R. Ruigrok, and C. DeCusatis, Opt. Eng. **37,** 3143 (1998).
11. X. H, Ni, Q. R. Xing, W. Cai, and R. R. Alfano, Opt. Lett. **28**, 343 (2003).
12. K. M. Yoo, Feng Liu, and R. R. Alfano, Opt. Lett. **16**, 1068 (1991).
13. A. Seas, V. Petričević, and R. R. Alfano, Opt. Lett.**18**, 891 (1993).
14. A. D. Kim and M. Moscoso, Phys. Rev. E. **64**, 026612(2001).
15. E. E. Gorodnichev, A. I. Kuzovlev, and D. B. Rogozkin, JETP Lett. **68**, 22(1998)
16. S. G. Demos and R. R. Alfano, Opt. Lett. **21**, 161 (1996).
17. S. P. Morgan, M. P. Khong, M. G. Somekh, Appl. Opt. **36**, 1560 (1997).

18. M. J. Rakovic, G. W. Kattawar, M. Mehrubeoglu, B. D. Cameron, L. V. Wang, S. Rastegar, G. L. Cote, Appl. Opt. **38**, 3399 (1999).

19. G. Yao, L. V. Wang, Opt. Lett. **24**, 537 (1999).

20. J. M. Schmitt, A. H. Gandjbakhche, and R. F. Bonner, Appl. Opt. **31**, 6535 (1992).

21. W. Cai, M. Lax, R. R. Alfano, Phys. Rev. E **63**, 016606 (2001).

22. Smith, F., The Infrared and Electro-Optical Systems Handbook *Atmospheric Propagation of Radiation*, Vol. 2, SPIE Press (1993).

23. E. P. Zege, A. P. Ivanov, and I. L. Katsev, *Image transfer through a scattering medium* (Springer-Verlag, Berlin-Heidelberg, 1991).

Chapter 5

Precursor propagation through linear (dielectric-like) media

5.1 Introduction

In this chapter we consider the propagation of short pulse in a dielectric medium described by a Lorentz model. Especially, we focus on resolving recent controversy on observation of optical precursor in water. There has been a growing interest in this question in recent years as researchers have focused on utilizing laser pulses in femtosecond and attosecond time region to study new materials, information processing, biomedical systems and for non-invasive medical diagnostics. Precursors are believed to travel deeper into medium since their attenuation is given by non-exponential polynomial form $1/z^n$ (z is the propagation distance). Generating and controlling precursors could enhance medical imaging and also have significant applications for the military and in homeland security.

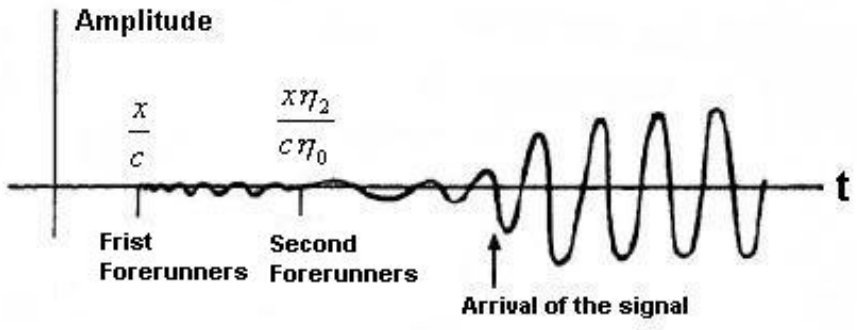

Fig.5.1 Illustrating the arrival of the sommerfeld, Brillouin precursors and the signal. [L. Brillouin, *Wave Propagation and Group Velocity*, (Academic, New York, 1960)]

Fig.5.1 illustrates the arrival of precursors and signal. The phenomenon of precursors was described by Sommerfeld and Brillouin[1,2,3], who realized that some frequency

components of a wide spectrum pulse has to propagate at or very close to light-in-vacuum velocities. These components are attenuated less than the signal components whose frequencies lie closer to the absorption band and add up to a significant contribution after a sizable flight path in the medium. These ideas were taken up by Baerwald[4] and a number of authors [5,6,7,8].

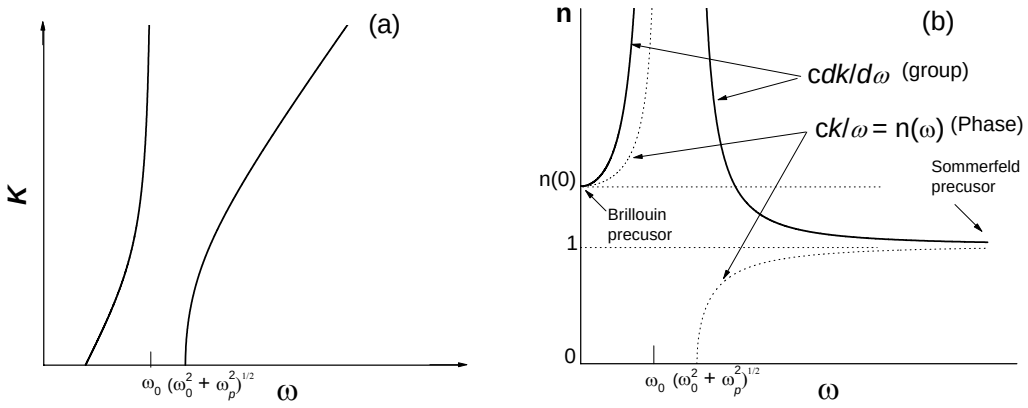

Fig.5.2 a) Dispersion relation and b) $cdk/d\omega$ and ck/ω versus frequency for Lorentz model (Equ.5.3, ω_0 = 40/fs, ω_p = 44.7/fs) without damping. The Sommerfeld precursor is formed around the infinite frequency where the phase velocity and group velocity are close to speed of light in vacuum *c*. The Brillouin precursor is formed around the zero frequency where the group velocity and phase velocity is close to *c*/n(0).

For a simple resonant Lorentz model without damping, Fig.5.2(a) shows the dispersion relation and Fig.5.2(b) shows the functions $cdk/d\omega$ and ck/ω versus frequency. There are three types of precursors that represent the transient of the medium to an incoming electromagnetic pulse [9]. The initial precursor is due to the inertia of the electrons in the medium, the first photons in the propagating pulse go through the medium at the speed of light in vacuum, as if the medium were not present. These

photons have never been observed and are most likely too few in number ever to be detected. The second precursor (Sommerfeld) consists primarily of the original pulse's high-frequency photons and propagates through the medium at almost the speed of light (in vacuum) and with relatively minor interactions with the medium [see Fig.5.2(b)]. This precursor also carries little energy. The third precursor (Brillouin) can contain significant amounts of energy and comes from the low-frequency [zero frequency in Fig.5.2(b)] photons present in a broadband pulse. It can arrive either before or after the main pulse, depending on the wavelength-dependent properties of the medium.

The first direct experimental search for precursors was reported in 1969 by Pleshko and Palócz [10] using microwave in a waveguide with a controllable stop band. In this case of a well-defined artificial medium, the high-frequency Sommerfeld precursor and low-frequency Brillouin precursors were clearly identified.

In a recent Letter [11], Choi and Osterberg(**CO**) proposed to have observed "optical precursors" in water using a 540 fs supercontinuum pulse about 780 nm propagating through a very long distance in water on order of meters. Their claim relies largely on a const 1/z fit to energy and pulse breakup at the long distance. We disputed this claim [11].

We will first demonstrate the formation of Brillouin precursor for Lorentz medium using numerical calculation. Then, we disproved the recent claim by CO of the observation of precursor in water using experiments and gave an alternate explanation for their observation in term of distortion due to absorption and dispersion effect [11].

5.2 Formation of Brillouin precursors

The integral representation of the propagated plane wave pulses is given by

$$A(z,t) = \frac{1}{2\pi}\int_{-\infty}^{+\infty} d\omega E(0,\omega)\exp[i(kz-\omega t)] \tag{5.1}$$

where $k = n\omega/c$ and

$$E(0,\omega) = \int_{-\infty}^{+\infty} E(0,t)e^{i\omega t}dt \tag{5.2}$$

For a dielectric Lorentz medium with a single resonance frequency at ω_0 the complex index of refraction n is given by

$$n^2(\omega) = 1 - \frac{\omega_p^2}{\omega^2 - \omega_0^2 + i\gamma\omega} \tag{5.3a}$$

Where ω_0 is the resonant frequency, ω_p is the plasma frequency of the medium and γ is the damping constant. For large frequencies the index of refraction goes as

$$n^2(\omega) \to 1 - \frac{\omega_p{}^2}{2\omega^2} \tag{5.3b}$$

the refraction index n(ω) is close to 1 for infinite frequency, the light travels at a speed close to c.

Here we follow Jackson's use of "Method of Stationary Phase" to gain a qualitative understanding of the amplitude (Eq.5.1) at various times [12], the damping constant is ignored (γ=0). A more rigorous and more accurate method of steepest descent is presented by Sommerfeld and Brillouin [1] as well as other researchers [13].

The method of stationary phase addresses itself to the problem of evaluating approximately integrals of the general type

$$I = \int F(\omega)e^{i\phi(\omega)}d\omega \tag{5.4}$$

where $F(\omega)$ is a function that varies relatively slowly with ω and $\phi(\omega)$ is a phase that is generally large and rapidly varying. The rapid oscillations of $e^{i\phi}$ over most the range of integration mean that the integrand averages to almost zero. Exceptions to this cancellation occur only when $\phi(\omega)$ has an extremum. The integral can therefore be estimated by finding the places where $\phi(\omega)$ has a vanishing derivative, evaluating approximately the integral in the neighborhood of each of these points, and summing the contributions.

Let $\phi(\omega)$ have a vanishing first derivative at $\omega = \omega_s$. In the neighborhood of this point, $\phi(\omega)$ can be expanded in Taylor series:

$$\phi(\omega) = \phi_s + \tfrac{1}{2!}\phi_s''(\omega - \omega_s)^2 + \tfrac{1}{3!}(\omega - \omega_s)^3 + \cdots \tag{5.5}$$

In Equ.(5.1), the phase $\phi(\omega)$ is expressed by:

$$\phi(\omega) = k(\omega)x - \omega t \tag{5.6}$$

The points of stationary phase defined by $\partial\phi/\partial\omega = 0$ satisfy the condition,

$$\frac{cdk}{d\omega} = \frac{ct}{x} \tag{5.7}$$

At time t, the points of the stationary phase is at that frequency ω whose group velocity is x/t. For time immediately after $t_0 = x/c$, the point of stationary phase is given by

$$\omega_s \cong \omega_p \sqrt{\frac{t_0}{2(t - t_0)}} \tag{5.8}$$

Evaluating Equ. (5.1) using Equ.(5.5) till second derivative at large frequency gave us the earliest arrival signal, called first or Sommerfeld precursor. The amplitude of this part of signal is very small.

At later times, the point of stationary phase moves to lower frequencies. In general the amplitude remains very small. Only when the elapsed time t_1(the arrival of zero frequency component or Brillouin precursor) reaches

$$t_1 = k'(0)z = \frac{n(0)z}{c} \tag{5.9}$$

is there a qualitative change. At this point, the amplitude of oscillation is a considerably larger than before and of relatively long period. The second and third derivative of $k(\omega)$ is given as:

$$\frac{d^2k}{d\omega^2} = \frac{\omega}{c}\frac{d^2n}{d\omega^2} + \frac{2}{c}\frac{dn}{d\omega} = 0 \quad for\ \omega = 0\ and\ \gamma = 0 \tag{5.10}$$

$$\frac{d^3k}{d\omega^3} = \frac{\omega}{c}\frac{d^3n}{d\omega^3} + \frac{3}{c}\frac{d^2n}{d\omega^2} = \frac{3{\omega_p}^2}{cn(0){\omega_0}^4} \quad for\ \omega = 0\ and\ \gamma = 0 \tag{5.11}$$

The second derivative is vanished which means that $\phi_s'' = 0$ ($\omega = 0$). The $\phi(\omega)$ is expanded as

$$\phi(\omega) \cong \phi(0) + \frac{\phi'''}{3!}\omega^3 = \omega(t_1 - t) + \frac{x}{6}\left(\frac{d^3k}{d\omega^3}\right)_0 \omega^3 \tag{5.12}$$

The amplitude of Equ.(5.1) is therefore given approximately by

$$A(z,t) \cong \frac{1}{2\pi}\int_{-\infty}^{+\infty} d\omega E(0,\omega = 0)e^{i\omega(t_1 - t) + i(z/6)\left(d^3k/d\omega^3\right)_0 \omega^3} \tag{5.13}$$

Change of variable $\nu = \sqrt{\frac{z}{2|t - t_1|}\left(\frac{d^3k}{d\omega^3}\right)}\omega$, this integral can be written as

$$A(z,t)=\begin{cases}\frac{1}{2\pi}\left[\dfrac{3x}{z\left(\dfrac{d^3k}{d\omega^3}\right)_0}\right]^{1/3}\int_0^\infty\cos\left[\frac{3}{2}x\left(\dfrac{v^3}{3}+v\right)\right]dv & t_1>t\\ \frac{1}{2\pi}\left[\dfrac{3x}{z\left(\dfrac{d^3k}{d\omega^3}\right)_0}\right]^{1/3}\int_0^\infty\cos\left[\frac{3}{2}x\left(\dfrac{v^3}{3}-v\right)\right]dv & t_1<t\end{cases} \tag{5.14}$$

where $x=\dfrac{2\sqrt{2}\left|t-t_1\right|^{3/2}}{3\left(z\dfrac{d^3k}{d\omega^3}\right)_0^{1/2}}$ and

$$\int_0^\infty\cos\left[\frac{3}{2}x\left(\frac{v^3}{3}\pm v\right)\right]dv=\begin{cases}\frac{1}{\sqrt{3}}K_{1/3}(x) \;\to\; \frac{1}{\sqrt{3}}\frac{\Gamma(1/3)}{2}\left(\frac{2}{x}\right)^{1/3} & t_1>t\\ \frac{\pi}{3}\left[J_{1/3}(x)+J_{-1/3}(x)\right]\to\frac{\pi}{3}\left[\frac{1}{\Gamma(4/3)}\left(\frac{x}{2}\right)^{1/3}+\frac{1}{\Gamma(2/3)}\left(\frac{x}{2}\right)^{-1/3}\right] & t_1<t\end{cases} \tag{5.15}$$

where J is the Bessel function and K is the modified Bessel function of the second kind.

The amplitude A(z,t) can be written as:

$$A(z,t)\approx z^{-1/3}\frac{1}{2\pi}\left[\frac{3}{\left(\dfrac{d^3k}{d\omega^3}\right)_0}\right]^{1/3}\begin{cases}\times 3^{-1/2}\Gamma(1/3)2^{-2/3} & t_1>t\\ \times\frac{\pi}{3}\frac{1}{\Gamma(2/3)}2^{1/3} & t_1<t\end{cases} \tag{5.16}$$

The amplitude is decayed nonexponentially ($z^{-1/3}$).

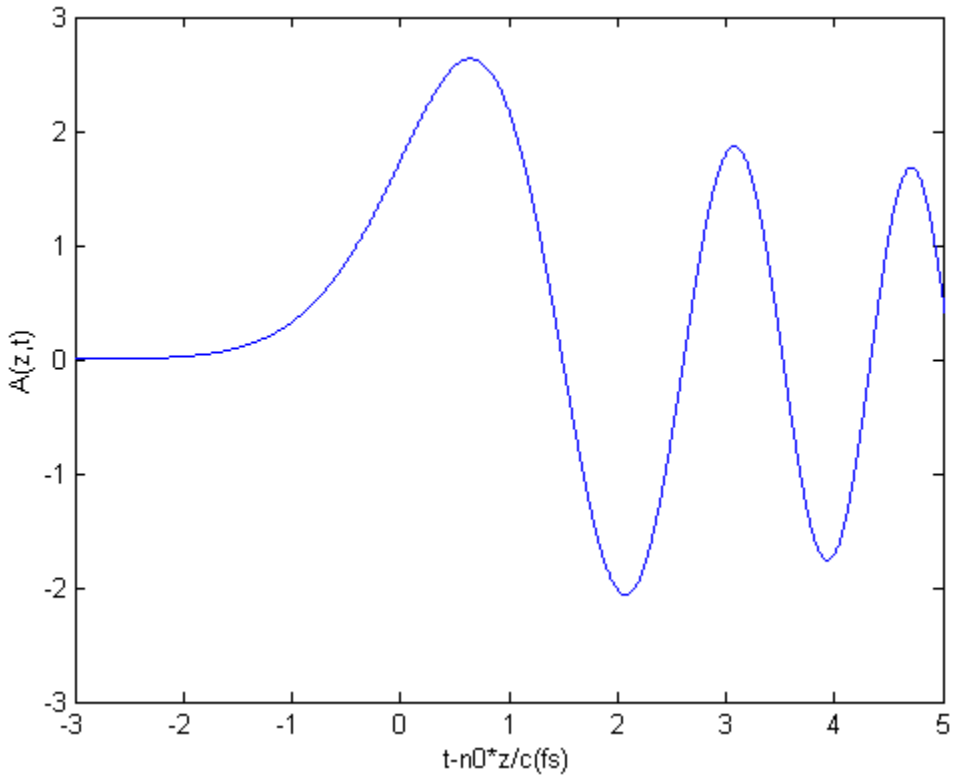

Fig.5.3 The approximate behavior Brillouin precursor as a function of time. ω_0 = 40/fs, ω_p = 44.7/fs (Equ.5.3). The original point '0' in the X-axis represents the arrival of zero frequency component.

Equ.(5.14) describes the second precursor – Brillouin precursor, which is of much lower frequency than the first. Choose ω_0 = 40/fs, ω_p = 44.7/fs, and n(0)=1.4996 (we will use the same parameters later), the approximate behavior of the second precursor (Brillouin) is illustrated in Fig.5.3.

Equ.(5.14) and (5.15) show that the large-depth, fixed-relative-time ($|t-t_1|$) values of the Brillouin precursor decay as $z^{-1/3}$. This kind of polynomial algebraic decay ($\sim z^{1/n}$) causes interests in the applications such as free-space communications and medical imaging [11,14], In those applications, the attenuation of signal follows Beer's law (exponential decay) and decay much faster than algebraic decay for large depth.

However, we should point out that the $z^{-1/3}$ dependence of amplitude is a result of the dispersion of the index of refraction n not the absorption α. The absorption, which is actually connected with the exponential decay, is ignored in Jackson's derivation using method of stationary phase. The pulse shape, which is a result of the interference of light of different frequencies around zero-frequency, is broadened with the increase of depth due to the frequency dependence of the refraction index n. $z^{-1/3}$ dependence of amplitude is the consequence of pulse broadening. Mathematically, there is an explicit dependence on z in the denominator of amplitude $A(z, t)$, which is linked to the second derivative of $\phi(\omega)$ [Equ.(5.4)] and stationary phase method. In the evaluation of self-phase modulation for an intense pulse going through condensed matter, Alfano [15] also used the stationary phase method and obtained the $1/z$ dependence for the intensity spectrum $S(z)$. The $1/z$ dependence is a consequence of spectrum broadening which depends on z. In that case, the extent of the spectrum-broadening ($\Delta\omega$) is proportional to the distance z; $S(z)\cdot\Delta\omega$ is a constant [15].

The above stationary method ignored the absorption α and used constant incident amplitude [$E(0,\omega=0)$]. To obtain the evolution dynamics of Brillouin precursors, a more accurate method should be applied to solve the integral Equ.(5.1). Sommerfeld and Brillouin performed an asymptotic analysis using the method of steepest descents in evaluating the integral in Equ.(5.1) with absorption. They showed a $z^{-1/2}$ decrease in intensity, and beside this has an absorption which increases exponentially with depth [1]. Several groups have improved on the early analysis of Sommerfeld and Brillouin [16,17]. However, the complicated asymptotic analysis gave no physical explanation of the results. Here we solve the integral Equ.(5.1) using numerical method to evaluate the

effect of dispersion and absorption on the formation of Brillouin precursor, the results are compared with Oughstun's results [13] obtained with asymptotic analysis

For an input Gaussian pulse-modulated sine wave:

$$E(0,t) = e^{-t^2/T^2} \sin(\omega_c t) \tag{5.17}$$

The propagated field is then given by

$$E(z,t) = \frac{T}{2\pi^{1/2}} \mathrm{Re}\, i\left\{ \int_{-\infty}^{+\infty} e^{-(T^2/4)(\omega-\omega_c)^2} e^{i(kz-\omega t)} d\omega \right\} \tag{5.18}$$

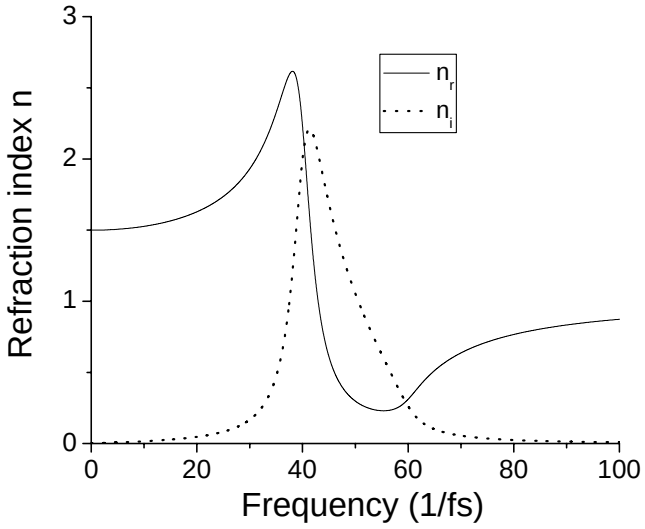

Fig.5.4 Real (n_r) and imaginary (n_i) part of the refraction index of the Lorentz dielectric medium ω_0 = 40/fs, ω_p = 44.7/fs and γ = 5.6/fs.

The parameters for the Lorentz medium are chose as suggested by Brillouin [1]: ω_0 = 40/fs, ω_p = 44.7/fs and γ = 5.6/fs. The incident pulse width is 2T=0.314 fs, and carrier frequency is ω_c =10/fs. Fig.5.4 shows the refraction index of the Lorentz medium. The imaginary part of the refraction index around zero frequency is close to zero and increasing quickly with the increase of frequency.

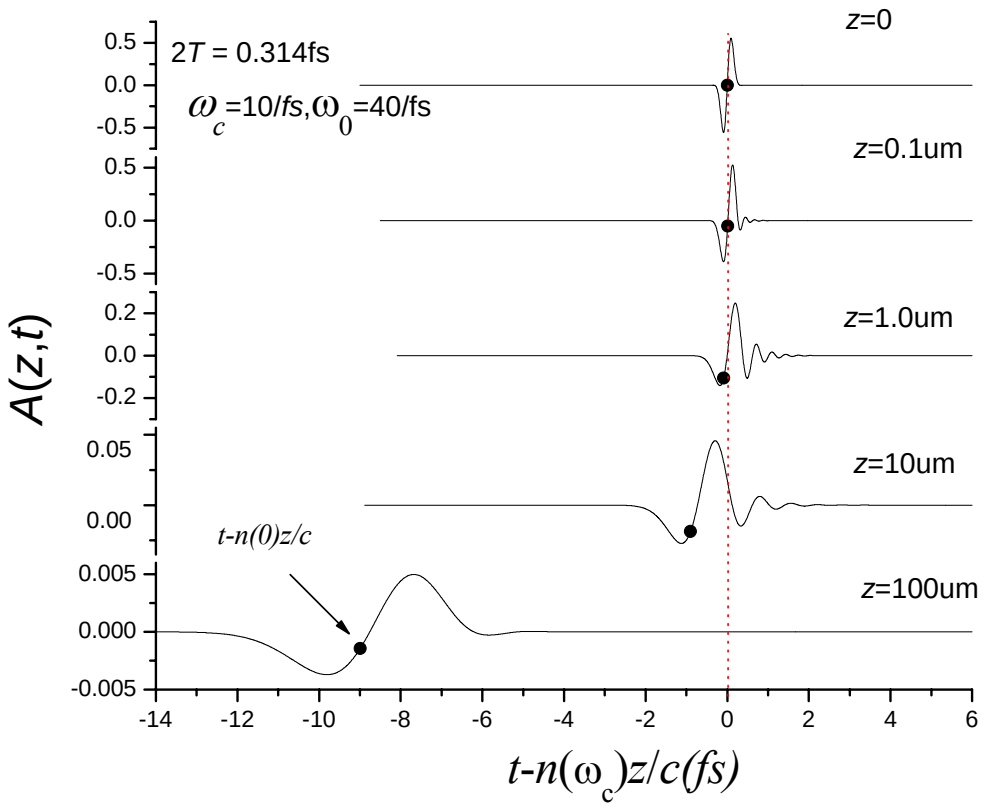

Fig.5.5 Numerically determined dynamical evolution of the propagated field for an input Gaussian-modulated sine wave with initial pulse width $2T=3.14\times10^{-16}$s and below resonance carrier frequency $\omega_c=1\times10^{16}$/s (λ=188.49 nm, T=107 as). The dot represents the arrival of zero frequency component in the spectrum.

Fig.5.5 shows the evolution of the input Gaussian-modulated sine pulse with the increase of propagation distance. The relative zero point in the figure indicates the arrival of the frequency component of the carrier frequency. The value $t\text{-}n(0)z/c$ corresponds to the arrival of zero frequency component. The attenuation of the frequency component in the incident pulse is increased with the increase of the frequency. Consequently, as the propagation distance increases, the location of peak amplitude shifts toward the space-time $ct/z=n(0)$ where the attenuation vanishes and the temporal profile of the incident

pulse broaden. It is clearly shown that after the propagation distance of 100 μm, the peak around the carrier frequency disappeared, the Brillouin precursor is formed around the zero frequency component. These results are consistent with Oughstun's asymptotic analysis (Oughstun made an apparent mistake in the scale of propagation distance) [13].

To further clarify the behavior and qualitatively distinguish the dispersion and absorption contribution of the medium in the formation of Brillouin precursor, we numerically evaluated Equ.(5.1) with constant value of the real part of the complex refraction index, for example, the value at carrier frequency.

Fig.5.6 shows the evolution of the input Gaussian-modulated sine pulse with constant real part of refraction index. In this figure, the ripple tail around the space-time $ct/z=n(\omega_c)$ disappeared, absorption cause the temporal broadening. The frequency dependent of the real part of the refraction index or dispersive propagation results in the ripple at the tail for the space-time $ct/z=n(\omega_c)$ in Fig.5.5. However, after propagating enough distances, this kind of oscillatory tail vanishes in both Fig.5.5 and 5.6 since the curve of the real part of refraction index is really flat around zero frequency.

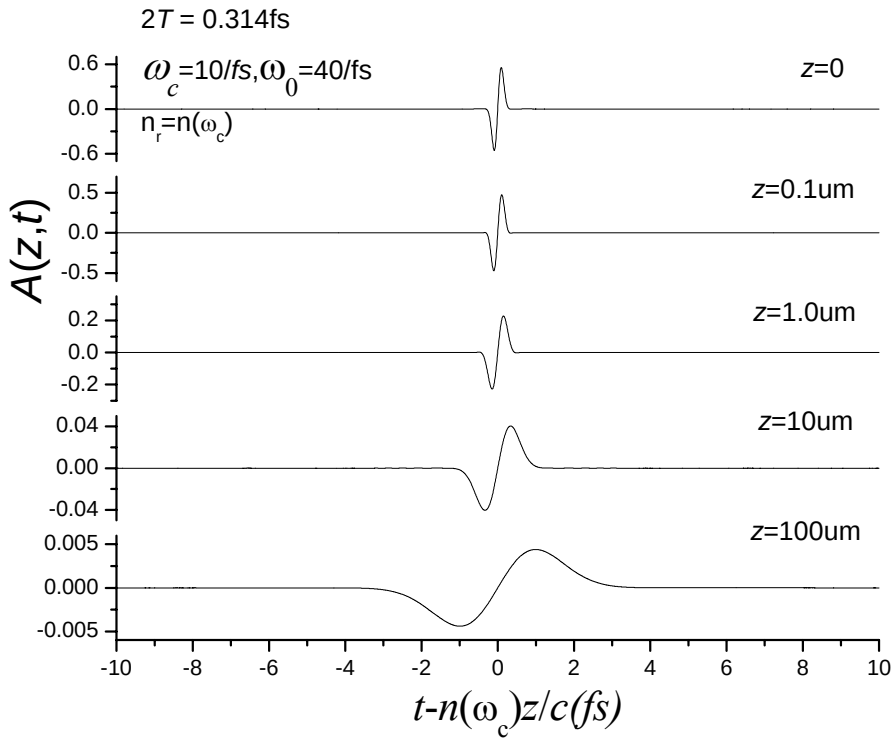

Fig.5.6 Numerically determined dynamical evolution of the propagated field for an input Gaussian-modulated sine wave with initial pulse width $2T=3.14\times10^{-16}$s and below resonance carrier frequency $\omega_c=1\times10^{16}$/s. The real part of refraction index is set to constant value, the value at the carrier frequency.

The parameters Brillouin and Oughstun used requiring a central wavelength of 188.4 nm and pulse width of 0.314fs. It is hard to prepare this kind of pulse at this stage. Both the Sommerfeld and the Brillouin precursor have been detected experimentally for the propagation of microwave waveguide [10]. However, precursors in the optical region are difficult to be observed because of the high carrier frequency, narrow spectrum and lack of appropriate materials. Although there have been a few reports on the experimental observation of optical precursors [18,19,20], a clear peak separation from the main pulse has not been observed and an analysis of precursors has not been attempted.

Recently, progress in the terahertz (THz) region [21,22] has opened up an important frequency region to explore the problem of Brillouin precursors at low frequencies. This kind of submillimeter wave contains enough near zero frequency components, it is easy to find a Lorentz medium have a resonant frequency above the Thz wave. Most important, both the amplitude and the phase of the electric field of the THz pulse can be detected using photoconductive dipole antennas [22,23] or electro-optic sampling [24] techniques, which allows us to explore the field structure of the precursors.

Here, we applied the use of the ZnTe as the semiconductor crystal for generation of Thz pulse and precursor. The dielectric response of ZnTe can be written as:

$$n(\omega) = \sqrt{\varepsilon(\omega)} = \left(\varepsilon_{el} - \frac{\varepsilon_{st}\omega_{TO}^2}{\omega^2 - \omega_{TO}^2 - 2i\gamma\omega} \right)^{1/2} \tag{5.19}$$

with ε_{st} being the contribution of the TO resonance to the static dielectric constant, ω_{TO} the angular resonance frequency, and γ the damping. For ε_{st} we used 6.0, for ω_{TO} we took the value 33.3 THz [25,26,27]. For the input pulse shape we used the time derivative of a Gaussian:

$$E(0,t) = (t/\sigma)e^{-2(\ln 2)t^2/\sigma^2} \tag{5.20}$$

where σ=100fs. The spectral distribution $E(0,\omega)$ can be written as

$$E(0,\omega) = -i\frac{\sqrt{\pi}\sigma^2(\omega - \omega_c)}{4\sqrt{2}(\ln 2)^{3/2}} e^{-\sigma^2(\omega-\omega_c)^2/8\ln 2} \tag{5.21}$$

ω_c = 6.4477 THz is carrier frequency. Numerically evaluate Equ.(5.1) using Equ.(5.20), we obtained a result as shown in Fig. 5.7.

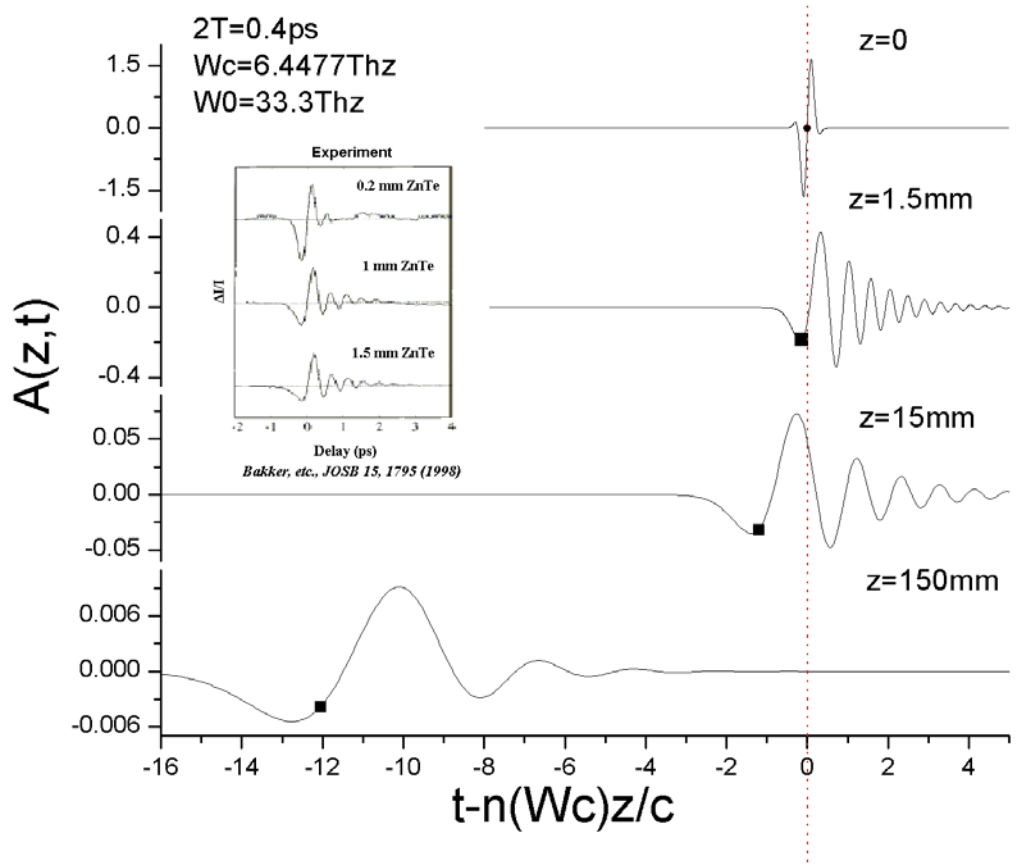

Fig.5.7 Numerically determined dynamical evolution of the propagated field for an input THz wave in ZnTe crystal. The dot represents the arrival of zero frequency component in the spectrum The inset is Bakker, *etc*.'s experimental results.

In Fig. 5.7, the origin '0' of the X-axis is the relative time of the arrival of main signal and the point 't-n(0)z/c' is the relative time of arrival of zero frequency component. Clearly, Brillouin precursor is separated from the main signal after 15cm sample and the main signal is vanished due to the absorption at this distance. The numerical results in Fig.5.7 is consistent with the experimental measurement by Bakker, *etc*.[25] at short distances (see Bakker's experimental result in the inset of Fig.5.7). However, in their measurement, the sample is not thick enough (maximum 1.5 mm in their measurement) to observe the separated Brillouin precursor and they contributed their observation as

distortion. The results presented in Fig.5.7 demonstrated that THz wave provides a practical method to explore the precursor phenomena.

5.3 Are precursors observed in water?

In a recent Physical Review Letter [11], Choi and Osterberg(**CO**) proposed to have observed "optical precursors" in water using a 540 fs supercontinuum pulse about 780 nm propagating through a very long distance in water. Their peak power was below the onset of nonlinear effects.

The apparent observation by CO made a stir; therefore, when Choi and Österberg published their result in *Physical Review Letter*. Water is a major component in human body. The experimental was hailed as the first complete demonstration of the Brillouin precursor using visible light. Such a discovery might one day have significant consequences in medical imaging, underwater communications, and also have significant applications for the military and in homeland security. However, after a carefully reading of Choi and Österberg's work, we believe that precursors have not been observed by **CO**. Our alternate explanation is that pulse breakup is due to vibration overtone absorption and dispersion in water. In addition, there are several inconsistencies in their data.

As we discussed in Chapter 5.2, Brillouin precursors arise from DC or near zero frequency component in the incident pulse, it is one kind of asymptotic behavior around the zero frequency for a Lorentz medium. Instead of totally energy loss of the pulse, $1/z$ factor in Brillouin's expression [1] as well as others authors [11,13] represents the reshaping of pulse due to dispersive propagation of pulse in the medium. The slowly decay of Brillouin precursor actually come from the ignorable absorption at near zero

frequencies in comparison with the carrier frequency of the signal. In Choi and Österberg's experiement, there are negligible "real" low frequencies of 540 fs, 60 nm broad pulse propagating in water. Or even if the near zero frequency component exists, it is impossible for the optical detector that they are using to detect it. The slow attenuation behavior in their experiment is strange and deserve more careful experiments to identify it.

Pulse breakup at large propagation distance is other evidence for their announcement of observation of precursor. **CO** did eliminate some of the nonlinear effects in water by propagating a weak broadened pulse. The authors, however, ignored the existence of a vibrational overtone absorption band centered at 760 nm for broad bandwidth pulse.

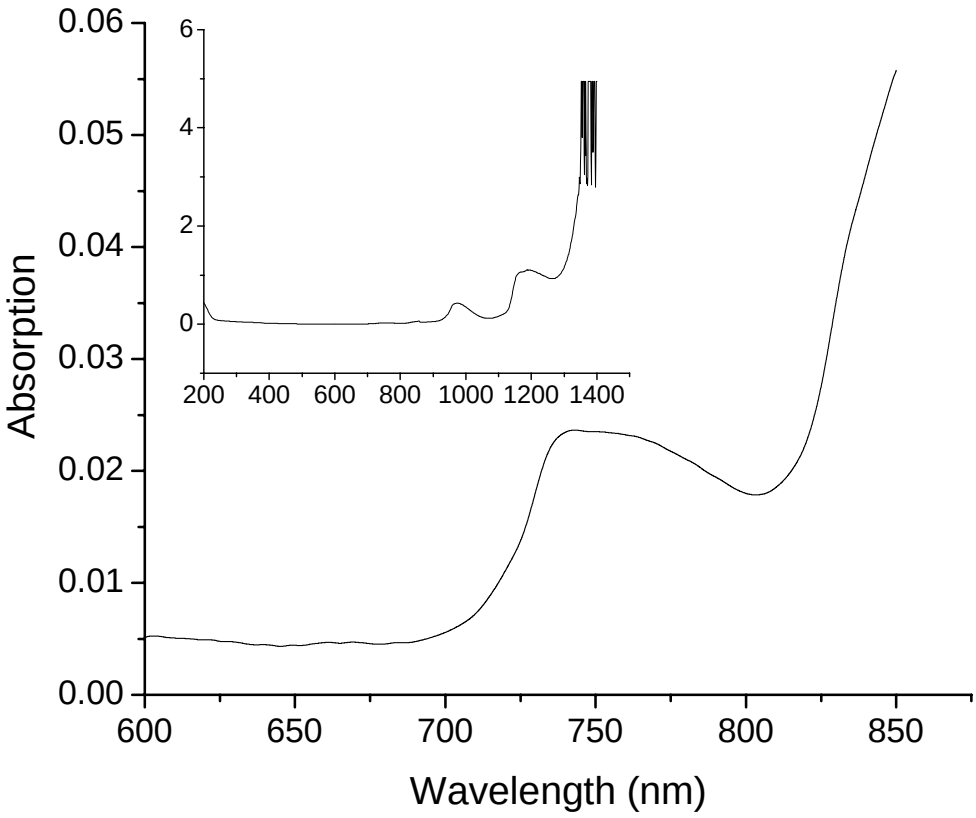

Fig.5.8 The absorption [-ln(transmission)] of water of 20mm.The inset is the absorption over the wavelength of 200-1600 nm.

Fig.5.8 shows the absorption of water over the wavelength of interest. There exists overtone absorption band around 760 nm. To simulate the effect of the absorption band to the pulse profile, we just need to evaluate Equ.(5.1) with the complex index of water and incident pulse profile. However, Choi and Österberg broaden the pulse spectrum with fiber. In order to evaluate Equ.(5.1), more parameters are needed to simulate the self-phase modulation [see Equ.(6.13) in chapter 6] and linear chirp (an additional $-i\beta t$ term in phase of the optical field) in the pulse. Instead, we performed experiments to confirm our model that overtone absorption distorts the temporal and spectral profiles. The

experimental arrangement is shown schematically in Fig 5.9. A 100 fs pulse centered at 780 nm was sent through a 30 cm single mode fiber, then the broadened pulse propagated through the water. The spectrum [Figs. 5.10 and 11(a)] and temporal profile [Figs. 5.10 and 11(b)] of pulse before and after propagating a distance of 1.2 m in water were measured using a spectrometer and a 2.5 ps streak camera.

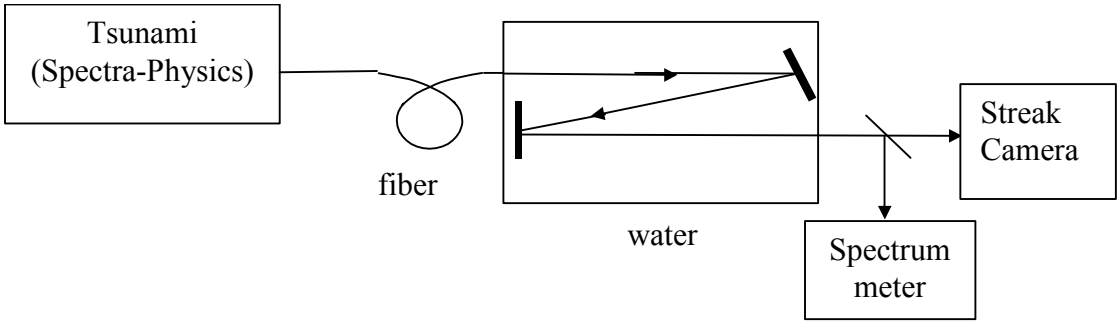

Fig.5.9 Schematic diagram of the experimental setup for broad-band pulse propagation through water

The results showed that both the spectrum [Fig. 10(a)] and temporal profile [Fig. 10(b)] of the laser pulse are smooth before going through the water. However, at a lower laser output power (measured immediately after the fiber) of 200 mW [dotted curve in Fig. 5.10(b)], the spectrum was not broadened enough by the fiber, both spectrum and pulse didn't split after going through the water [dotted curve in Figs.5.11(a) and (b)]. When we increased the laser output to 350 mW [solid curve in Fig. 5.10(b)], the spectrum [solid curve in Fig. 5.10(a)] is broadened enough to cross the absorption band centered at 760 nm, a spectrum peak is formed around 750 nm which is accompanied by split pulse [solid line in Figs.11(a) and (b)]. More experimental results with different filters and different water pathlength from 0.6 m to 3 m showed that the bandwidth is a critical parameter for observation of the pulse split. A spectrum narrower than 50 nm makes it

hard to obtain this split since the bandwidth is not wide to cross the absorption band at 760 nm and no perceptible spectral split formed.

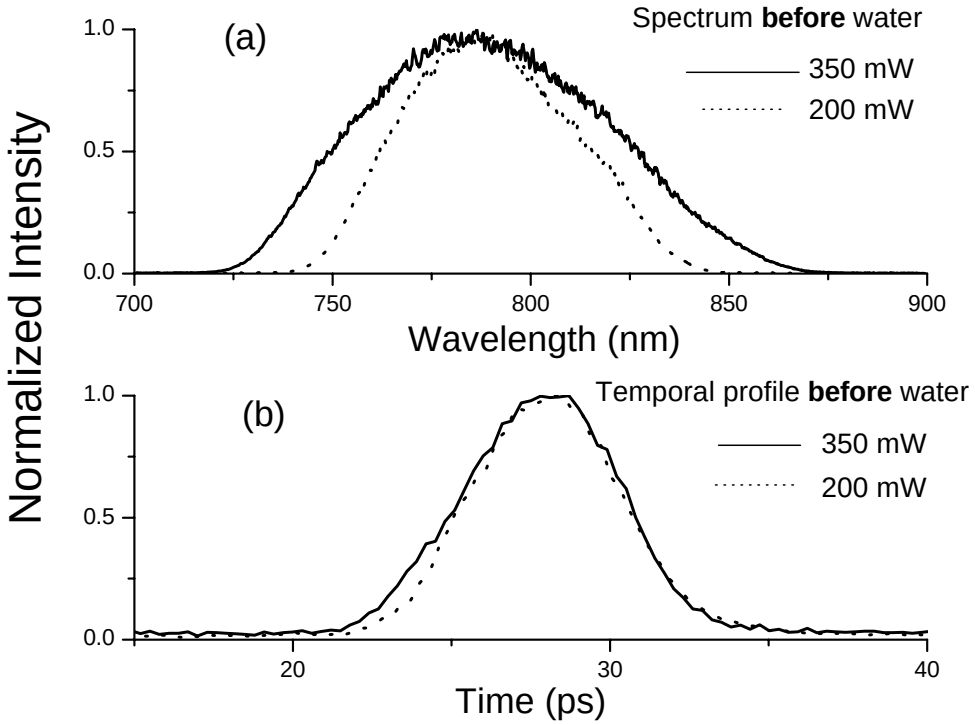

FIG. 5.10 Spectrum (a) and temporal profile (b) of the pulse **before** going through 1.2 m of water. The dotted curve and solid curve represent a laser input power of 200 mW and 350 mW, respectively. The time axis is relative time.

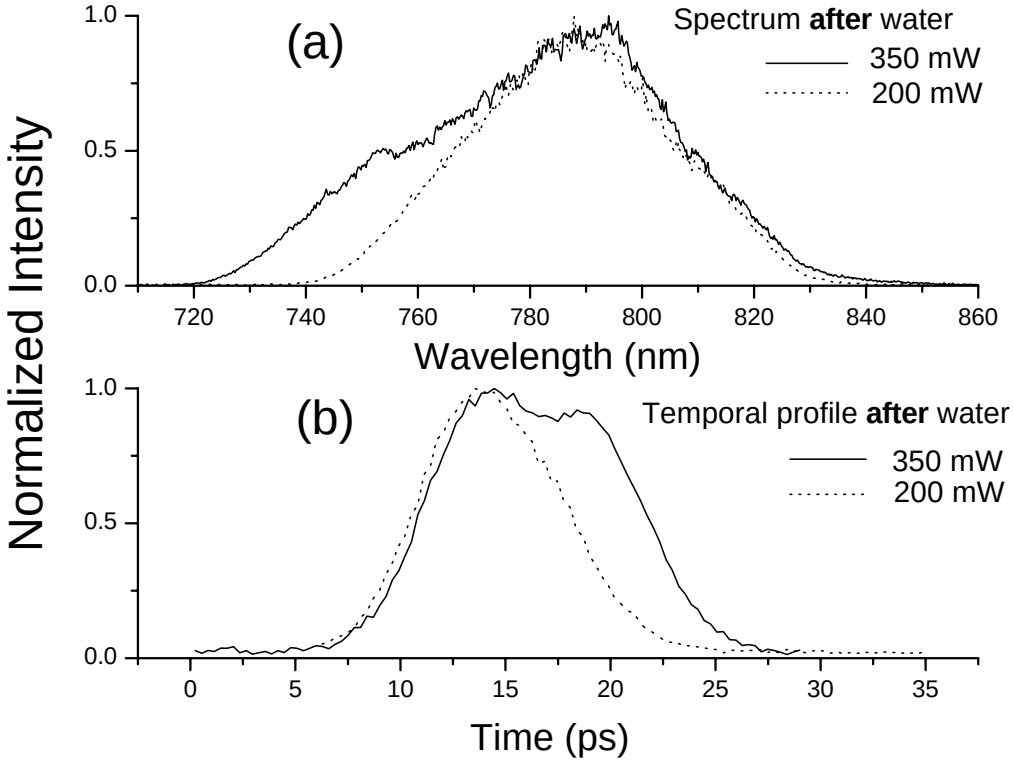

FIG. 5.11 Spectrum (a) and temporal profile (b) of the emerging pulse **after** going through 1.2 m of water. The dotted curve and solid curve represent a laser input power of 200 mW and 350 mW, respectively. The time axis is relative time.

Our analysis and experimental results shows that pulse split in water is due to distortion from small overtone absorption on the pulse profile, a process different as the formation of precursor (see section 5.3). No perceptible asympototic behavior exists around zero frequency for a 100fs pulse centered around 780 nm going through water. Optical precursors are not observed in water as claimed by Choi and Osterberg. The non-exponential decay of intensity, another 'obvious' evidence of observation of optical precursors, may be explained as the coherent effects between light and water. The coherent effect states that when the time integral of the pulse amplitude expressed in

suitable reduced units is equal to $2n\pi$, the pulse propagates unattenuated as a result of the coherent and nonlinear interaction with the absorbing medium [30, 31, 32, 33, 34].

5.4 Conclusion and discussion

In this chapter, we have discussed the formation of Brillouin precursor. For a Gaussian-sine incident pulse, reshaping by the absorption difference at the carrier frequency and the near zero frequency is the main mechanism of the formation of Brillouin precursor. We showed that the generation of a Brillouin precursor require the existence of significant zero or near zero frequency component. We believe that Brillouin precursor in water have not been observed by recent researchers. Our alternate explanation is that pulse breakup is due to vibrational overtone absorption and dispersion in water.

The discussion in this chapter focused on the carrier frequency below the resonant frequency. There are other cases, for the frequencies inside the absorption band. Reshaping from absorption, gain and dispersive propagation in this regime gave rise to interesting discussions of slow- and fast-light [28,29]. For frequency above the resonant frequency, it is sommerfeld precursor. We will be expected to study these effects in the future using THz pulses.

References:

1. L. Brillouin, *Wave propagation and group velocity* (Academic, New York, 1960).
2. A. Sommerfeld, Ann. Phys. (Leipzig) **44**, 177 (1914).
3. L. Brillouin, Ann. Phys. (Leipzig) **44**,203 (1914).
4. H. G. Baewald, Ann. Phys. (Leipzig) **7**, 731(1930).
5. J. L. Birman and M. J. Frankel, Opt. Commun. **13**, 303 (1975).
6. M. J. Frankel and J. L. Birman, Phys. Rev. A **15**, 2000 (1977).
7. T. A. Weber and D. B. Trizna, Phys. Rev. **144**, 277 (1966).
8. D. L. Johnson, Phys. Rev. Lett. **41**, 417 (1978).
9. E. Varoquaux, G. A. Williams, and O. Avenel, Phys. Rev. B **34**,7617 (1986).
10. P. Pleshko and I. Palócz, Phys. Rev. Let. **22**, 1201 (1969).
11. S. -H. Choi and U. Österberg, Phys. Rev. Lett. **92**, 193903 (2004) ; Also see, S. Chasteen, "Light wave outlasts itself", Phys. Rev. focus, **13** (12 May 2004); J. R. Minkel, "Splinters of light", Science News (20 May 2004); T. M. Roberts, Phys. Rev. Lett. **93**, 269401 (2004); R. R. Alfano, J. L. Birman, X. Ni, M. Alrubaiee, and B. B. Das, Phys. Rev. Lett. **94**, 239401 (2005).
12. J. D. Jackson, *Classical Electrodynamics* 2nd ed. (Wiley, New York, 1975).
13. K. E. Oughstun, and J. E. K. Laurens, Radio Science **26**, 245 (1991).
14. U. J. Gibson, and U. L. Österberg, Opt. Express **13**, 2105 (2005).
15. R. R. Alfano, Interaction of picosecond laser pulses with matter (Ph.D. dissertation, GTE Laboratories, Bayside, New Yok); R. R. Alfano, J. I. Gersten, G. A. Zawadzkas, and N. Tzoar, Phys. Rev. A **10**, 698 (1974).
16. K. E. Oughstun, Proc. IEEE **79**, 1379 (1991).

17. A. Karlsson and S. Rikte, J. Opt. Soc. Am. A **15**, 487 (1998).

18. N. C. Nielsen, S. Linden, J. Kuhl, J. Förstner, A. Knorr, S. W. Koch, and H. Giessen, Phys. Rev. B **64**, 245202 (2001).

19. J. Aaviksoo, J. Kuhl, and K. Ploog, Phys. Rev. A **44**, R5353 (1991).

20. M. Sakai, R. Nakahara, J. Kawase, H. Kunugita, and K. Ema, Phys. Rev. B **66**, 033302 (2002).

21. D. Grischkowsky, S. Keiding, M. van Exter, and Ch. Fattinger, J. Opt. Soc. Am. B **7**, 2006 (1990).

22. X. -C. Zhang, B. B. Hu, J. T. Darrow and D. H. Auston, Appl. Phys. Lett. **56**, 1011 (1990).

23. M. van Exter, C. Fattinger, and D. Grischkowsky, Appl. Phys. Lett. **55**, 337 (1989).

24. Q. Wu and X.-C Zhang, Appl. Phys. Lett. **70**, 1784 (1997).

25. H. J. bakker, G. C. Cho, H. Kurz, Q. Wu, and X.-C. Zhang, J. Opt. Soc. Am. B **15**, 1795 (1998).

26. A. Nahata, A. S. Weling, and T. F. Heinz, Appl. Phys. Lett. **69**, 2321 (1996).

27. T. Hattori, Y. Homma, A. Mitsuishi, and M. Tacke, Opt. Commun. **7**, 229 (1973).

28. S. Chu and S. Wong, Phys. Rev. Lett. **48**, 738 (1982); Also see comment: A. Katz and R. R. Alfano, Phys. Rev. Lett. **49**, 1292 (1982); and reply: S. Chu and S. Wong, Phys. Rev. Lett. **49**, 1293 (1982).

29. R. Y. Chiao, Phys. Rev. A **48**, R34 (1993).

30. S. L. McCall and E. L. Hahn, Phys. Rev. **183**, 457 (1969).

31. M. D. Crisp, Phys. Rev. A **1**, 1604 (1970).

32. M. D. Crisp, Phys. Rev. A **5**, 1365 (1972).

33. F. A. Hopf, G. L. Lamb, C. K. Rhodes, and M. O. Scully, Phys. Rev. A **3**, 758 (1971).

34. O. Avenel, E. Varoquaux, and G. A. Williams, Phys. Rev. Lett. **53**, 2058 (1984).

Chapter 6

Diffraction effects induced nonlinear effect for ultrashort pulse propagation through condensed media

6.1 Introduction

Nonlinear effect in isotropic condensed matter is governed by the n_2 term in the wave propagation equation and can be described by nonlinear wave equation. Self-focusing is a consequence of the competition between diffraction of beam and n_2. The self-focusing of ultrashort laser pulses in condensed media can give rise to filamentation. One of the most incredible effects in nonlinear optics is the supercontinuum(SC) generation[1,1,3]. In this phenomenon the spectral content of the pulse is dramatically broadened. Various nonlinear processes are responsible for collinear and conical continuum emission, mainly self-phase modulation (SPM) and nondegenerate four-wave mixing (FWM)[1,1], respectively. The threshold for SC generation is typically several megawatts for a range of transparent condensed media. At pulse powers well above the threshold (~100MW) the beam is observed to form multiple self-focused white-light filaments. These filaments increase the local intensity which in turn helps the intensity dependent SPM process.

For over thirty years, SC generation was used for time-resolved pump-probe research to study the dynamics of fundamental excitations in matter[4,5]. Recently, SC has attracted increasing interest for many diverse applications such as sources for wavelength division multiplexing in communications[6], long distance propagation[7], remote sensing[8,9,10], and femtosecond and attosecond pulse generation[11] among others. The

coherence of the SC has been demonstrated by Zeylikovich and Alfano using gratings for optical communications[12], by Cook *et. al*.[13] using a cylindrical lens to focus a beam to water, by Chin *et. al.*[14] through the observation of ring fringes came from the superposition of the background field and the fields that diverge from the filament as well as others [15].

Most recently, the ultrashort light filaments is been observed to survive their interaction with water droplets as large as 95 μm and that they can transmit through water clouds with little attenuation. [16].

Motivated by many applications, recent research has aimed to control the filamentation process and their distribution. The propagation distance at which filamentation occurs can be controlled by adding negative chirp to the pulse[17]. Méchain *et al*. achieved a degree of control by introducing field gradients and phase changes on the input beam in air [18], Schroeder et al performed similar investigations for controlling filaments in water [19]. Cook et al generated coherent array of WLC filaments produced by diffractive microlenses[20]. Other methods for filament control have utilized the effects of beam astigmatism and ellipticity [21,22].

In this chapter, periodic filamentation and SC generation were induced by Fresnel diffraction in BK7 glass from a circular aperture or a straight edge. The SC generation and filaments formation were observed at different distances from the apertures. Interferences patterns in SC spatial intensity distribution for both cases have been observed and attributed to the spatial arrangement of small-scale filaments. The experimental results showed that the spatial coherence among multiple filaments is high.

6.2. Theoretical description of light propagation in nonlinear media

Self-focusing

A simple physical model for self-trapping of optical beam is shown in Fig.6.1

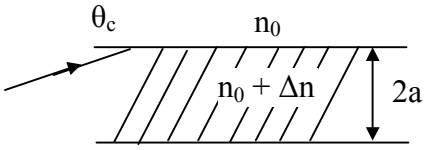

Fig.6.1 Propagation of light in $\chi^{(3)}$ media

where $\Delta n = n_2 |E|^2 = \dfrac{2\pi\chi^{(3)}|E|^2}{n_0}$ is the intensity-dependent refractive index which results to the self-focusing of the beam and n_0 is the linear index of the medium For $\theta \le \theta_c$, total reflection happens.

$$\cos(\theta_c) = n/n + \Delta n \tag{6.1}$$

and, since θ_c is small, $\cos\theta_c \approx 1 - \theta_c^2/2 = 1 - \Delta n/n$, $\theta_c = \sqrt{\dfrac{2\Delta n}{n}}$

If the beam diameter is 2a, the beam might be expected to expand by diffraction with an angular divergence of $\theta_D \approx 1.22\lambda/2n_0 a$.

The balance between self-focusing and diffraction ($\theta_c = \theta_D$) results to the self-trapping of beam. The critical power for self-trapping can be written

$$P_{cr} = I(\pi a^2) = \frac{n_0 c E^2}{8\pi}(\pi a^2) = \frac{c(1.22\lambda)^2}{64 n_2} \tag{6.2}$$

A more accurate description of the competition of self-focusing and diffraction can be obtained from wave propagation equation [23,24]. The power well above the critical power for self-trapping leads to the input beam fragments into random distribution of small-scale filaments [25] and supercontinuum generation.

Supercontinuum generation

For our discussion of self-phase modulation, let us start from the nonlinear wave equation:

$$\frac{\partial^2}{\partial z^2}E(z,t)-\frac{1}{c^2}\frac{\partial^2}{\partial t^2}\bar{E}(z,t)=\frac{4\pi}{c^2}\frac{\partial^2}{\partial t^2}\bar{P}(z,t) \tag{6.3}$$

where $\bar{P}=\bar{P}^{(1)}+\bar{P}^{(2)}=\chi^{(1)}E+\chi^{(3)}|E|^2E$, the wave equation can written as:

$$\frac{\partial^2}{\partial z^2}E(z,t)-\frac{n_0^2}{c^2}\frac{\partial^2}{\partial t^2}\bar{E}(z,t)=\frac{4\pi}{c^2}\frac{\partial^2}{\partial t^2}\bar{P}^{(3)}(z,t) \tag{6.4}$$

Let $E=A(z,t)\exp(ik_0z-i\omega_0t)$ and use the slowly varying amplitude approximation by neglecting the $\partial^2A/\partial t^2$ term, we got:

$$\left(\frac{\partial}{\partial z}+\frac{1}{\upsilon_g}\frac{\partial}{\partial t}\right)A(z,t)=-\frac{2\pi\omega_0^2}{ik_0c^2}\chi^{(3)}|A|^2A \tag{6.5}$$

Let $A(z,t)=A_0(z,t)\exp(i\phi)$ and $z'=z,t'=t-z/v_g$, we obtain for the above equation:

$$\frac{\partial A_0}{\partial z'}=0 \tag{6.6}$$

$$\frac{\partial\phi}{\partial z'}=\frac{2\pi\omega_0^2}{c^2k_0}\chi^{(3)}|A_0|^2 \tag{6.7}$$

They yield immediately the solution

$$\phi(z,t')=\phi_0+\frac{2\pi\omega_0^2}{c^2k_0}\chi^{(3)}|A_0(t')|^2z \tag{6.8}$$

A(z,t) can be written as:

$$A(z,t')=A(0,t')\exp\left(i\frac{2\pi\omega_0^2}{c^2k_0}\chi^{(3)}|A(0,t')|^2z\right)=A(0,t')\exp\left(in_2|A(0,t')|^2z\,\omega_0/c\right) \tag{6.9}$$

This is a pulse whose intensity is unaltered during propagation and which experiences a phase shift ϕ due to self-phase modulation

$$\phi = (\omega_0 / c) n_2 |A|^2 z \tag{6.10}$$

$|A|^2$ is a function of t', the various part of the pulse undergo different phase shifts, leading to a frequency shift or 'chirp' which is directly proportional to the distance traveled. Suppose, for example, the field $A(z,t)$ is initially in the form of a chirp-free (constant-phase) pulse $A(0,t)=E_0\mathrm{sech}(t/\tau)$. After such a pulse has traveled a distance z in the medium, the difference between its instantaneous optical frequency (at $t+z/v_g$) and carrier frequency ω_0 is obtained by differentiating the phase shift with respect to t:

$$\delta\omega = -\frac{d\phi}{dt} = -(\omega_0 / c) n_2 |E_0|^2 z \frac{d \sec h^2(t/\tau)}{dt} \tag{6.11}$$

$$\delta\omega(t) = 2 n_2 z (\omega_0 / c\tau) I_0 \sec h^2(t/\tau) \tanh(t/\tau) \tag{6.12}$$

The spectrum of the self-phase modulation field is, therefore, expected to be broaden. The further the pulse travels, the more modulation occurs. When SPM is very strong, it broadens the spectrum a lot, we call this effect continuum generation. The spectrum can be calculated from the Fourier transform

$$E(\omega) = \frac{1}{2\pi}\int_{-\infty}^{+\infty} E(z,t')\exp(i\omega t')dt' = \frac{1}{2\pi}\exp(i n_0 \omega z/c)\int_{-\infty}^{+\infty} A(0,t')\exp\left(i\left[(\omega-\omega_0)t + \omega_0 z n_2 |A(0,z')|^2 / c\right]\right) \tag{6.13}$$

which can be approximately evaluated by the method of stationary phase [26]

Fresnel Diffraction

Diffraction and interference[27] are two important effects taking place in optics and optical_phenomena to control the phase of waves. Both processes can rearrange the

spatial distribution of the incident energy and make it possible to alter nonlinear processes at sample site such as SC generation at a lower incident energy [28,29]and even help with the generation of ultrashort pulses. Fresnel diffraction describes the near field diffraction pattern and more intensity can occur spatially at well define distances for a light beam from a small aperture than for a full beam non-aperture case. The interference pattern at sample site from Fresnel diffraction for circular aperture gives a well define annular ring pattern[27]. The effects of Fresnel diffraction in the design of high-power laser systems has been studied by Campillo, *et. al*. [30] and Fleck, *et. al*.[31]. A period breakup of optical beams due to self-focusing has been reported and explained using an instability theory[32].

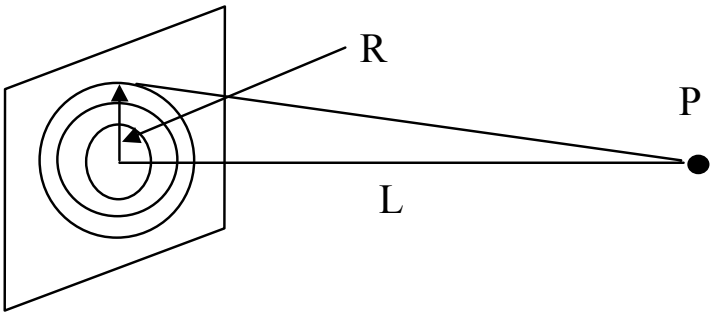

Fig. 6.2 Collimated beam illuminates the aperture

Considering a collimated beam propagation through an aperture (Fig. 6.2), the most important parameter needed for classifying near field diffraction pattern is the Fresnel number N, which denotes the number of zones seen by the observation point in the aperture. For an incident beam of uniform intensity, it is given by:

$$N = \frac{R^2}{\lambda L} \tag{6.14}$$

where R is the radius of the aperture, λ is incident wavelength, L is the on axis distance between the observation point and aperture. Fresnel number $N \geq 1$ produces Fresnel

diffraction. The sum of the optical field disturbance on axis from odd-numbered Fresnel zones at P is:

$$E \approx \frac{|E_1|}{2} + \frac{|E_N|}{2} \tag{6.15}$$

where E_N is the contribution from the electric field intensity of the Nth Fresnel zone. An even-numbered Fresnel zones leads to field at P given by:

$$E \approx \frac{|E_1|}{2} - \frac{|E_N|}{2} \tag{6.16}$$

The near-axis intensity I at this point P corresponding to one Fresnel zone obtained from Equ. (6.15) is

$$I \approx 4I_0 \tag{6.17}$$

where I_0 is the unobstructed intensity. A large intensity enhancement happens at the observation point P corresponding to odd Fresnel zones. The first zone gives largest intensity [Equ.(6.17)] and can induce nonlinear optical effects.

6.3. Fresnel supercontinuum generation and interference formation

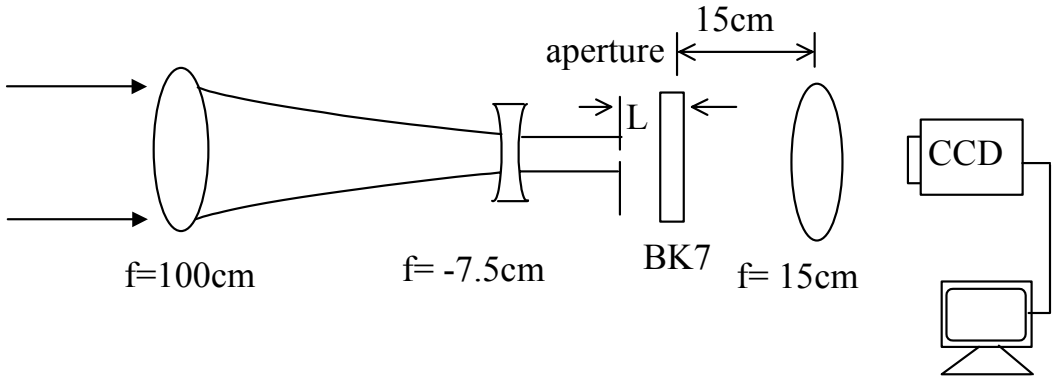

Fig. 6.3 Schematic diagram of the SC experimental setup

The experimental arrangement to observe the effect of Fresnel diffraction on SC generation is shown in Fig. 6.3. A Ti:sapphire amplifier system produces 0.35mJ,

160fs(FWHM) at 800nm pulses with a repetition rate of 1 KHz. The $1/e^2$ diameter of the beam is 1cm. Collimated beam propagates through an aperture of diameter 300μm. A BK7 glass with the thickness of 6mm is placed at a distance L from the aperture. A lens is used to collect the SPM and conical emission from the BK7. The intensity of incident beam is set below the threshold of self-focusing and SC generation in the BK7 without the aperture. The collecting lens and the BK7 is moved together towards the aperture along its axis at distances corresponding to N = 1,2,3…zones.

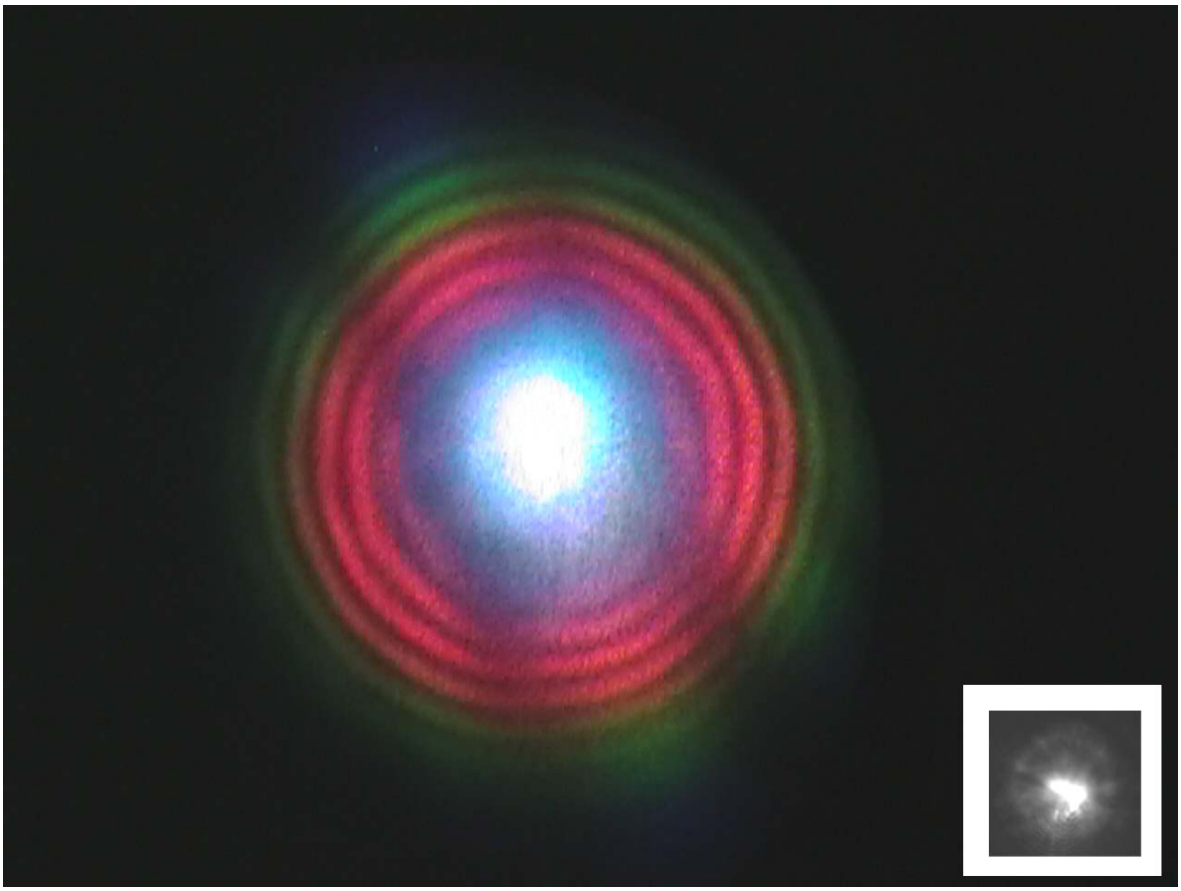

Fig. 6.4 Supercontinuum generation in BK7 glass resulting from energy enhancement of ultrashort beam propagation through a 300 μm diameter aperture at a distance corresponding to Fresnel number N = 1. The insert is the photograph of filaments formed in the BK7 glass. A central filament and some small scale filaments around the central one are showed in this photograph.

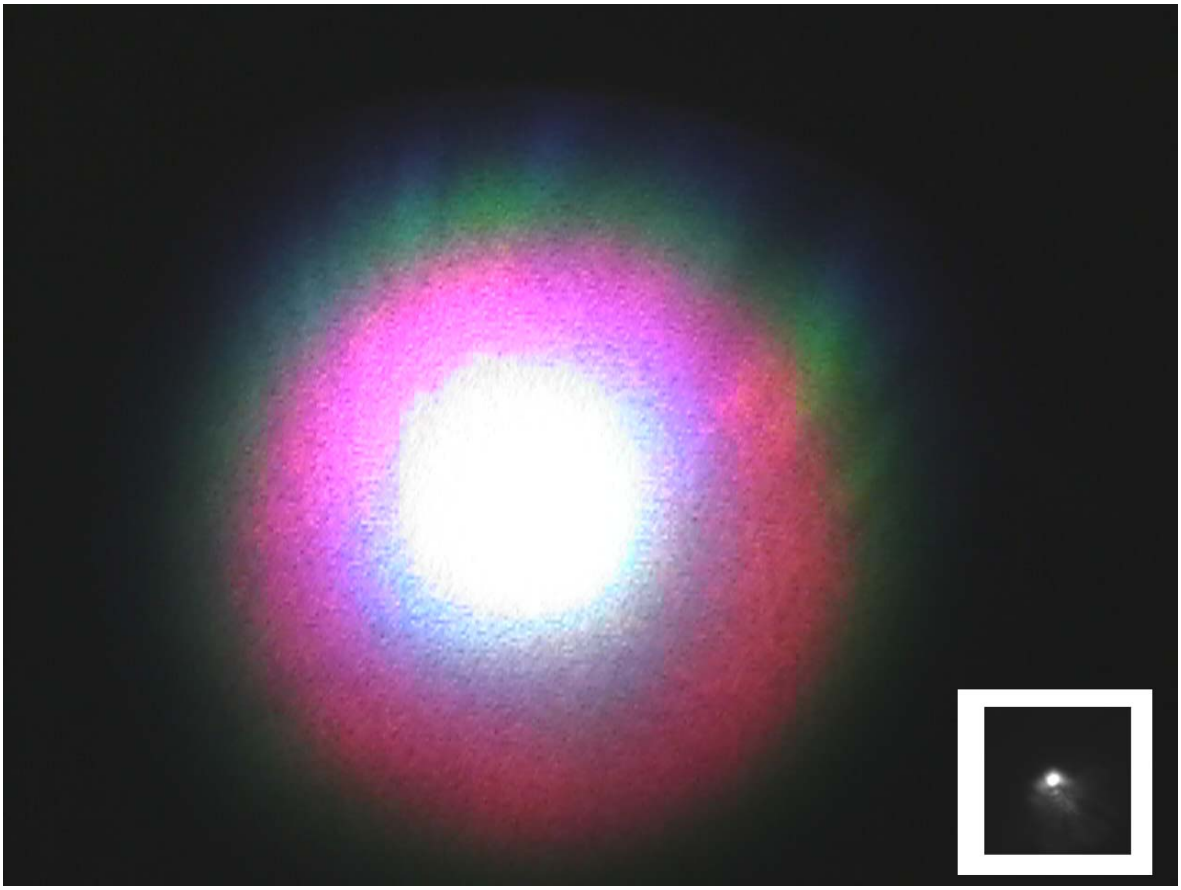

Fig. 6.5 Supercontinuum generation in BK7 glass resulting from energy enhancement of ultrashort beam propagation through a 300 μm diameter aperture at a distance corresponding to Fresnel number $N = 3$. The insert is the photograph of filaments in the BK7 glass. A central filament is only shown in this photograph.

The supercontinuum generation first appears when $N = 1$. A typical snapshot of the observed emission pattern is shown in Fig.6.4. The insert shows the filaments profile at the exit surface of the glass. SPM contributes to the white light spot in the central region[1]. The Nondegenerate four-photon stimulated emission[1] results in the colorful cone(red to violet). The blue portion near the central white light comes from the Rayleigh

scattering in BK7. According to Equ.(6.17) for $N = 1$, the intensity will 4 times higher than the unobstructed light intensity at the generation spot. The appearance of SC is consistent with the calculation of this radiation distribution.

When the collecting lens and the BK7 moved further towards the aperture, the SC generation will disappear and reappear again at the distance corresponding to $N = 3$, as expected from the radiation distribution along the axis. The observed SC pattern is shown in Fig.6.5, consisting of a colorful conical emission with white light in the central region.

6.4. Results and discussion

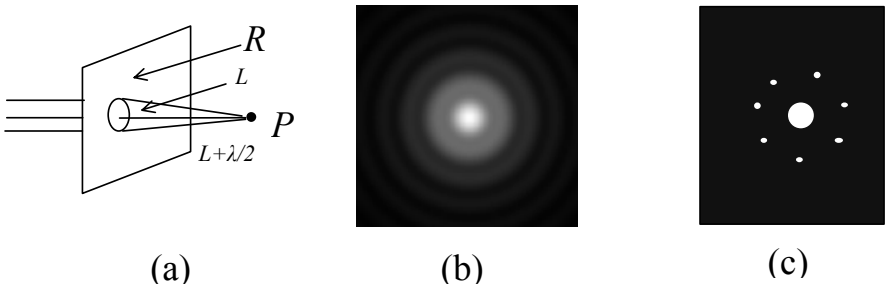

Fig. 6.6 Pictorial representation of Fresnel diffraction and filaments formation in BK7 glass located a distance corresponding to Fresnel number $N = 1$ to the aperture. a) Diagram of plane wave propagation through a aperture. b) Diffraction pattern of the incident laser in the sample (BK7). c) Filaments formation in the sample (BK7)

The difference between the emission pattern displayed in Figs.6.4 and 6.5 are the interference ring pattern inside the conical emission pattern. This is the first reported ring pattern arising from the interference of the Fresnel diffraction field inside the BK7 glass along the axis and along the first intense outer annular ring of diffraction pattern. Fig.6.6 is the pictorial representation explaining the Fresnel diffraction and filaments formation in BK7 located a distance corresponding to Fresnel number $N = 1$ in the aperture. Fig. 6.6(a) shows the diagram of beam propagation through the aperture. Fig. 6.6(b) shows the

diffraction intensity distribution from the first zone ($N = 1$) at the distance P. The pattern consists of central spot and annular rings. In Fig. 6.6(c), the central portion of the beam self focuses to form a bright filament, and the first intense diffracted annular ring at the sample site P also self focuses but breaks up to periodic small scale filaments[32]. The inserts in Figs. 6.4 and 6.5 show the filaments pattern photographed in the BK7 glass. Both photographs have a clear filament pattern generated by self-focusing in the central region which result in SC generation and FWM. At the position corresponding to $N = 1$, the intense outer ring of Fresnel diffraction self focuses and breaks up to several small scale filaments. Both the brighter filament in the central region and small small scale filaments in the annular ring can result in SC generation. Due to the intensity difference in the diffraction field of the central region and the outer first annular ring, the central filament and small scale filament from the annular ring are generated in different places in the BK7 glass. A small adjustment of the collecting lens position showed a change in the contrast of the central filament and small scale filaments around it, giving an estimation of 0.9 mm separation distance between the two set of filaments created. The SC generation at the two different positions along the beam propagation direction contributed to the interference ring observed on the CCD. Calculation based on the interference ring spacing confirmed the 0.9mm separation between the filament sources in the glass. Actually, this kind of ring can be observed for the supercontinuum generated around the focus point, where it has a similar intensity distribution as the diffraction field. In Fig.6.5 (N = 3), the outer ring of the diffraction field in the BK7 glass was not enough to form filaments in the annular ring. The SC generation is present in the central region and no interference rings occur in the angular FWM pattern.

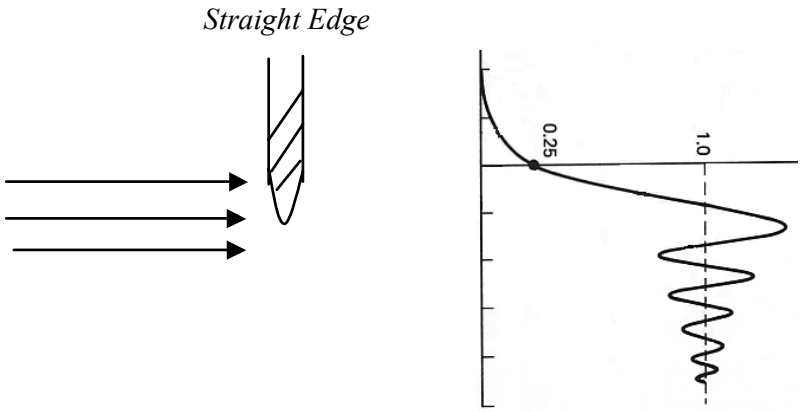

Fig.6.7 Diffracted intensity distribution from a straight edge illuminated by collimated light

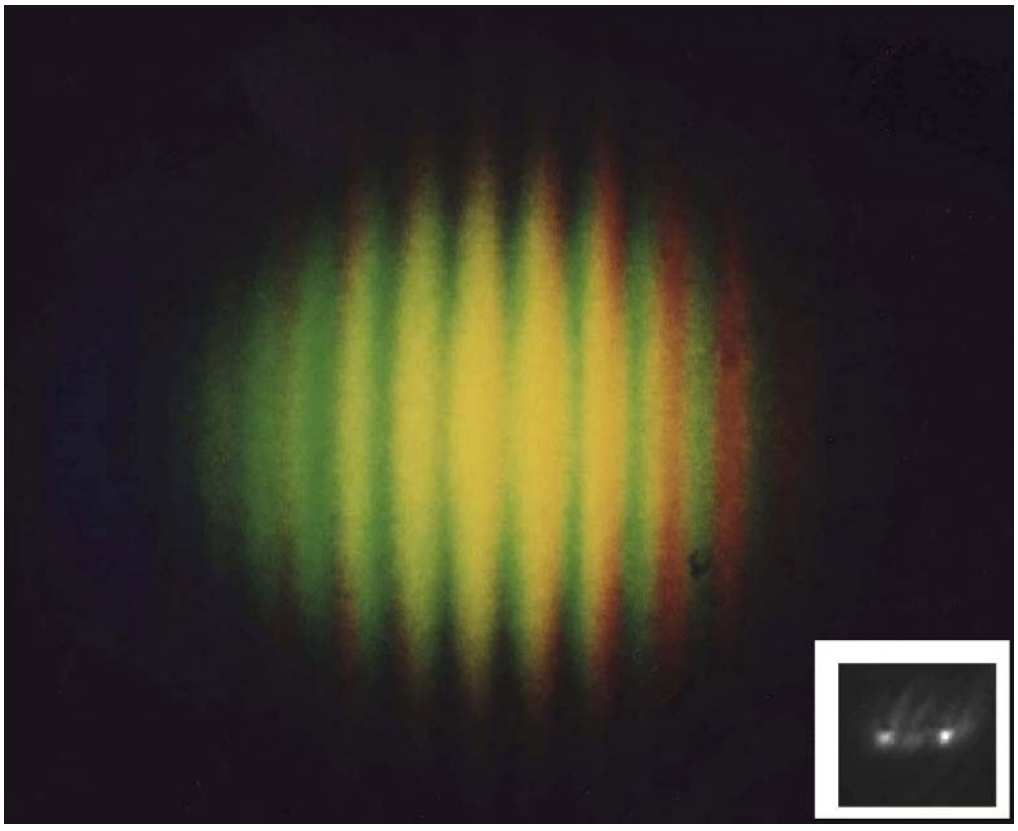

Fig. 6.8 Supercontinuum generation in BK7 glass resulting from energy enhancement of ultrashort beam propagation through a straight edge. The insert is the photograph of filaments in the BK7 glass. Two filament parallel to the edge are formed.

The intensity enhancement and SC generation can also occur from a diffraction straight edge. Fig.6.7 shows the diffracted intensity distribution from a straight edge illuminated by collimated light. The first Fresnel diffraction maximum from the edge is ~1.4 higher than the incident intensity[27]. Fig. 6.8 shows SC generation in BK7 glass when ultrashort intense laser propagating through a straight edge. In this case, the incident laser pulses were adjusted to be not strong enough to generate SC without an edge. This increase in intensity by diffraction from the straight edge creates SC with a lower power incident laser pulse. Fringes are observed in the SC emission perpendicular to the edge. This interference phenomenon can be understood from the fringes pattern in the diffracted intensity distribution in the BK7 glass. Self-focusing can be formed along the first maximum fringe which breaks up into small scale filaments along the edge direction. The spatial distribution of filaments inside the BK7 glass is photographed and presented in the insert of Fig. 6.8. Two filaments are formed parallel to the edge. These two filaments produce interference fringes pattern perpendicular to the edge. This interference pattern is similar to the pattern observed by Cook's[13] using a focusing cylindrical lens to produce a horizontal spatial array of filaments.

6.5. Conclusion

In summary, SC generation has been enhanced using Fresnel diffraction with a lower laser intensity from femtosecond laser pulses. Diffraction led to the formation of periodic filaments. Clear interference fringes and rings are observed. Those interference structures reveals that SC sources within different filaments formed by different complicated nonlinear processes are mutually coherent. Further experimental and theoretical work is

needed to describe the interference structures in the SC generation resulting from diffraction and types I, II, and III self-focusing[1,33].

References:

1. R. R. Alfano and S. L. Shapiro, Phys. Rev. Lett. **24**, 592 (1970).
2. R. R. Alfano and S. L. Shapiro, Phys. Rev. Lett. **24**, 584 (1970).
3. R. R. Alfano and S. L. Shapiro, Phys. Rev. Lett. **24**, 1217 (1970).
4. R. R. Alfano and S. L. Shapiro, Scientific American, **228**, no. 6, 42-55, 58, 60, (1973).
5. R. R. Alfano, *The Supercontinuum Laser Source* (New York: Springer-Verlag, 1989).
6. Y. Takushima and K. Kikuchi, IEEE Photon. Technol. Lett., **11**, 322 (1999).
7. A. Braun, G. Korn, X. Liu, D. Du, J. Squier, and G. Mourou, Opt. Lett. **20**, 73 (1995).
8. P. Rairoux, H. Schillinger, S. Niedermeier, M. Rodriguez, F. Ronneberger, R. Sauerbrey, B. Stein, D. Waite, C. Wedekind, H. Wille, and L. Wöste, and C. Ziener, Appl. Phys. B **71**, 573 (2000).
9. Q. Luo, W. Liu, and S. L. Chin, Appl. Phys. B **76**, 337 (2003).
10. G. Méchain, J. Kasparian, J. Yu, S. Frey, E. Salmon, and J-P. Wolf, Appl. Phys. B. 78, 535 (2004).
11. A. Baltuška, M. Uiberacker, E. Goulielmakis, R. Kienberger, V. S. Yakovlev, T. Udem, T. W. Hänsch, F. Krausz, IEEE JSTQE **9**, 972 (2003).
12. I. Zeylikovich and R. R. Alfano, Appl. Phys. B **77**, 265 (2003).
13. K. Cook, A. K. Kar, and R. A. Lamb, Appl. Phys. Lett. **83**, 3861 (2003).
14. S. L. Chin, S. Petit, W. Liu, A. Iwasaki, M. –C. Nadeau, V. P. Kandidov, O. G. Kosareva, K. Yu. Andrianov, Opt. Comm. **15**, 329 (2002).

15. W. Watanbe and K. Itoh, Jpn. J. Appl. Phys. **40**, 592 (2001).

16. F. Courvoisier, V. Boutou, J. asparian, E. Salmon, Appl. Phys. Lett. **83**, 213 (2003).

17. H. Wille, M. Rodriguez, J. Kasparian, D. Mondelain, J. Yu, A. Mysyrowicz, R. Sauerbrey, J-P. Wolf and L. Wöste, Eur. Phys. J. AP. **20**, 183 (2002).

18. G. Méchain, A. Couairon, M. Franco, B. Prade and A. Mysyrowicz, Phys. Rev. Lett. **93**, 035003 (2004).

19. H. Schroeder, J. Liu, and S. L. Chin, Opt. Express **12**, 4789 (2004).

20. K. Cook, R. McGeorge, A. K. Kar, M. R. Taghizadeh, and R. A. Lamb, Appl. Phys. Lett. **86**, 021105 (2005).

21. G. Fibich, S. Eisenmann, B. Ilan and A. Zigler, Optics Letters **29**, 1772 (2004).

22. A. D. Dubietis, G. Tamošauskas, G. Fibich and B. Ilan, Opt. Lett. **29**, 1126 (2004).

23. R. Y. Chiao, E. Garmire, and C. H. Townes, Phys. Rev. Lett. **13**, 479 (1964).

24. P. L. Kelley, Phys. Rev. Lett. **15**, 1005 (1965).

25. M. Centurion, Y. Pu, M. Tsang, and D. Psaltis, Phys. Rev. A **71**, 063811 (2005).

26. R. R. Alfano, "Interaction of picosecond laser pulses with matter", GTE Technical Report TR 72-330. Published as Ph.D. thesis at New York University (1972).

27. M. Born and E. Wolf, *Principles of Optics*, 6th ed. (Oxford: Pergamon Press, 1980).

28. K. Cook, A. K. Kar, and R. A. Lamb, Opt. Express **13**, 2025 (2005).

29. X. Ni, C. Wang, X. Liang, M. Alrubaiee and R. R. Alfano, IEEE *JSTQE* **10**, 1229 (2004).

30. A. J. Campillo, J. E. Pearson, S. L. Shapiro, and N. J. Terrell, Jr., Appl. Phys. Lett. **23**, 85 (1973).

31. J. A. Fleck, Jr. and C. Layne, Appl. Phys. Lett. **22**, 467 (1973).

32. A. J. Campillo, S. L. Shapiro, and B. R. Suydam, Appl. Phys. Lett. **23**, 628 (1973).

33. Y. R. Shen, *The principles of nonlinear optics* (Wiley, New York, 1984).

Chapter 7

Summary and future work

In this thesis, we have presented study of light scattering and transmission in turbid media. The polarization properties as well as media properties (particle sizes, concentration, *etc.*) of the scattered light is concerned. Some others properties of pulse scattering and transmission in turbid media deserve to be explored for the fundamental physics and application purposes. Here are several lines of research arising from this thesis work that have been planed to be pursued.

7.1 Interference and diffraction experiments for scattered light from random medium

Can we select out the ballistic or snake-like photons directly after light going through the turbid media. Since the ballistic and snake-like photon just exists in the parallel to the incident polarization component, interference is an effect, which maybe act as the mechanism to cut off the diffusive photons.

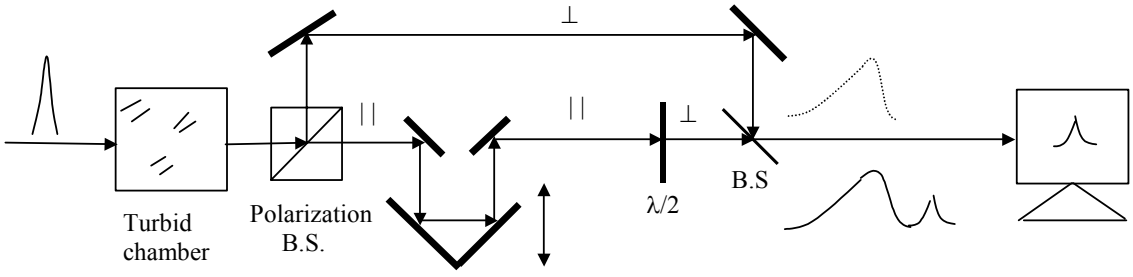

Fig. 7.1 Interference experiment to extract the ballistic and snake-like photon

Fig.7.1 presents our proposal experiment to get rid of diffusion photons and select out the ballistic and snake-like photons directly. We separate the transmitted light to parallel

and perpendicular to incident polarization components, change the parallel polarization to perpendicular polarization using a wave plate, add it with the perpendicular component emerging from the turbid media. A delay in the optical path of the parallel component is used to adjust the delay between the two arms. We predict that the diffusion photons in the parallel component can be cancelled by the perpendicular component emerging from the media. This technique is very different with the OCT technique, which needs a reference beam from the light source, which is impractical in some situation.

This suggested experiment raises the investigation of the coherent properties of the diffusion component. In many treatments of Young's interference experiments, a discussion of the nature of the light source is avoided. It is fortuitous, however, that regardless of the nature of the light source and its state of polarization, interference will always be observed.

Fresnel and Arago did Young's experiment [1] again using polarized light, their results can be summarized as following:

- Two waves linearly polarized in the same plane can interfere.
- Two waves linearly polarized with perpendicular polarizations cannot interfere.
- Two waves linearly polarized with perpendicular polarizations, if derived from perpendicular component of unpolarized light and subsequently brought into the same plane, cannot interfere.
- Two wave linearly polarized with perpendicular polarizations, if derived from the same linearly polarized wave and subsequently brought into the same plane, can interfere.

Point 3 in Fresnel and Arago's results can be understood as that the parallel and perpendicular polarization came from different process in the natural light emission, no phase relation exists for parallel polarization and perpendicualr polarization in the natural light. What will we do in this experiment is: if their assumption is the correct, I will not see the interference if we desinged an experiment as shown in Fig.7.2 for the natural unpolarized light source. where

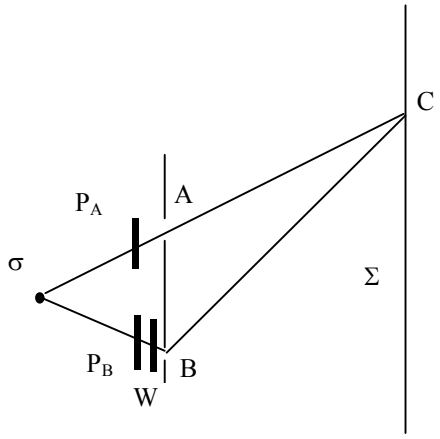

Fig. 7.2 Interference experiment with polarized light

σ is the light source, P_A and P_B is the parallel and perpendicular polarizer. W is a half-wave plate which change the polorization of the light after P_B to the same polarization as point A. Screen is used to observe the interference pattern from the double slits A and B. We haven't seen any report of the result of this suggested experiment for scattered light. The depolarization mechanisms for natural light source and scattered light are very different. For natural light source, the parallel and perpendicular light from independent emission process, however, the parallel and perpendicular scattered light is just rotation of polarization plane from the same polarized light source by the scatterers in the medium. Coherence property exists in the parallel and perpendicular component of the

scattered light from turbid media. If this experiment present a result of interference phenomena on the screen for the scattered light, it will indicate the possibility we can succeed in selecting the snake-like photon out directly, also, it will indicate a useful unpolarized source different as the natural unpolarized light. Furthermore, we are going to investigate the temporal interference properties of different component of the scattered light.

7.2 Passive signal propagation and imaging using optical trapping

The word “passive” came from the idea that, instead of propagating signal or imaging through a medium without altering the host medium properties, we proposed to improve the image contrast by redistributing the particles inside the host medium using optical trapping effect. A single-beam gradient force optical trap for Mie and Rayleigh dielectric particles was observed by Ashkin in 1986 [2]. A wide variety of optical traps based on the basic scattering and gradient forces of radiation pressure [3,4,5]. The scattering force is proportional to the optical intensity and points in the direction of the incident light. The gradient force is proportional to the gradient of the intensity and points in the direction of the intensity gradient. Since their development in the 1980s, they have remained limited for many years to trapping only one particle per laser beam. The most exciting developments in optical tweezers in recent years has been the creation of two-, three-and four-dimensional arrays of optical traps by using diffractive optical (DO) [7,8] and the generalized phase contrast (GPC) method [9,10]. Here, we proposed to trap the particles in the pathway of the signal beam with a guide doughnut beam. As we shown

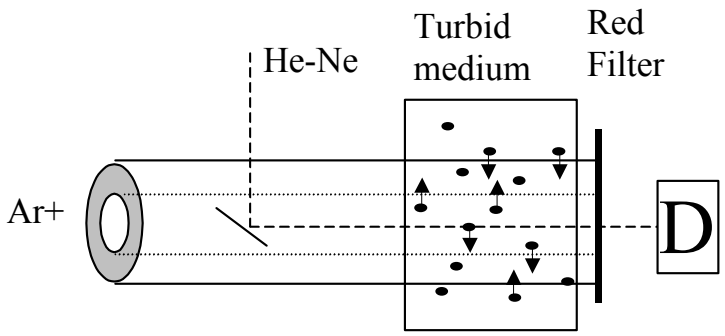

Fig. 7.3 Optical trapping for signal propagation and imaging experiment

in Fig. 7.3, a doughnut Ar^+ laser beam with Gaussian intensity distribution in the ring (such as a Laguerre-Gaussian laser mode) propagates through a turbid medium. A He-Ne laser Beam goes through the center of the Ar^+ beam. The Ar^+ laser is stronger in intensity and acts as the guide light to trap the particles in the hollow center to distribute along the ring. A weaker signal He-Ne laser will travel through the medium experiencing less scattering.

Mode converters, phase singularities as well as other techniques can be used to generate the doughnut beam [11,12,13,14,15]. Here, we expanded the Gaussian beam with TEM_{00} mode, blocked the central of the beam with a pin, and reduced the beam size. A doughnut beam is formed with a sharp inner edge of ring. A focus lens transformed the sharp edge ring to approximate Guassian intensity distribution at the near focus position. The sample is located around the near focus position.

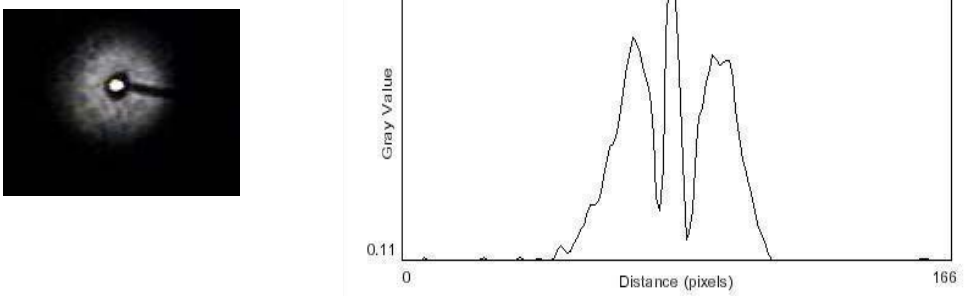

Fig.7.4 Doughnut beam (Ar^+ laser) with a signal beam located at the hollow center.

Fig. 7.4 shows the image and profile of the doughnut beam (Ar^+ laser) and the signal beam (He-Ne laser) at the sample position. The doughnut beam, which is much stronger and is attenuated for the visualization of signal beam, 'moves' away the particles along the pathway of the signal beam in the turbid medium. Fig.7.5 shows the concentration dependence of optical trapping. In Fig.7.5, the power of Ar^+ is 0.8W. ΔI is the intensity difference of the detected He-Ne light intensity with or without doughnut beam. X-axis is the concentration of the scatterers in the turbid medium. The diameter of scatterer is 4.18 μm. Fig. 7.5 shows a clear improvement of the signal intensity with the guided doughnut beam. The application of the optical trapping technique in the field of signal propagation and imaging in turbid medium is promising.

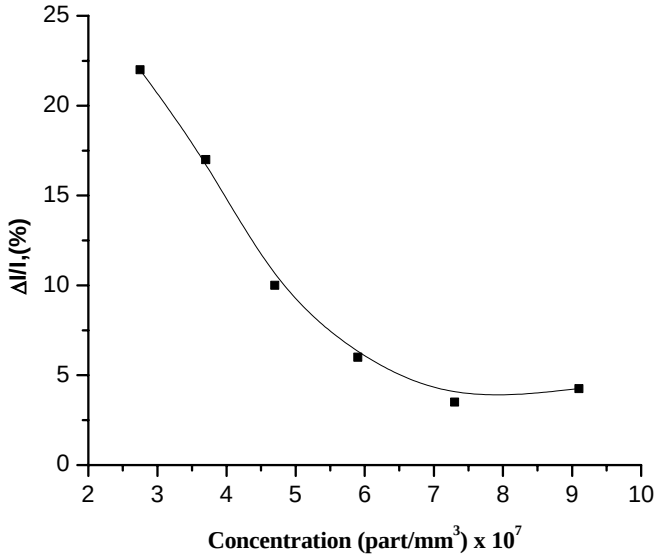

Fig. 7.5 Concentration dependence of optical trapping.

7.3 Signal detection and imaging with saturable absorber

A saturable absorber is an optical component with certain optical loss, which is reduced for high optical intensities. This effect can. occur in DODCI dye [16] as well as semiconductors[17,18].

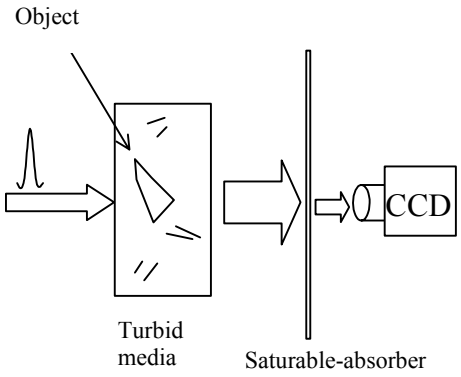

7.6 Image with saturable absorber

Saturable absorption effect may provide an efficient way to extract the ballistic photon from the background of diffusive scattered light. The ballistic light decays quickly in the turbid medium, however, the pulse width remain approximately the same as the incident pulse. For an ultrashort pulse, it means the peak power of the ballistic light is much higher than the diffusive light. Fig.7.6 is the proposed experimental setup. An appropriated selected fast saturable absorber before the CCD camera can be used to cut the diffusive light background and enhance the image contrast.

References:

1. C. Brosseau, *Fundamentals of polarized light: A statistical optics approach* (John Wiley & Sons, 1998).
2. A. Ashkin, J. M. Dziedzic, J. E. Bjorkholm, and S. Chu, Opt. Lett. **11**, 288 (1986).
3. A. Ashkin, Science **210**, 1081 (1980).
4. V. S. Letokhov and V. G. Minogin, Phys. Rep. **73**, 1 (1981).
5. A. Ashkin and J. P. Gordon, Opt. Lett. **8**, 511 (1983).
6. A. Ashkin and J. M. Dziedzic, Phys. Rev. Lett. **54**, 1245 (1985).
7. E. R. Dufresne, G. C. Spalding, M. T. Dearing, S. A. Sheets, D. G. Grier, Rev. Sci. Instrument. **72**, 1810 (2001).
8. J. Leach, G. Sinclair, P. Jordan, J. Courtial, M. J. Padgett, J. Cooper, and Z. J. Laczik, Opt. Express **12**, 220 (2004).
9. P. J. Rodrigo, R. L. Eriksen, V. R. Daria, and J. Glückstad, Opt. Express **10**, 1550 (2002).
10. P. J. Rodrigo, V. R. Daria, and J. Glückstad, Appl. Phys. Lett. **86**, 074103 (2005).
11. M. W. Beijersbergen, L. Allen, H. E. L. O van der Veen and J. P. Woerdman, Opt. Comm. **96**, 123 (1993).
12. N. R. Heckenberg, R. McDuff, C. P. Smith, and A. G. White, Opt. Lett. **17**, 221 (1992).
13. M. Padgett, J. Arlt, and Simpson, Am. J. Phys. **64**, 77 (1996).
14. O. Boyko, Th. A. Planchon, P. Mercère, C. Valentin and Ph. Balcou, Opt. Comm. **246**, 131 (2005).
15. J. Arlt, K. Dholakia, L. Allen and M. J. Padgett, J. Mod. Opt. **45**, 1231 (1998).

16. D. N. Dempster, T. Morrow, R. Ranken and G. F. Thompson, J. Chem. Soc. Faraday II **68**, 1479 (1972).

17. M. Haiml, R. Grange, U. Keller, Appl. Phys. B **79**, 331 (2004).

18. U. Keller, K. J. Weingarten, F. X. Kärtner, D. Kopf, B. Braun, I, D. Jung, R. Fluck, C. Hönninger, N. Matuschek and J. Aus der Au, IEEE *JSTQE* **2**, 435 (1996).

Appendix A

Analytical solution of the vector transport equation using cumulant expansion

In this appendix, we present analytical cumulant solution of the polarized radiative transfer equation in an infinite medium developed by W. Cai, expressed in the angular distribution **F**(**s**,t), the first cumulants (the center of the distribution), the second cumulant (half-width of spread of the distribution), and an approximation Gaussian polarized photon spatial distribution I(**r**,**s**,*t*) as function of position **r**, light direction **s**, and *t*. Detailed derivation of formula for cumulant solution of the polarized radiative transfer is given in Ref.1. Several minor modifications are made in this appendix.

As we showed in Chapter 2, the polarized photon transport equation is described as:

$$\partial I^{SP}(r,s,t)/\partial t + cs\cdot\nabla_r I^{SP}(r,s,t) + \mu_a I^{SP}(r,s,t) = \mu_s \int P(s,s')\left[I^{SP}(r,s',t) - I^{SP}(r,s,t)\right]ds' + I^{SP(0)}\delta(r-r_0)\delta(s-s_0)\delta(t-0) \quad \text{(A.1)}$$

We analytically solve Equ.(A.1). First, we study the dynamics of the photon distribution in the light direction space in circular presentation (CP), **F**(**s**, $\mathbf{s}_0$, t), which is a vector of four components on a spherical surface for **s** of radius 1. The kinetic equation of **F**(**s**,$\mathbf{s}_0$,t) can be obtained by integrating Equ.(2.1) over whole space **r**. The integral of the gradient term over all space vanishes. The spatial independence of μ_s, μ_a, and **P**(**s**,**s**') retains translation invariance. Thus the integral of Equ.(2.1) obeys:

$$\partial \mathbf{F}(\mathbf{s},\mathbf{s}_0,t)/\partial t + \mu_a \mathbf{F}(\mathbf{s},\mathbf{s}_0,t) + \mu_S[\mathbf{F}(\mathbf{s},\mathbf{s}_0,t) - \int \mathbf{P}(\mathbf{s},\mathbf{s}')[\mathbf{F}(\mathbf{s}',\mathbf{s}_0,t)ds'] = \mathbf{I}^{(0)}\delta(\mathbf{s}-\mathbf{s}_0)\delta(t-0) \quad \text{(A.2)}$$

where the angular distribution **F**(**s**,$\mathbf{s}_0$,t) is defined by

$$\mathbf{F}(\mathbf{s},\mathbf{s_0},t) = \int d\mathbf{r}\mathbf{I}(\mathbf{r},\mathbf{s},t) \tag{A.3}$$

The mth component of $\mathbf{F}(s,s_0,t)$, with the initial polarization in unit n_0 state, can be expanded in GSF's in the following form:

$$F^{CP}_{mn_0}(s,s_0,t) = \sum_l F^l_{mn_0}(t) \sum_s (-1)^s P^l_{m,s}(\mu) P^l_{s,n_0}(\mu_0) \exp[-is(\phi-\phi_0)] \exp(-\mu_a t) \tag{A.4}$$

When $\mathbf{s}_0$ is set along $\mathbf{z}$ direction and the initial reference plane is set as *x-o-z* plane, and $\mathbf{s} = (\theta,\phi)$, Equ.(A.4) is specialized to the following form:

$$F^{CP}_{mn_0}(s,z,t) = \sum_l \left[F^l_{mn_0}(t) P^l_{m,n_0}(\cos\theta) - \delta_{m,n_0} \frac{2l+1}{4\pi} e^{-\mu_s t} P^l_{0,0}(\cos\theta) \right] \times \exp(-in_0\phi) \exp(-\mu_a t) \tag{A.5}$$

The second term in Equ.(A.5) being substracted represents the ballistic (unscattered) photons. The detailed reasons for this subtraction is explained in Ref.2. The corresponding subtracted terms in calculation of the first cumulant and the second cumulant will appear in the later section.

Using the addition theorem of GSF [3], one can eliminate the variables χ', χ, Θ in Equ. (2.3), and express the components of the phase matrix in Equ.(A.2) in fixed coordinates as:

$$P_{mn}(\mu,\phi;\mu',\phi') = \frac{1}{4\pi} \sum_l p^l_{mn} \sum_{s=-l}^{l} (-1)^s P^l_{m,s}(\mu) P^l_{s,n}(\mu') \exp[-is(\phi-\phi')] \tag{A.6}$$

Substituting Equ. (A.5) and (A.6) to Equ.(A.2) and using the orthogonality relation of GSF's, an analytically solvable equation for $F^l_{mn_0}(t)$ for each *l* is obtained:

$$dF^l_{mn_0}(t)/dt = \sum_n \Pi^l_{mn} F^l_{nn_0}(t) \tag{A.7}$$

with $\Pi^l_{mn} = \mu_s\left[\delta_{m,n} - p^l_{m,n}/(2l+1)\right]$ (the coefficiet p^l_{mn} is defined on Section 2.2), under the initial condition

$$F^l_{mn_0}(t=0) = \delta_{m,n_0}(2l+1)/4\pi \tag{A.8}$$

Note that m, n_0 must be 0 or –0 for l=0,1. The solution $F^l_{mn_0}(t)$ has the following form:

$$F^l_{mn_0}(t) = \frac{2l+1}{4\pi}\sum_i \left[B^l_{mn_0}\right]_i \exp\left(-\lambda^l_i t\right) \tag{A.9}$$

i = 1,2,3,4 for l≥2, and i = 1,2 for l = 1,2. The eigenvalues λ^l_i for $l \geq 2$ is given by

$$\lambda^l_i = (1/2)\left\{\left(\Pi^l_{00} + \Pi^l_{22} \pm \Pi^l_{0-0} \pm \Pi^l_{2-2}\right) + \left[\left(\Pi^l_{00} - \Pi^l_{22} \pm \Pi^l_{0-0} \mp \Pi^l_{2-2}\right)^2 \pm 16\begin{pmatrix}\mathrm{Re}\left[\Pi^l_{20}\right] \\ \mathrm{Im}\left[\Pi^l_{20}\right]\end{pmatrix}^2\right]^{1/2}\right\} \tag{A.10}$$

for I = 1, 2, and for I = 3, 4, the sign '+' before the square brackets in Equ.(A.10) is replaced by '-'. For l=0,1 two eigenvalues are $\lambda^l_i = \Pi^l_{00} \pm \Pi^l_{0-0}$. The constant coefficients $\left[B^l_{mn_0}\right]_i$ can be determined using linear algebra under the initial condition Equ.(A.8).

In SP the mth component m = [I, Q, U, V] of the angular distribution, with the initial polarized state $\boldsymbol{I}^{\mathrm{SP}(0)}$, is obtained by

$$F^{SP}_m(s,t) = \left[T^{-1}F^{CP}(s,t)TI^{SP(0)}\right]_m \tag{A.11}$$

The angular distribution for the parallel polarized component is given by

$$F_{\parallel}(s,t) = \left[F^{SP}_I(s,t) + F^{SP}_Q(s,t)\right]/2 \tag{A.12a}$$

. Similarly, we have

$$F_{\perp}(s,t) = \left[F^{SP}_I(s,t) - F^{SP}_Q(s,t)\right]/2 \tag{A.12b}$$

$$F_R(s,t) = \left[F^{SP}_I(s,t) + F^{SP}_V(s,t)\right]/2 \tag{A.12c}$$

$$F_L(s,t) = \left[F^{SP}_I(s,t) - F^{SP}_V(s,t)\right]/2 \tag{A.12d}$$

Equ. (A.11) serves as the exact Green's function of polarized light propagation in the light direction space. It determines all time evolution of polarized light, including its spatial distribution, because displacement is an integration of velocity, c**s**(t), over time. The *m*th component [*m=I,Q,U,V*] of the photon distribution function in the SP representation, $I_m^{SP}(r,s,t)$, with the source located at $\mathbf{r}_0 = 0$, the initial direction $\mathbf{s}_0$, and the initial polarization $\mathbf{I}^{SP(0)}$, is given by

$$I_m^{sp}(r,s,t) = \left\langle \delta\left(r - c\int_0^t s(t')dt'\right)\delta(s(t)-s)\right\rangle_m^{SP} \tag{A.13}$$

where $\langle\cdots\rangle_m^{SP}$ means the *m*th component of the ensemble average in the light direction space in the SP representation. The first δ function ensures that the displacement **r**-0 is given by a path integral. The second δ function assures the correct final value of the direction. Equ.(A.13) is a formally exact solution, but cannot be evaluated directly. We make a Fourier transform for the first δ function in Equ.(A.13), and obtain

$$I_m^{SP}(\mathrm{r},\mathrm{s},t) = F_m^{SP}(\mathrm{s},\mathrm{s}_0,t)\frac{1}{(2\pi)^3}\int d\mathrm{q}\exp\left\{i\mathrm{q}\cdot\mathrm{r} + \sum_{k=1}^{\infty}\frac{(-ic)^k}{k!}\sum_{j_k}\cdots\sum_{j_1} q_{j_k}\cdots q_{j_1}\right.$$

$$\left.[< \int_0^t dt_k \cdots \int_0^t dt_1 T[s_{j_k}(t_k)\cdots s_{j_1}(t_1)] >_c]_m^{SP}\right\} \tag{A.14}$$

where T denotes time-ordered multiplication [4,5]. The index c denotes a cumulant, which is defined in statistics books[6,7]. As for an arbitrary random variable A, we have

$$\langle A\rangle_c = \langle A\rangle, \quad \langle A^2\rangle_c = \langle A^2\rangle - \langle A\rangle\langle A\rangle \tag{A.15}$$

The *k*th moment can be evaluated using a standard time-dependent Green's function approach, which is given by

$$[<\int_0^t dt_k \cdots \int_0^t dt_1 T[s_{j_k}(t_k)\cdots s_{j_1}(t_1)]>]_m^{SP} = \frac{1}{F_m^{sp}(\mathrm{s},\mathrm{s}_0,t)} \left\{ \int_0^t dt_k \int_0^{t_k} dt_{k-1} \cdots \int_0^{t_2} dt_1 \right.$$
$$\int d\mathrm{s}^{(k)} \int d\mathrm{s}^{(k-1)} \cdots \int d\mathrm{s}^{(1)} \mathrm{F}^{SP}(\mathrm{s},\mathrm{s}^{(k)},t-t_k) s_{j_k}^{(k)} \mathrm{F}^{SP}(\mathrm{s}^{(k)},\mathrm{s}^{(k-1)},t_k-t_{k-1}) s_{j_{k-1}}^{(k-1)} \cdots \quad \text{(A.16)}$$
$$\left. \mathrm{F}^{SP}(\mathrm{s}^{(2)},\mathrm{s}^{(1)},t_2-t_1) s_{j_1}^{(1)} \mathrm{F}^{SP}(\mathrm{s}^{(1)},\mathrm{s}_0,t_1-0) \mathrm{I}^{SP(0)}]_m + \text{perm.} \right\}$$

where the abbreviation "perm" means all k!-1 terms obtained by permutation of $\{j_i\}$, i=1,…k, from the first term.

In the evaluation of Equ.(A.16), it is convenient to set s in a spherical harmonic basis

$$s = [s_1, s_0, s_{-1}] = [-2^{-1/2}\sin\theta e^{+i\phi}, \cos\theta, +2^{-1/2}\sin\theta e^{-i\phi}] \quad \text{(A.17)}$$

which is related to a component in Cartesian basis α = x, y, z by $s_\alpha = \sum U_{\alpha j} s_j$, j = 1, 0, -1 with

$$U = \begin{bmatrix} -2^{-1/2} & 0 & 2^{-1/2} \\ 2^{-1/2} i & 0 & -2^{-1/2} i \\ 0 & 1 & 0 \end{bmatrix} \quad \text{(A.18)}$$

Also, here we introduce a recurrence relation of GSP's to evaluate Equ.(A.16). This recurrence relation is directly derived from angular momentum theory [8]. Defining $s_j = \mu_j e^{ij\phi}$, with j = 1, 0, -1, we have

$$\mu_j P_{m,n}^l(\cos\theta) = \gamma_j \sum_h \langle l,1,m,0 \mid l+h,m\rangle \langle l,1,n,\pm j \mid l+h,n\pm j\rangle P_{m,n\pm j}^{l+h}(\cos\theta) \quad \text{(A.19)}$$

where j, h = +1, 0, -1, $\gamma_{\pm 1} = \mp i$ and γ_0 = 1, and <l_1, l_2, m_1, m_2|L,M> are Clebsch-Gordon coefficients in angular momentum theory [8], given by

$$\langle l-h,1,m,-j \mid l,m-j\rangle = \begin{bmatrix} \left[\frac{(l-m)(l-m+1)}{(2l-1)2l}\right]^{1/2} & \left[\frac{(l+m)(l-m+1)}{(2l-1)2l}\right]^{1/2} & \left[\frac{(l+m)(l+m+1)}{(2l+2)(2l+3)}\right]^{1/2} \\ \left[\frac{(l-m)(l+m)}{(2l-1)l}\right]^{1/2} & \frac{m}{[l(l+1)]^{1/2}} & -\left[\frac{(l+m+1)(l-m+1)}{(l+1)(2l+3)}\right]^{1/2} \\ \left[\frac{(l+m)(l+m+1)}{(2l-1)2l}\right]^{1/2} & -\left[\frac{(l-m)(l+m+1)}{2l(l+1)}\right]^{1/2} & \left[\frac{(l-m)(l-m+1)}{(2l+2)(2l+3)}\right]^{1/2} \end{bmatrix} \quad \text{(A.20)}$$

where the row index (from above) j = 1, 0, -1 and the column index (from left) h = 1, 0, -1 (the term of j = 0, h = 0 is misprinted in Ref.9).

The first cumulant (center of the spatial distribution)

The unnormalized first moment $\langle R_\alpha \rangle_m^{SP}$ in SP can be evaluated using the first order of Equ.(A.15)

$$\langle R_\alpha \rangle_m^{SP} = c\left\langle \int_0^t dt' s_\alpha(t') \right\rangle_m^{SP} = \left[\int_0^t dt' \int ds' F^{SP}(s,s',t-t') s_\alpha{}' F^{SP}(s',z,t') I^{SP(0)} \right]_m \quad \text{(A.21)}$$

The corresponding qualities in the CP can be written as

$$< R_\alpha >_m^{SP} = \left[\sum_j U_{\alpha j} \mathrm{T}^{-1} < \mathrm{R}_j > \mathrm{TI}^{SP(0)} \right]_m \quad \text{(A.22)}$$

with α = x,y,z and j = 1, 0, -1, the indices of the spherical harmonic basis. <R> in Equ. (A.22) is defined in CP as

$$\langle R_j \rangle_{mn_0} = c\int_0^t dt' \int ds' \sum_n F_{mn}(s,s',t-t') s_j{}' F_{nn_0}(s',z,t') \quad \text{(A.23)}$$

Substituting Equ.(A.4) and (A.5) to Equ.(A.23), and using the recurrence relation [Equ.(A.19)] and the orthogonality relation of GSF's, integrating over ds',dt' in Equ.(A.23), the unnormalized first moment in CP is given by

$$\langle R_j \rangle_{mn_0} = c\sum_l \left\{ P^l_{m,n_0-j}(\cos\theta) e^{-i(n_0-j)\phi} \gamma_j \sum_n \sum_h \frac{2(l-h)+1}{4\pi} D^{l,h}_{m,n,n_0}(t) \right.$$

$$\left. \times \langle l-h,1,n,0 \mid l,n \rangle \langle l-h,1,n_0,-j \mid l,n_0-j \rangle - \delta_{j,0}\delta_{m,n_0} \frac{2l+1}{4\pi} t e^{-\mu_s t} P^l_{0,0}(\cos\theta) e^{-in_0\phi} \right\} \quad \text{(A.24)}$$

$$D^{l,h}_{m,n,n_0}(t) = \sum_{i,j} \left[B^l_{mn}\right]_i \left[B^{l-h}_{nn_0}\right]_j \left(\frac{\exp(-\lambda_j^{l-h} t) - \exp(-\lambda_i^l t)}{\lambda_i^l - \lambda_j^{l-h}} \right) \exp(-\mu_a t) \quad \text{(A.25)}$$

where i, j = 1, 2, 3, 4 for $l \geq 2$, and i, j = 1, 2 for l = 1, 2.

In SP the *m*th component *m* = [**I**, **Q**, **U**, **V**] of the unnormalized first moment, with the initial polarized state $\mathbf{I}^{\mathrm{SP}(0)}$, is obtained from Equ.(A.22).

The center of photon distribution for the parallel polarized component is obtained by

$$R^{c}_{\parallel,\alpha}(s,t)=\frac{\left[\left\langle R_{\alpha}\right\rangle^{SP}_{I}+\left\langle R_{\alpha}\right\rangle^{SP}_{Q}\right]}{2F_{\parallel}(s,t)} \tag{A.26}$$

and $R^{c}_{\perp,\alpha}, R^{c}_{R,\alpha}, R^{c}_{L,\alpha}$ can be determined in a similar way.

As an example, supposed we need to calculate the center of the spatial distribution R_{x} for right-handed circularly polarized light ($R^{c}_{R,x}$). First, we obtain the angular distribution $F^{l}_{mn_0}(t)$ in CP using Equ.(A.9) and the center of the spatial distribution <R> in CP using Equ.(A.24). Then the corresponding mth component qualities $F^{SP}_{m}(\mathbf{s},t)$ and $\left\langle R_{x}\right\rangle^{SP}_{m}$ in the SP can be acquired from Equ.(A.11) and Equ.(A.22). $F_R(\mathbf{s},\mathrm{t})$ in Equ.(A.26) is obtained from Equ.A.(12c). $R^{c}_{R,x}$ is written as:

$$R^{c}_{R,x}(s,t)=\frac{\left[\left\langle R_{x}\right\rangle^{SP}_{I}+\left\langle R_{x}\right\rangle^{SP}_{V}\right]}{2F_{R}(s,t)} \tag{A.27}$$

The second cumulant (half-width of the spatial distribution)

The unnormalized second moment $\left\langle R_{\alpha}R_{\beta}\right\rangle^{SP}_{m}$ in SP can be evaluated using the second order of Equ.(A.16)

$$\left\langle R_{\alpha}R_{\beta}\right\rangle^{SP}_{m}=c^{2}\left\langle\int_{0}^{t}dt'\int_{0}^{t}dt''T\left[s_{\alpha}(t')s_{\beta}(t'')\right]\right\rangle^{SP}_{m}=c^{2}$$

$$\times\left\{\left[\int_{0}^{t}dt'\int_{0}^{t'}dt''\int ds'\int ds''F^{SP}(s,s',t-t')s_{\alpha}{}'F^{SP}(s',s'',t'-t'')s_{\beta}{}''F^{SP}(s'',z,t'')I^{SP(0)}\right]_{m}+(t.c)\right\} \tag{A.28}$$

Similarly, Equ.(A.28) is written as

$$\left\langle R_\alpha R_\beta \right\rangle_m^{SP} = \left[\sum_{j1} \sum_{j2} \left(U_{\alpha j_1} U_{\beta j_2} + U_{\alpha j_2} U_{\beta j_1} \right) T^{-1} \left\langle R_{j_2} R_{j_1} \right\rangle TI^{SP(0)} \right]_m \tag{A.29}$$

where $\left\langle R_{j_2} R_{j_1} \right\rangle$ is defined in the CP as

$$\left\langle R_{j_2} R_{j_1} \right\rangle_{mn_0} = c^2 \int_0^t dt' \int_0^{t'} dt'' \int ds' \int ds'' \sum_{n_2} F_{mn_2}(s, s', t-t') s_{j_2}{}' \sum_{n_1} F_{n_2 n_1}(s', s'', t'-t'') s_{j_1}{}'' F_{n_1 n_0}(s'', z, t'') \tag{A.30}$$

Substituting Equ.(A.4) and (A.5) to Equ.(A.30), and using the recurrence relation and the orthogonality relation of GSF's, the unnormalized second moment in CP is given by

$$\begin{aligned} \left\langle R_{j_2} R_{j_1} \right\rangle_{mn_0} = c^2 \sum_l \Bigg\{ & P^l_{m,n_0-j_1-j_2}(\cos\theta) e^{-i(n_0-j_1-j_2)\phi} \gamma_{j_2} \gamma_{j_1} \sum_{n_2} \sum_{n_1} \sum_{h_2} \sum_{h_1} \frac{2(l-h_2-h_1)+1}{4\pi} \\ & \times E^{l,h_2,h_1}_{m,n_2,n_1,n_0}(t) \langle l-h_2, 1, n_2, 0 \mid l, n_2 \rangle \langle l-h_2, 1, n_0-j_1, -j_2 \mid l, n_0-j_1-j_2 \rangle \\ & \times \langle l-h_2-h_1, 1, n_1, 0 \mid l-h_2, n_1 \rangle \langle l-h_2-h_1, 1, n_0, -j_1 \mid l-h_2, n_0-j_1 \rangle \\ & - \delta_{j_2,0} \delta_{j_1,0} \delta_{m,n_0} \frac{2l+1}{4\pi} \frac{t^2}{2} e^{-\mu_s t} P^l_{0,0}(\cos\theta) e^{-in_0\phi} \Bigg\} \end{aligned} \tag{A.31}$$

with

$$\begin{aligned} E^{l,h_2,h_1}_{m,n_2,n_1,n_0}(t) = & \sum_{i,j,f} \left[B^l_{mn_2} \right]_i \left[B^{l-h_2}_{n_2 n_1} \right]_j \left[B^{l-h_2-h_1}_{n_1 n_0} \right]_f \exp(-\mu_a t) \\ & \times \left(\frac{\exp\left(-\lambda_f^{l-h_2-h_1} t\right) - \exp\left(-\lambda_i^l t\right)}{\left(\lambda_j^{l-h_2} - \lambda_f^{l-h_2-h_1}\right)\left(\lambda_i^l - \lambda_f^{l-h_2-h_1}\right)} - \frac{\exp\left(-\lambda_j^{l-h_2} t\right) - \exp\left(-\lambda_i^l t\right)}{\left(\lambda_j^{l-h_2} - \lambda_f^{l-h_2-h_1}\right)\left(\lambda_i^l - \lambda_j^{l-h_2}\right)} \right) \end{aligned} \tag{A.32}$$

where $i, j, f = 1, 2, 3, 4$ for $l \geq 2$, and $i, j, f = 1, 2$ for $l = 1, 2$.

In SP, the mth component m = [**I**, **Q**, **U**, **V**] of the unnormalized second moment, with the initial polarized state $\mathbf{I}^{SP(0)}$ is obtained from Equ.(A.29)

The half-width of the photon distribution for the parallel polarized component is determined by

$$D_{\|,\alpha\beta}(s,t)=\frac{\left[\left\langle R_\alpha R_\beta\right\rangle_I^{SP}+\left\langle R_\alpha R_\beta\right\rangle_Q^{SP}\right]}{2F_{\|}(s,t)}-\frac{1}{2}R_{\|,\alpha}^{c}R_{\|,\beta}^{C} \tag{A.33}$$

and $D_{\perp,\alpha\beta}$, $D_{R,\alpha\beta}$, $D_{L,\alpha\beta}$ can be determined in a similar way.

Gaussian distribution of the polarized light

Terminating Equ.(A.14) at the second order of the cumulant and setting **s** in Cartesian coordinates, integration over **q** in Eq.(A.11) can be analytical performed, which leads to the following Gaussian approximation expression of the polarized photon distribution. When the initial $\mathbf{s}_0$ is set along z, it is given by

$$I_\nu(r,s,t)=\frac{F_\nu(s,t)}{(4\pi)^{3/2}}\frac{1}{[\det D_\nu]^{1/2}}\exp\left\{-\frac{1}{4}\left[(D_\nu)^{-1}\right]_{\alpha\beta}\left(r_\alpha-R_{\nu,\alpha}^{c}\right)\left(r_\beta-R_{\nu,\beta}^{c}\right)\right\} \tag{A.34}$$

where $\nu=\|,\perp,R,L$.

Equ.(A.34) gave an analytical expression for the backscattered intensity distribution of polarized light. For incident linearly polarized light, $\nu=\|$ and $\nu=\perp$ gave the time-resolved backscattering of light with parallel and perpendicular to incident polarization, respectively. For incident circularly polarized light, $\boldsymbol{\nu}$ = R and $\boldsymbol{\nu}$ = L gave the backscattered intensity distribution of right- and left-handed circularly polarized light, respectively. To obtain the intensity distribution for the scattered polarized light (I_υ), first we need provide the parameters (such as incident wavelength, size of the particle, refraction of the particle, refraction index of the surrounding medium, suspensions concentration) to calculate some scattering coefficients [such as μ_s, $p_{m,n}^{l}$ in the expression Π_{mn}^{l} of Equ.(A.7)], then we solve Equ.(A.7) to get the eigenvalue λ_i^l and expansion

coefficient $\left[B^{l}_{mn0}\right]_i$ in Equ.(A.9). After we have calculated those parameters, we can obtain $F^{l}_{mn_0}$, $\left\langle R_j \right\rangle_{mn_0}$, $\left\langle R_{j_2} R_{j_1} \right\rangle_{mn_0}$ in CP according to Equ.(A.9), (A.24), (A.31). Provided the incident Stokes parameters $\mathbf{I}^{\mathrm{SP}(0)}$, the values for F^{SP}_{m}, $\left\langle R_\alpha \right\rangle^{SP}_{m}$, $\left\langle R_\alpha R_\beta \right\rangle^{SP}_{m}$ in SP can be obtained through Equ. (A.11), (A.22), (A.29) and transformed to F_υ, $R_{\upsilon,\alpha}$, D_υ in Equ.(A.34) via Equ.(A.12), (A.26), (A.33). Finally, given the detector location r_α in Equ.(A.34), we can obtain I_υ in Equ.(A.34). We have developed an program to evaluate Equ.(A.34) in Appendix B. The numerical results for incident circularly polarized light are presented in Chapter 2. In Chapter 3, we used Equ.(A.34) to fit our experimental data.

References:

1. W. Cai, M. Lax, R. R. Alfano, Phys. Rev. E. **63**, 016606 (2000).
2. W. Cai, M. Xu, R. R. Alfano, Phys. Rev. E **71**, 041202 (2005).
3. J. W. Hovenier, C. V. M. van der Mee, Astron. Astrophys. **128**, 1 (1983).
4. R. P. Feynman, Phys. Rev. **84**, 108 (1951).
5. F. Dyson, *ibid*. **75**, 486 (1949).
6. S. H. Ma, *Statistical Mechanics* (World Scientific, Philadephia, 1985).
7. M. G. Kendall and A. Stuart, *The advanced theory of statistics* 3rd ed. (Hafner, New York, 1969), Vol.1.
8. B. M. Brink, G. M. Satchler, *Angular Momentum* (Clarendon Press, Oxford, 1962).
9. M. Gel'fand, Z. Ya. Sapiro, Amer. Math. Soc. Translations **2**, 207 (1956).

Appendix B

Computer program to calculate the polarized photon intensity distribution

This whole program is used to calculate the backscattering of polarized light in a turbid medium. The main program calculated the parallel, perpendicular, right-handed and left-handed circularly polarized backscattered light based on Equ. (2.8) or Equ.(A.34). The subroutines deals with the parameters needed in Equ.(2.8). Most of the subroutines are general programs, which can be used in this thesis as well as other purposes.

1. Main program: calculate the parallel ($\nu = \|$), perpendicular ($\nu = \perp$), right-handed ($\nu = R$) and left-handed ($\nu = L$) circularly polarized light according to Equ. (2.8) or Equ.(A.34)
2. Subroutine *RCP*(): calculate $\left\langle R_j \right\rangle_{mn_0}$ according to the Eq.(A.24)
3. Subroutine *Dcoeff*(): calculate the coefficient $D^{l,h}_{m,n,n_0}$ according to Equ.(A.25)
4. Subroutine *RRCP*(): calculate $\left\langle R_{j_2} R_{j_1} \right\rangle_{mn_0}$ according Equ. (A.31)
5. Subroutine *Ecoeff*(): calculate the coefficient $E^{l,h_2,h_1}_{m,n_2,n_1,n_0}$ according to Equ.(A.32)
6. Subroutine *RSP*(): calculate $\left\langle R_\alpha \right\rangle^{SP}_m$ in Cartesian basis and SP representation according to Equ.(A.22)
7. Subroutine *RRSP*(): calculate $\left\langle R_\alpha R_\beta \right\rangle^{SP}_m$ in Cartesian basis and SP representation according to Equ.(A.29)

8. Subroutine *FCP*(): calculate the angular distribution of light F_m^{SP} in Circular and Stokes representation according to Equ. (A.9),(A.11)
9. Subroutine *DSP*(): calculate the half-width of the spread of the distribution $D_{\|,\alpha\beta}$ in SP representation according to Equ.(A.33)
10. Subroutine *ISP*(): calculate the I_v according to Equ.(A.34)
11. Subroutine *GSPH3*(): calculate the generalized spherical function of $d_{m,n}^j$ in Equ.(2.7)
12. Subroutine *SPHER*(): calculate all the necessary single scattering parameters including the expansion coefficient p_{mn}^l in Equ.(2.6), (A.6),(A.7)
13. Subroutine *CCG*(): calculate the Clebsch-Gordan coefficients $\langle l-h,1,m,-j \mid l,m-j \rangle$ according to Equ.(A.20)
14. Subroutine *EIGEN*(): calculate Π_{mn}^l in Equ. (A.7), eigen-vector $\left[B_{mn_0}^l\right]_i$ in Equ.(A.9) and eigen-value λ_i^l in Equ. (A.10)

```
!   This program computes the backscattering of polarized in scattering media
!                                                (Equ. (A.34) in Ni's thesis)
!
!   This program is compiled with Microsoft Developer Studio (Fortran
!                                                    Powerstation 4.0)
!
!   The program is based on
!   1. W. Cai, M. Lax and R. R.Alfano, Analytical solution of the polarized
!      photon transport equation in an infinite uniform     medium using
!      cumulant expansion, Phys. Rev. E 63, 016606 (2000)
!   2. X. Ni, Light propagation in turbid and condensed media, PhD thesis at
!                City College of New York (2006)
!
!   Input parameters:
!
!      LAM - wavelength of the incident light in valcuum
!      I0 - incident Stokes parameter [I Q U V]
!           I0(1)--I, I0(2)--Q, I0(3)--U, I0(4)--V
!      rr - location of the detector
!           rr(1)-x, rr(2)-y, rr(3)-z
!      x - cosine of the zenith angle of the detector
```

```
!      psi1 - cosine of the azimuth angle of the detector
!      REFMED - !Refractive index of the surrounding medium
!      MRR    - (Real)relative refractive index( Sphere / Surrounding medium)
!      MRI    - (Imaginary)relative refractive index( Sphere /
!                                                    Surrounding medium)
!      R1 - Radius of particle
!      cc - Speed of light in vacuum
!      lt - number of transport mean free path
!      mua    - absorption coefficient
!      DDELT - desired numerical accuracy
!
!    Output information
!      Im_sp(1) - intensity of parallel to incident polarization
!         Im_sp(2) - intensity of perpendicular to incident polarization
!      Im_sp(3) - intensity of right-handed polarized light
!      Im_sp(4) - intensity of left-handed polarized light

    IMPLICIT REAL*8 (A-H,O-Z)
    PARAMETER (NMIE=200, NPL=2*NMIE)
    REAL*8 AL1(NPL),AL2(NPL),AL3(NPL),AL4(NPL),BET1(NPL),BET2(NPL)
    real*8 LAM,PPP(NPL,6), mus, mua,cc,Q1,lt, R1, DDELT,dt,MRR,MRI
    Integer L1MAX,nlt,i,j,k,STAT,NT
    complex*16 lambda(NPL,4),bb(NPL,4,4,4)

    complex*16 U(3,3),T(4,4),T1(4,4),d_sp(4,3,3),im_sp(4),rr(3)
    complex*16 r_cp(3,4,4),rr_cp(3,3,4,4),r_sp(3,4),rr_sp(3,3,4),   &
                                          f_cp(4,4),fm_sp(4)
    real*8 d_spR(4,3,3),d_spI(4,3,3),r_spR(3,4),r_spI(3,4),         &
                                           fm_spR(4),fm_spI(4)

    real*8 I0(4)
    real*8 x,d3(NPL,3,9)
    real*8 psi1,tt
    open (6, file='spher.print')
    open (10, file='spher.write')
    open(11,file='general.dat')
    open(120,file='dspr.dat')
    open(121,file='dspi.dat')
    open(130,file='rspr.dat')
    open(131,file='rspi.dat')
    open(140,file='fmspr.dat')
    open(141,file='fmspi.dat')
    LAM=0.61D0
    REFMED=1.33D0
    MRR=1.19D0
    MRI=0.00D0
    R1 = 0.350
    cc = 1.0d0
    lt = 1.0d0
    I0(1) = 1.0d0
    I0(2) = 0.0d0
    I0(3) = 0.0d0
    I0(4) = 1.0d0

    rr(1) = dcmplx(0.150d0,0.0d0)
    rr(2) = dcmplx(0.0d0,0.0d0)
    rr(3) = dcmplx(0.0d0,0.0d0)
    DDELT=1D-7
!U is the matrix for the transform from a spherical harmonic basis to a
!      Cartesian basis[Equ.(A.18)]
!T is the matrix for the transform from Stokes presentation to circular
!      presentation [Equ.(2.4b)]. T1 is the inverse of T
    U = reshape((/dcmplx(-1.0d0/dsqrt(2.0d0),0.0d0),dcmplx(0.0d0,0.0d0),  &
```

```
                                  dcmplx(1.0d0/dsqrt(2.0d0),0.0d0),   &
                 dcmplx(0.0d0,1.0d0/dsqrt(2.0d0)), dcmplx(0.0d0,0.0d0),  &
                                   dcmplx(0.0d0,1.0d0/dsqrt(2.0d0)),  &
                 dcmplx(0.0d0,0.0d0), dcmplx(1.0d0,0.0d0),dcmplx(0.0d0,  &
                  0.0d0)/),(/3,3/),(/dcmplx(0.0,0.0),dcmplx(0.0,0.0)/),  &
                                                        (/2,1/))

    T =  reshape((/dcmplx(0.0d0,0.0d0),    dcmplx(0.5d0,0.0d0),           &
                dcmplx(0.0d0,0.5d0), dcmplx(0.0d0,0.0d0),                 &
                dcmplx(0.5d0,0.0d0),dcmplx(0.0d0,0.0d0),                  &
                dcmplx(0.0d0,0.0d0),     dcmplx(0.5d0,0.0d0),             &
                dcmplx(0.5d0,0.0d0),dcmplx(0.0d0,0.0d0),                  &
                dcmplx(0.0d0,0.0d0),     dcmplx(-0.5d0,0.0d0),            &
                dcmplx(0.0d0,0.0d0),    dcmplx(0.5d0,0.0d0),              &
                dcmplx(0.0d0,-0.5d0),dcmplx(0.0d0,0.0d0)/),(/4,4/),       &
                (/dcmplx(0.0d0,0.0d0),dcmplx(0.0d0,0.0d0)/),(/2,1/))

    T1 = reshape((/dcmplx(0.0d0,0.0d0), dcmplx(1.0d0,0.0d0),              &
                  dcmplx(1.0d0,0.0d0), dcmplx(0.0d0,0.0d0),               &
                  dcmplx(1.0d0,0.0d0), dcmplx(0.0d0,0.0d0),               &
                  dcmplx(0.0d0,0.0d0), dcmplx(1.0d0,0.0d0),               &
                  dcmplx(0.0d0,-1.0d0),dcmplx(0.0d0,0.0d0),               &
                  dcmplx(0.0d0,0.0d0), dcmplx(0.0d0,1.0d0),               &
                  dcmplx(0.0d0,0.0d0), dcmplx(1.0d0,0.0d0),               &
                  dcmplx(-1.0d0,0.0d0),dcmplx(0.0d0,0.0d0)/),(/4,4/),     &

(/dcmplx(0.0d0,0.0d0),dcmplx(0.0d0,0.0d0)/),(/2,1/))
!      Calculation of Mie coefficient
    CALL SPHER (LAM,REFMED,MRR,MRI,R1,L1,AL1,AL2,AL3,AL4,BET1,BET2,   &
           CEXT,CSCA,DDELT,PPP,L1MAX,Q1)
    mus = cc/lt/(1.0d0-Q1)  !scattering coefficient
    mua = 0.0D0             !absorption coefficient
    CALL eigen(mus,PPP,lambda,bb,L1MAX)  !Calculate pii Equ.(A7),
                  !eigenstates Equ.(A9) and eigenvalues Equ.(10)
    x = -1.0d0
    call gsph3(x,d3, L1MAX,NPL) !Calculate generalized spherical function
    psi1 = 0.0d0
    NT = 600
    dt = 0.02d0
    write(11,110) NT
    write(11,111) dt
110 format(I4)
111 format(e13.7)
    STAT = 2
do nlt = 1,NT
    tt = 0.1+real(nlt-1)*dt
    if(STAT==1) then
        call FCP(f_cp,fm_sp,psi1,L1max,tt,d3,bb,mua,mus,lambda,NPL,T,T1,I0)
        call RCP(r_cp,psi1,L1max,tt,d3,bb,mua,mus,lambda,NPL)
        call RRCP(rr_cp,psi1,L1max,tt,d3,bb,mua,mus,lambda,NPL)
        call RSP(r_cp,r_sp,fm_sp,U,T,T1,I0)
        call RRSP(rr_cp,rr_sp,fm_sp,U,T,T1,I0)
        call DSP(d_sp,r_sp,rr_sp)
        do i=1,4
            do j=1,3
                write(120,12)dreal(d_sp(i,j,1)),dreal(d_sp(i,j,2)),      &
                                                dreal(d_sp(i,j,3))
                write(121,12)dimag(d_sp(i,j,1)),dimag(d_sp(i,j,2)),      &
                                                dimag(d_sp(i,j,3))
12              format(e13.7,' ',e13.7,' ',e13.7)
            end do
        end do
        do i=1,3
```

```
            write(130,13)dreal(r_sp(i,1)),dreal(r_sp(i,2)),      &
                         dreal(r_sp(i,3)),dreal(r_sp(i,4))
            write(131,13)dimag(r_sp(i,1)),dimag(r_sp(i,2)),      &
                                dimag(r_sp(i,3)),dimag(r_sp(i,4))
13          format(e13.7,' ',e13.7,' ',e13.7,' ',e13.7)
        end do
        write(140,14)dreal(fm_sp(1)),dreal(fm_sp(2)),            &
                     dreal(fm_sp(3)),dreal(fm_sp(4))
        write(141,14)dimag(fm_sp(1)),dimag(fm_sp(2)),            &
                     dimag(fm_sp(3)),dimag(fm_sp(4))
14      format(e13.7,' ',e13.7,' ',e13.7,' ',e13.7)
    else
        do i=1,4
            do j=1,3
                read(120,*)d_spR(i,j,1),d_spR(i,j,2),d_spR(i,j,3)
                read(121,*)d_spI(i,j,1),d_spI(i,j,2),d_spI(i,j,3)
                d_sp(i,j,1) = dcmplx(d_spR(i,j,1),d_spI(i,j,1))
                d_sp(i,j,2) = dcmplx(d_spR(i,j,2),d_spI(i,j,2))
                d_sp(i,j,3) = dcmplx(d_spR(i,j,3),d_spI(i,j,3))
            end do
        end do
        do i=1,3
            read(130,*)r_spR(i,1),r_spR(i,2),r_spR(i,3),r_spR(i,4)
            read(131,*)r_spI(i,1),r_spI(i,2),r_spI(i,3),r_spI(i,4)
            r_sp(i,1) = dcmplx(r_spR(i,1),r_spI(i,1))
            r_sp(i,2) = dcmplx(r_spR(i,2),r_spI(i,2))
            r_sp(i,3) = dcmplx(r_spR(i,3),r_spI(i,3))
            r_sp(i,4) = dcmplx(r_spR(i,4),r_spI(i,4))
        end do
        read(140,*)fm_spR(1),fm_spR(2),fm_spR(3),fm_spR(4)
        read(141,*)fm_spI(1),fm_spI(2),fm_spI(3),fm_spI(4)
        fm_sp(1) = dcmplx(fm_spR(1),fm_spI(1))
        fm_sp(2) = dcmplx(fm_spR(2),fm_spI(2))
        fm_sp(3) = dcmplx(fm_spR(3),fm_spI(3))
        fm_sp(4) = dcmplx(fm_spR(4),fm_spI(4))
    end if
    call ISP(d_sp,r_sp,fm_sp,Im_sp,rr)
    print *,nlt
    write(10,1) tt,dreal(Im_sp(1)), dreal(Im_sp(2)),dreal(Im_sp(3)), &
                                                    dreal(Im_sp(4))
    write(6,1)  tt,dimag(Im_sp(1)), dimag(Im_sp(2)),dimag(Im_sp(3)), &
                                                    dimag(Im_sp(4))
1   format(e13.7,' ',e13.7,' ',e13.7,' ',e13.7,' ',e13.7)
end do !end of nlt_loop
end

!      Calculation <Rj>mn0 according to the Eq.(A.24)
!      R(m,n0,j,lmax) represents the position of the center of the distribution
!      Input
!            x  = cosine of the zenith angle
!            psi1 = azimuth angle
!      Output:
!            r_cp[j,m,n]
    subroutine RCP(r_cp,psi1,L1max,tt,d3,bb,mua,mus,lambda,NPL)
    implicit integer (a-z)
    Real*8 Rjr, Rji, part, partr,parti,psi1,tt,d3(NPL,3,9),mua,mus,Rjr1,Rji1
    Real*8 CCG
    complex*16 r_cp(3,4,4),Dcoeff,bb(NPL,4,4,4),lambda(NPL,4),DcoeffC
    real*8 C_const, PI, DcoeffR, DcoeffI,ccgVal1,ccgVal2,d3Val
    PI=4.d0*ATAN(1.d0)
    C_const = 1.0D0
    do j1 = 1,3
       do m1 = 1,4
```

```
 do n1 = 1,4
 select case (m1)
 case (1)
     m = 2
 case (2)
     m = 0
 case (3)
     m = 0
 case (4)
     m = -2
 end select
 select case (n1)
 case (1)
     n0 = 2
 case (2)
     n0 = 0
 case (3)
     n0 = 0
 case (4)
     n0 = -2
 end select
 j = 2-j1
 Lmin = max(IABS(m),IABS(n0-j))+1
 Rjr = 0.00
 Rji = 0.00
 ! partr,parti = (i**(m-n0+j))*(exp(-i(n0-j)*psi1)*gamma(j)
 if      (j1 == 1) then
     j = 1
     partr = dsin((n0-j)*psi1)*(-1.0d0)
     parti = dcos((n0-j)*psi1)*(-1.0d0)
 else
    if (j1 == 2) then
         j = 0
         partr = dcos((n0-j)*psi1)
         parti = dsin((j-n0)*psi1)
    else
         j = -1
         partr = -dsin((n0-j)*psi1)*(-1.0d0)
         parti = -dcos((n0-j)*psi1)*(-1.0d0)
    end if
 end if
 if (mod(m-n0+j,4)/=0) then
     if (mod(m-n0+j,2)==0) then
         partr = -partr
         parti = -parti
     else
         if (mod(m-n0+j-1,4)==0) then
             part = partr
             partr = -parti
             parti = part
         else
             part = partr
             partr = parti
             parti = -part
         end if
     end if
  end if
do L2 = Lmin,L1max-1
     L1 = L2-1
     d3Val = d3(L2,(m+4)/2,n0-j+5)

     do  n2 = 1,4
         select case (n2)
```

```
                    case (1)
                        n = 2
                    case (2)
                        n = 0
                    case (3)
                        n = 0
                    case (4)
                        n = -2
                    end select
                    do     h1= 1,3
                        h = 2-h1
                        ! d3(l,m,n): m=1,2,3        represnet -2,0,0,2
                        !                n=1,2,....9    represnet -4,....,4
                        !Dm,n,n0,l,h:m,n,n0=1,2,3,4 represnet      2,0,0,2
                        !            h=1,2,3        represnet 1, 0, -1
                        DcoeffC = Dcoeff(m1,n2,n1,L2,h,tt,bb,mua,lambda,NPL)
                        DcoeffR = dreal(DcoeffC)
                        DcoeffI = dimag(DcoeffC)
                        ccgVal1 = CCG(L1-h,1,n,0,L1,n)
                        ccgVal2 = CCG(L1-h,1,n0,-j,L1,n0-j)


                        Rjr1 = C_const*d3Val*real(2*(L1-h)+1)*0.25d0/PI*   &
                               ccgVal1*ccgVal2*(partr*DcoeffR-parti*DcoeffI)
                        Rjr = Rjr+ Rjr1
                        Rji1= C_const*d3Val*real(2*(L1-h)+1)*0.25d0/PI     &
                              *ccgVal1*ccgVal2*(parti*DcoeffR+partr*DcoeffI)
                        Rji = Rji+Rji1
                    end do !end_loop h1
                end do        !end_loop n2
                if ((m1==n1) .AND. (j1==2)) then
                    Rjr = Rjr - real((2*L2-1))*0.25d0/PI*dexp(-mus*tt)*tt* &
                          d3(L2,2,5)
                end if
              end do       !end_loop L2
            r_cp(j1,m1,n1) = dcmplx(Rjr,Rji)
            end do  !end_loop n1
        end do             !end_loop m1
    end do                 !end_loop j1

    return
    end


!Calculation of coefficient D(m,n,n0,l,h) according to Equ.(A.25)
!Input:
!   m=1,2,3,4  represent +2,0,-0,-2
!   n=1,2,3,4  represent +2,0,-0,-2
!   n0=1,2,3,4 represent +2,0,-0,-2
!   h=1,0,-1
    complex*16 function Dcoeff(m,n,n0,l,h,tt,bb,mua,lambda,NPL)
    implicit integer (a-z)
!   implicit none
    Real*8 tt,mua
    complex*16 bb(NPL,4,4,4),lambda(NPL,4),ff,ff1,temp
    !complex*8 ret
    Dcoeff = dcmplx(0.0d0,0.0d0)
    do i = 1,4
        do   j = 1,4
            if ((l-h-1)>=0) then
               if ((cdabs(bb(l,i,m,n)) .GT. 1.0e-13)                &
                .AND. (cdabs(bb(l-h,j,n,n0)) .GT. 1.0e-13)          &
                .AND. (dabs(cdabs(lambda(l,i)-lambda(l-h,j)))       &
```

```
                .GT. 1.0e-13)) then

                    temp = lambda(l,i)*tt
                    ff1 =  ff(lambda(l,i)-lambda(l-h,j),tt,temp)
                    Dcoeff = Dcoeff+bb(l,i,m,n)*bb(l-h,j,n,n0)*       &
                             ff1*dexp(-mua*tt)
               else
                    if ((cdabs(bb(l,i,m,n)) .GT. 1.0e-13)             &
                       .AND. (cdabs(bb(l-h,j,n,n0)) .GT. 1.0e-13)     &
                       .AND. (dabs(cdabs(lambda(l,i)-lambda(l-h,j)))  &
                                .LE. 1.0e-13)) then
                           ff1= cdexp(-lambda(l,i)*tt)*tt
                           Dcoeff = Dcoeff+bb(l,i,m,n)*bb(l-h,j,n,n0) &
                                    *ff1*exp(-mua*tt)
                    end if
               end if
            end if
        end do !end_loop of j
    end do    !end_loop of i
    end      function

!Calcualtion of ff = (exp(xt)-1)/x
    complex*16 function ff(x,t,temp)
    implicit none
    complex*16 x,temp
    real*8 t
    ff =dcmplx(0.0d0,0.0d0)
    if (cdabs(x*t) < 1.0e-6) then
       ff = (t+0.5d0*x*t*t)*cdexp(-temp)
    else
       ff = (cdexp(x*t-temp)-cdexp(-temp))/x
    end if
    end function



!Calculation of <Rj2Rj1>mn0 according Equ. (A.31)
!   Input
!       m1 = 1,2,3,4 represent m = 2,0,-0,-2
!       n1 = 1,2,3,4 represent n0 = 2,0,-0,-2
!       j1 = +1,0,-1
!       j2 = +1,0,-1
!       x  = cosine of the zenith angle
!       psi1 = azimuth angle
!   Output:
!   <Rj1Rj2>mn0
subroutine RRCP(rr_cp,psi1,L1max,tt,d3,bb,mua,mus,lambda,NPL)
implicit none
integer NPL,Lmin,l1max
integer m1,n1,j0,j,j1,j2,m,n0,k1,k2,k3,k4,h1,h2,h3,h4,L1,L2
complex*16 rr_cp(3,3,4,4),Ecoeff,bb(NPL,4,4,4),lambda(NPL,4),EcoeffC
real*8 d3(NPL,3,9), CCG,mua,mus,tt
real*8 C_const, PI,EcoeffR,EcoeffI,ccgVal1,ccgVal2,ccgVal3,ccgVal4,d3Val
real*8 RRjr, RRji, partr, parti, part, psi1

PI=4.d0*ATAN(1.d0)
C_const = 1.0d0

do j0 = 1,3
    do j = 1,3
        do n1 = 1,4
            do m1 = 1,4
                j2 = 2-j0
```

```
j1 = 2-j
select case (m1)
case (1)
    m = 2
case (2)
    m = 0
case (3)
    m = 0
case (4)
    m = -2
end select
select case (n1)
case (1)
    n0 = 2
case (2)
    n0 = 0
case (3)
    n0 = 0
case (4)
    n0 = -2
end select
Lmin = max(IABS(m),IABS(n0-j2-j1))+1
RRjr = 0.00d0
RRji = 0.00d0
select case (j2+j1)
case (2)
    partr = -dcos((n0-j2-j1)*psi1)
    parti = dsin((n0-j2-j1)*psi1)
case (1)
    partr = dsin((n0-j2-j1)*psi1)*(-1.0d0)
    parti = dcos((n0-j2-j1)*psi1)*(-1.0d0)
case (0)
    partr = dcos((n0-j2-j1)*psi1)
    parti = dsin((j2+j1-n0)*psi1)
case (-1)
    partr = -dsin((n0-j2-j1)*psi1)*(-1.0d0)
    parti = -dcos((n0-j2-j1)*psi1)*(-1.0d0)
case (-2)
    partr = -dcos((n0-j2-j1)*psi1)
    parti = dsin((n0-j2-j1)*psi1)
end select
if (mod(m-n0+j2+j1,4)/=0) then
    if (mod(m-n0+j2+j1,2)==0) then
        partr = -partr
        parti = -parti
    else
        if (mod(m-n0+j2+j1-1,4)==0) then
            part = partr
            partr = -parti
            parti = part
        else
            part = partr
            partr = parti
            parti = -part
         end if
     end if
end if
do L2 = Lmin, L1max-2
    L1 = L2 -1
    d3Val = d3(L2,(m+4)/2,n0-j2-j1+5)
    do h4=1,3
        h2 = 2-h4
        do h3=1,3
```

```
                                h1 = 2-h3
                                do   k4=1,4
                                    select case (k4)
                                    case (1)
                                        k2 = 2
                                    case (2)
                                        k2 = 0
                                    case (3)
                                        k2 = 0
                                    case (4)
                                        k2 = -2
                                    end select
                                    do k3=1, 4
                                        select case (k3)
                                            case (1)
                                                k1 = 2
                                            case (2)
                                                k1 = 0
                                            case (3)
                                                k1 = 0
                                            case (4)
                                                k1 = -2
                                        end select
                                        EcoeffC = Ecoeff(m1,k4,k3,n1,L1,h2,    &
                                                  h1,tt,bb,mua,lambda,NPL)
                                        EcoeffR = dreal(EcoeffC)
                                        EcoeffI = dimag(EcoeffC)
                                        ccgVal1 = CCG(L1-h2,1,k2,0,L1,k2)
                                        ccgVal2 = CCG(L1-h2,1,n0-j1,-j2,L1,     &
                                                  n0-j1-j2)
                                        ccgVal3 = CCG(L1-h2-h1,1,k1,0,L1-h2,k1)
                                        ccgVal4 = CCG(L1-h2-h1,1,n0,-j1,         &
                                                  L1-h2,n0-j1)
                                        RRjr = RRjr+C_const**2*d3Val*            &
                                               real(2*(L1-h2-h1)+1)*0.25d0/PI*   &
                                               ccgVal1*ccgVal2*ccgVal3*ccgVal4 & 
                                               *(partr*EcoeffR-parti*EcoeffI)
                                        RRji = RRji+C_const**2*d3Val*real(2*    &
                                               (L1-h2-h1)+1)*0.25d0/PI*          &
                                               ccgVal1*ccgVal2*ccgVal3*ccgVal4 & 
                                               *(partr*EcoeffI+parti*EcoeffR)
                                    end do  !end_loop k3
                                end do             !end_loop k4
                            end do                 !end_loop h3
                        end do                     !end_loop h4
                    !modified on 04/05/05 to add ballistic component
                    if ((m1==n1) .AND. (j==2) .AND. (j0==2)) then
                         RRjr = RRjr - real((2*L2-1))*0.25d0/PI*dexp(-mus*tt)   &
                                                *tt*tt*0.5d0*d3(L2,2,5)
                    end if
                    end do                                 !end_loop L2
                    rr_cp(j0,j,m1,n1) = dcmplx(RRjr,RRji)
!                   write(10,*)      j0,j,m1,n1,rr_cp(j0,j,m1,n1)
                end do  !end_loop m1 (m)
            end do             !end_loop n1 (n0)
        end do                 !end_loop j (j1)
    end do                     !end_loop j0 (j2)

    end


    !Calculation of coefficient E(m,n2,n1,n0,l,h2,h1) according to Equ.(A.32)
    !Input:
```

```
!   m=1,2,3,4         represent +2,0,-0,-2
!   n2,n1,n0=1,2,3,4  represent +2,0,-0,-2
!   h2,h1=1,0,-1
    complex*16 function Ecoeff(m,n2,n1,n0,l,h2,h1,tt,bb,mua,lambda,NPL)
    implicit integer (a-z)
!   implicit none
    Real*8 tt,mua
    Integer NPL
    complex*16 bb(NPL,4,4,4),lambda(NPL,4),eff,ff,ff1,ff2,temp
    Ecoeff = Dcmplx(0.0d0,0.0d0)
    L2 = l + 1
    do i=1,4
        do   j=1,4
            do f=1,4
                if (((l-h2) .GE. 0) .AND. ((l-h2-h1) .GE. 0) .AND.  &
                    (cdabs(bb(L2,i,m,n2)) .GT. 1.0e-13) .AND.       &
                    (cdabs(bb(L2-h2,j,n2,n1)) .GT. 1.0e-13) .AND.   &
                    (cdabs(bb(L2-h2-h1,f,n1,n0)) .GT. 1.0e-13)) then
                    temp = lambda(L2,i)*tt
                    if ((dabs(cdabs(lambda(L2-h2,j)-lambda(L2-h2-h1,f)))  &
                          .GT. 1.0e-13) .AND. (dabs(cdabs(lambda(L2,i)-    &
                          lambda(L2-h2,j))) .GT. 1.0e-13)) then
                            if (dabs(cdabs(lambda(L2,i)-lambda(L2-h2-h1,f &
                                ))) .GT. 1.0e-13) then
                                Ecoeff = Ecoeff+bb(L2,i,m,n2)*bb(L2-h2,j, &
                                           n2,n1)*bb(L2-h2-h1,f,n1,n0)*   &
                                        eff(lambda(L2,i)-lambda(L2-h2-h1, &
                                        f),lambda(L2,i)-lambda(L2-h2,j),  &
                                       lambda(L2-h2,j)-lambda(L2-h2-h1,f) &
                                                  ,tt,temp)*dexp(-mua*tt)
                             else
                                 Ecoeff = Ecoeff+bb(L2,i,m,n2)*bb(L2-h2,j, &
                                           n2,n1)*bb(L2-h2-h1,f,n1,n0)*ff2 &
                                           (lambda(L2,i)-lambda(L2-h2,j),  &
                                                tt,temp)*dexp(-mua*tt)

                             end if
                     else
                        if ((dabs(cdabs(lambda(L2-h2,j)-lambda(L2-h2-h1,f &
                           ))) .LE. 1.0e-13) .AND. (dabs(cdabs(lambda(L2, &
                           i)-lambda(L2-h2,j))) .GT. 1.0e-13)) then
                                Ecoeff = Ecoeff+bb(L2,i,m,n2)*bb(L2-h2,j, &
                                         n2,n1)*bb(L2-h2-h1,f,n1,n0)*     &
                                         cdexp(-lambda(L2,i)*tt)*ff1(     &
                                         lambda(L2,i)-lambda(L2-h2,j),tt)
                        else
                           if ((dabs(cdabs(lambda(L2,i)-lambda(L2-h2,j))) &
                                .LE. 1.0e-13) .AND. (dabs(cdabs(lambda(L2 &
                                 -h2,j)-lambda(L2-h2-h1,f))) .GT.         &
                                 1.0e-13)) then
                                   Ecoeff = Ecoeff+bb(L2,i,m,n2)*bb(L2-h2 &
                                            ,j,n2,n1)*bb(L2-h2-h1,f,n1,n0 &
                                             )*ff2(lambda(L2-h2,j)-lambda &
                                             (L2-h2-h1,f),tt,temp)
                           else
                               if ((dabs(cdabs(lambda(L2-h2,j)-lambda(L2  &
                                   -h2-h1,f))) .LE. 1.0e-13) .AND. (dabs  &
                                   (cdabs(lambda(L2,i)-lambda(L2-h2,j)))  &
                                   .LE. 1.0e-13)) then
                                   Ecoeff = Ecoeff+bb(L2,i,m,n2)*bb(L2-h2 &
                                            ,j,n2,n1)*bb(L2-h2-h1,f,n1,n0 &
                                            )*cdexp(-lambda(L2,i)*tt)*tt  &
                                            *tt*0.5d0
```

```
                                end if
                             end if
                          end if
                       end if
                    end if
                end do
            end do
        end do
        end      function


!Calculation of (ff(cc)-ff(aa))/bb1 where bb1 = cc - aa
complex*16 function eff(cc,aa,bb1,tt,temp)
implicit none
complex*16 cc,aa,bb1,ff,temp
real*8 tt
eff = dcmplx(0.0d0,0.0d0)
if (cdabs(bb1)>1.0e-6) then
    eff = (ff(cc,tt,temp)-ff(aa,tt,temp))/bb1
else
    if (cdabs(aa*tt)<1.0e-6) then
       eff = 0.5d0*tt*tt*cdexp(-temp)
    else
        eff = ((aa*tt-1.0d0)*cdexp(aa*tt-temp)+cdexp(-temp))/aa/aa
    end if
end if
end function

!Calcualtion of ff1 = t*exp(x*t)/x-(exp(x*t)-1)/x/x
    complex*16 function ff1(x,t)
    implicit none
    complex*16 x
    real*8 t
    ff1 = dcmplx(0.0d0,0.0d0)
    if (cdabs(x*t) < 1.0e-6) then
        ff1 = 0.5d0*t*t+0.5d0*x*t*t*t*t               ! 0.5d0*t*t
    else
        ff1 = t*cdexp(x*t)/x-(cdexp(x*t)-1.0d0)/x/x
    end if
    end function


!Calcualtion of ff2 = (exp(x*t)-1)/x/x-t/x
    complex*16 function ff2(x,t,temp)
    implicit none
    complex*16 x,temp
    real*8 t
    ff2 = dcmplx(0.0d0,0.0d0)
    if (cdabs(x*t) < 1.0e-6) then
        ff2 = 0.5d0*t*t*cdexp(-temp)
    else
        ff2 = (cdexp(x*t-temp)-cdexp(-temp))/x/x-cdexp(-temp)*t/x
    end if
    end function



!Calculation of <Ra>m in Cartesian basis according to Equ.(A.22)
!Input:
!   a=1,2,3         represent +2,0,-0,-2
!   I0(4)           represent the initial state Isp(0)
```

```
subroutine RSP(r_cp,r_sp,fm_sp,U,T,T1,I0)
implicit none
Integer a,j,k
real*8 I0(4)
complex*16 U(3,3),T(4,4),T1(4,4),Rj(4,4),r_cp(3,4,4),r_sp(3,4)
complex*16 fm_sp(4),temp1(4),rsp1,rsp2,rsp3,rsp4
do a = 1,3
    r_sp(a,1) = dcmplx(0.0d0,0.0d0)
    r_sp(a,2) = dcmplx(0.0d0,0.0d0)
    r_sp(a,3) = dcmplx(0.0d0,0.0d0)
    r_sp(a,4) = dcmplx(0.0d0,0.0d0)
    do j = 1,3
        Rj(1,1) = r_cp(j,1,1)
        Rj(1,2) = r_cp(j,1,2)
        Rj(1,3) = r_cp(j,1,3)
        Rj(1,4) = r_cp(j,1,4)
        Rj(2,1) = r_cp(j,2,1)
        Rj(2,2) = r_cp(j,2,2)
        Rj(2,3) = r_cp(j,2,3)
        Rj(2,4) = r_cp(j,2,4)
        Rj(3,1) = r_cp(j,3,1)
        Rj(3,2) = r_cp(j,3,2)
        Rj(3,3) = r_cp(j,3,3)
        Rj(3,4) = r_cp(j,3,4)
        Rj(4,1) = r_cp(j,4,1)
        Rj(4,2) = r_cp(j,4,2)
        Rj(4,3) = r_cp(j,4,3)
        Rj(4,4) = r_cp(j,4,4)
        temp1 = MATMUL(T1,MATMUL(Rj,MATMUL(T,I0)))
        do k = 1,4
            temp1(k) = U(a,j)*temp1(k)
            r_sp(a,k) = r_sp(a,k)+temp1(k)
        end do
    end do
    !Parallel----I + Q
    if (cdabs(fm_sp(1)+fm_sp(2)) > 1.0e-7) then
        rsp1 = (r_sp(a,1)+r_sp(a,2))/(fm_sp(1)+fm_sp(2))
    else
        rsp1 = dcmplx(0.0D0,0.0d0)
    end if
    !Perpendicular----I - Q
    if (cdabs(fm_sp(1)-fm_sp(2)) > 1.0e-7) then
        rsp2 = (r_sp(a,1)-r_sp(a,2))/(fm_sp(1)-fm_sp(2))
    else
        rsp2 = dcmplx(0.0D0,0.0d0)
    end if
    !Right-handed----I + V
    if (cdabs(fm_sp(1)+fm_sp(4)) > 1.0e-7) then
        rsp3 = (r_sp(a,1)+r_sp(a,4))/(fm_sp(1)+fm_sp(4))
    else
        rsp3 = dcmplx(0.0D0,0.0d0)
    end if
    !Left-handed----I - V
    if (cdabs(fm_sp(1)-fm_sp(4)) > 1.0e-7) then
        rsp4 = (r_sp(a,1)-r_sp(a,4))/(fm_sp(1)-fm_sp(4))
    else
        rsp4 = dcmplx(0.0D0,0.0d0)
    end if
    r_sp(a,1) = rsp1
    r_sp(a,2) = rsp2
    r_sp(a,3) = rsp3
    r_sp(a,4) = rsp4
  end do
```

```
      end

!Calculation of <Rj1Rj2>mn0 in Cartesian basis according to Equ.(A.29)
!Input:
!   m,n0=1,2,3,4         represent +2,0,-0,-2
!   j1,j2=1,2,3       represent +1,0,-1
!   I0(4)           represent the initial state Isp(0)
!parameter: a - alpha, b - beta
    subroutine RRSP(rr_cp,rr_sp,fm_sp,U,T,T1,I0)
    implicit none
    Integer a,b,j1,j2,k
    real*8 I0(4)
    complex*16 U(3,3),T(4,4),T1(4,4),RRj(4,4),rr_sp(3,3,4)
    complex*16 rr_cp(3,3,4,4),fm_sp(4),temp2(4)
    complex*16      rrsp1,rrsp2,rrsp3,rrsp4
    do a = 1,3
        do b = 1,3
            rr_sp(a,b,1) = dcmplx(0.0d0,0.0d0)
            rr_sp(a,b,2) = dcmplx(0.0d0,0.0d0)
            rr_sp(a,b,3) = dcmplx(0.0d0,0.0d0)
            rr_sp(a,b,4) = dcmplx(0.0d0,0.0d0)
            do j1 = 1,3
                do j2 = 1,3
                    RRj(1,1) = rr_cp(j2,j1,1,1)
                    RRj(1,2) = rr_cp(j2,j1,1,2)
                    RRj(1,3) = rr_cp(j2,j1,1,3)
                    RRj(1,4) = rr_cp(j2,j1,1,4)
                    RRj(2,1) = rr_cp(j2,j1,2,1)
                    RRj(2,2) = rr_cp(j2,j1,2,2)
                    RRj(2,3) = rr_cp(j2,j1,2,3)
                    RRj(2,4) = rr_cp(j2,j1,2,4)
                    RRj(3,1) = rr_cp(j2,j1,3,1)
                    RRj(3,2) = rr_cp(j2,j1,3,2)
                    RRj(3,3) = rr_cp(j2,j1,3,3)
                    RRj(3,4) = rr_cp(j2,j1,3,4)
                    RRj(4,1) = rr_cp(j2,j1,4,1)
                    RRj(4,2) = rr_cp(j2,j1,4,2)
                    RRj(4,3) = rr_cp(j2,j1,4,3)
                    RRj(4,4) = rr_cp(j2,j1,4,4)
                    temp2 = MATMUL(T1,MATMUL(RRj,MATMUL(T,I0)))
                    do k = 1,4
                        temp2(k) = (U(a,j1)*U(b,j2)+U(a,j2)*U(b,j1))*temp2(k)
                        rr_sp(a,b,k) = rr_sp(a,b,k)+temp2(k)
                    end do
                end do
            end do
            if (cdabs(fm_sp(1)+fm_sp(2)) > 1.0e-7) then
                rrsp1 = (rr_sp(a,b,1)+rr_sp(a,b,2))/(fm_sp(1)+fm_sp(2))
            else
                rrsp1 = dcmplx(0.0D0,0.0d0)
            end if
            if (cdabs(fm_sp(1)-fm_sp(2)) > 1.0e-7) then
                rrsp2 = (rr_sp(a,b,1)-rr_sp(a,b,2))/(fm_sp(1)-fm_sp(2))
            else
                rrsp2 = dcmplx(0.0D0,0.0d0)
            end if
            if (cdabs(fm_sp(1)+fm_sp(4)) > 1.0e-7) then
                rrsp3 = (rr_sp(a,b,1)+rr_sp(a,b,4))/(fm_sp(1)+fm_sp(4))
            else
                rrsp3 = dcmplx(0.0D0,0.0d0)
            end if
            if (cdabs(fm_sp(1)-fm_sp(4)) > 1.0e-7) then
                rrsp4 = (rr_sp(a,b,1)-rr_sp(a,b,4))/(fm_sp(1)-fm_sp(4))
```

```
            else
                rrsp4 = dcmplx(0.0D0,0.0d0)
            end if
            rr_sp(a,b,1)=rrsp1
            rr_sp(a,b,2)=rrsp2
            rr_sp(a,b,3)=rrsp3
            rr_sp(a,b,4)=rrsp4
        end do
    end do
 end


!Exact solution in the light direction space, CP and SP representation
!Equ. (A.9),(A.11)
subroutine FCP(f_cp,fm_sp,psi1,L1max,tt,d3,bb,mua,mus,lambda,NPL,T,T1,I0)
    implicit integer (a-z)
    Real*8 psi1,tt,d3(NPL,3,9),mua,mus
    complex*16 f_cp(4,4),fm_sp(4),bb(NPL,4,4,4)
    complex*16 lambda(NPL,4),T(4,4),T1(4,4),Fcoeff,Fmn0
    real*8 I0(4)
    real*8 C_const, PI
    Real*8 part, partr,parti,partC
    PI=4.d0*ATAN(1.d0)
    C_const = 1.0D0
    do m1 =1,4
        select case (m1)
        case (1)
            m = 2
        case (2)
            m = 0
        case (3)
            m = 0
        case (4)
            m = -2
        end select
        do n1 = 1,4
            select case (n1)
            case (1)
                n0 = 2
            case (2)
                n0 = 0
            case (3)
                n0 = 0
            case (4)
                n0 = -2
            end select
            Fmn0 = dcmplx(0.0d0,0.0d0)
            do L1 = 1, L1max
                Fcoeff = dcmplx(0.0d0,0.0d0)
                do i = 1,4
                   Fcoeff = Fcoeff+real((2*L1-1))*0.25d0/PI*bb(L1,i,m1,n1)   &
                             *cdexp(-lambda(L1,i)*tt)
                end do  !end of i_loop
                partr = dcos(real(n0)*psi1)
                parti = -dsin(real(n0)*psi1)
                if (mod(m-n0,4)/=0) then
                    if (mod(m-n0,2)==0) then
                        partr = -partr
                        parti = -parti
                    else
                       if (mod(m-n0-1,4)==0) then
                            part = partr
                            partr = -parti
```

```
                        parti = part
                    else
                        part = partr
                        partr = parti
                        parti = -part
                    end if
                end if
            end if
            partC = dcmplx(partr,parti)
            Fmn0 = Fmn0 + Fcoeff*partC*d3(L1,(m+4)/2,n0+5)*dexp(-mua*tt)
            if (m1==n1)      then
                Fmn0 = Fmn0- real((2*L1-1))*0.25d0/PI*                &
                            dexp(-mus*tt)*d3(L1,2,5)
            end if
        end do               !end of      L1_loop
        f_cp(m1,n1) = Fmn0
    end do                          !end of n1_loop
end do                              !end of m1_loop
 fm_sp = MATMUL(T1,MATMUL(f_cp,MATMUL(T,I0)))
end


!Calculation of the half-width of the spread of the distribution
!<Dm>ab in SP basis according to Equ.(A.33)
subroutine DSP(d_sp,r_sp,rr_sp)
implicit integer (a-z)
complex*16 d_sp(4,3,3),rr_sp(3,3,4),r_sp(3,4)
do m =1,4
 do a = 1,3
    do b = 1,3
      d_sp(m,a,b) = 0.5*(rr_sp(a,b,m)-r_sp(a,m)*r_sp(b,m))
    end do !end of b_loop
end do     !end of a_loop
end do       !end of m_loop
end


!Calculation of the ImSP according to Equ.(A.34)
!Stokes parameter along the z-axis
subroutine ISP(d_sp,r_sp,fm_sp,Im_sp,rr )
implicit none
integer m,i,j
complex*16 d_sp(4,3,3),r_sp(3,4),fm_sp(4),fsp(4),Im_sp(4)
complex*16 fsp1,fsp2,fsp3,fsp4,dd_inv(3,3),rr(3),CDet
real*8 DetR,DetI,Det,ddR(3,3), ddI(3,3)
real*8 PI

PI=4.d0*ATAN(1.d0)
fsp(1)=(fm_sp(1)+fm_sp(2))*0.5D0
fsp(2)=(fm_sp(1)-fm_sp(2))*0.5D0
fsp(3)=(fm_sp(1)+fm_sp(4))*0.5D0
fsp(4)=(fm_sp(1)-fm_sp(4))*0.5D0

do m = 1,4
    Im_sp(m) = dcmplx(0.0d0,0.0d0)
    do i = 1,3
        do j = 1,3
            ddR(i,j) = dreal(d_sp(m,i,j))
            ddI(i,j) = dimag(d_sp(m,i,j))
        end do !end of j_loop
    end do     !end of i_loop
    CALL inverse_33c(ddR,ddI,dd_inv,DetR,DetI)
    Det = dsqrt(DetR**2+DetI**2)
```

```
    CDet = dcmplx(DetR, DetI)
!   if (dabs(Det) > 1.0e-13) then
        do i = 1,3
            do j = 1,3
                Im_sp(m) = Im_sp(m)+dd_inv(i,j)*(rr(i)-r_sp(i,m))  &
                                                *(rr(j)-r_sp(j,m))
            end do
        end do
        if(dreal(Im_sp(m))>-20.0d0) then
            Im_sp(m) = fsp(m)*cdexp(-0.25d0*Im_sp(m))/cdsqrt       &
                       (4.0d0*PI*4.0d0*PI*4.0d0*PI*CDet)
        else
            Im_sp(m) = dcmplx(0.0d0,0.0d0)
        end if
        if (cdabs(Im_sp(m)) < 1.0e-13) then
            Im_sp(m) = dcmplx(0.0d0,0.0d0)
        end if
end do  !end of m_loop
end


!  This program produces a group of the generalized spherical function
!  of d(l,m,n) in Equ.(2.7)
!  for compute polarized distribution function up to 2nd cumulant;
!     Input
!
!     out_put: d3(l3,m3,n3)
!  l3=1,....,LL+1    means l=0, .....,LL
!  m3=1,2,3          means m=-2,0,2       m=2*m3-4
!  n3=1,2,....,9     means n=-4,....,4    n=n3-5
!     This subroutine is used for Equ.(A.4), Equ.(A.24) and Equ.(A.31)
!   where P(l,m,n) = i^(m-n) d(l,m,n)
!     This subroutin is partially calibrated with Mishchenko's subroutine
!   Gener()

subroutine gsph3(x,d3, LL,NPL)
real*8 x,d3(NPL,3,9),dlmin,power,fac2,t1,t2,t3
integer l3,m3,n3,m,n,l,lmin,xmn,pow,NPL
do m3=1,3
    m=2*m3-4
    do n3=1,9
        n=n3-5
        if(n-m >= 0) then
            xmn=1
        else
            xmn=pow(-1,m-n)
        end if
        if(abs(m) >= abs(n)) then
            lmin=abs(m)
        else
            lmin=abs(n)
        end if
        dlmin=xmn*power(0.5d0,lmin)
        dlmin=dlmin*dsqrt(fac2(2*lmin)/(fac2(abs(m-n))*fac2(abs(m+n))))
        dlmin=dlmin*dsqrt(power(1.0d0-x,abs(m-n))*(power(1.0d0+x,abs(m+n))))
        do l3=1,LL+1
            l=l3-1
            if((m == 0) .AND. (n == 0)) then
                if (l == 0) then
                    d3(l3,m3,n3)=1.0d0
                else
                    if (l == 1) then
                        d3(l3,m3,n3)=x
```

```
                    else
                        d3(l3,m3,n3)=(real(2*l-1)*x*d3(l3-1,m3,n3)    &
                                      -(l-1)*d3(l3-2,m3,n3))/l
                    end if
                end if
             else
                if (l < lmin) then
                    d3(l3,m3,n3)=0
                else
                    if (l == lmin) then
                        d3(l3,m3,n3)=dlmin
                    else
                        t1=1.0d0/(real(l-1)*dsqrt(1.0d0*(l*l-m*m)*(l*l-n*n)))
                        t2=real(l)*dsqrt(1.0d0*real((l-1)*(l-1)-m*m)        &
                                         *real((l-1)*(l-1)-n*n))
                        t3=real(2*l-1)*real((l-1)*l*x-m*n)
                        d3(l3,m3,n3)=t1*(t3*d3(l3-1,m3,n3)-t2*d3(l3-2,m3,n3))
                    end if
                end if
            end if
          end do   !end_loop_l3
       end do !end_loop_n3
    end do !end_loop_m3
return
end

!pow.r n^m
function pow(n, m)
integer n,m,pow,i
pow=1
if(m == 0) then
    return
else
   do i=1,m
      pow =pow*n
   end do
end if
return
end

!power.r p^m
function power(p, m)
real*8 p,power
integer m,i
power=1.0d0
if(m==0) then
  return
else
  do i=1,m
      power = power*p
  end do
end if
return
end

!factor.r m!
function fac2(m)
real*8 fac2
integer m
fac2=1.0
if(m==0) then
  fac2 = 1.0d0
  return
```

```
else
  do i=1,m
     fac2 = fac2*i
  end do
end if
return
end


!*************************************************************
!      The program computes far-field light scattering by polydisperse
!      homogeneous spherical particles using the Lorenz-Mie theory

!  The original program is based on the book
!  1. Mishchenko, M. I., L. D. Travis, and A. A. Lacis (2002):
!  Scattering, Absorption, and Emission of Light
!  by Small Particles, Cambridge University Press, Cambridge.page 162
!   - page 165
!      The source code has been modified by Ni
!      Input parameters:
!
!   R1 is the radius of the particle
!   LAM - wavelength of the incident light in the surrounding medium
!      REFMED - Refractive index of the surrounding medium
!
!   Important:  LAM, R1
!                 must be in the same units of length (e.g., microns)
!
!   MRR and MRI - real and imaginary parts of the relative refractive
!                   index (MRI must be non-negative)
!
!   DDELT - desired numerical accuracy of computing the scattering
!        matrix elements
!
!  Output information:
!
!   L1 - temporatory not used
!      CEXT and CSCA - average extinction and scattering cross sections
!           per particle
!   F11 = a_1, F33 = a_3, F12 = b_1, and F34 = b_2 - elements of the
!          normalized scattering matrix given by Eq. (4.65) of Ref. 1.
!   PPP is the coefficient of expansion in generalized spherical function
!              coefficients appearing in the expansions
!       of the elements of the normalized scattering matrix in
!       generalized spherical functions [Eqs. (4.75)-(4.80) of Ref. 1].
!      PPP(1)-ALPHA1, PPP(2)-ALPHA2, PPP(3)-ALPHA3, PPP(4)-ALPHA4,
!   PPP(5)-BETA1, PPP(6)-BETA2
!      L1MAX-order of expansion in generalized spherical function
!   Q1 - g factor
      SUBROUTINE SPHER (LAM,REFMED,MRR,MRII,R1,L1,AL1,AL2,AL3,AL4,BET1  &
                        ,BET2,CEXT,CSCA,DDELT,PPP, L1MAX,Q1)
      PARAMETER (NGRAD=1000, NMIE=200, NPL=2*NMIE, NDRDI=3*NMIE)
!Questional change in NGRAD, NMIE
      IMPLICIT REAL*8 (A-H,O-Z)
      REAL*8 LAM,REFMED,MRR,MRI,MRII, R1, DDELT, &
             PSI(NMIE),HI(NDRDI),RPSI(NDRDI),&
             AL1(NPL),AL2(NPL),AL3(NPL),AL4(NPL),BET1(NPL),&
             BET2(NPL),P1(NPL),P2(NPL),P3(NPL),P4(NPL), &
             DR(NDRDI),DI(NDRDI),AR(NMIE),AI(NMIE),BR(NMIE),BI(NMIE),&
             X(NPL),W(NPL),&
             COEFF1(NMIE),COEFF2(NMIE),COEFF3(NMIE),&
             COEF1(NPL),COEF2(NPL),COEF3(NPL),COEF4(NPL),&
             COEF5(NPL),COEF6(NPL),COEF7(NPL),COEF8(NPL), &
```

```
             F11(NPL),F33(NPL),F12(NPL),F34(NPL),&
             PIN(NMIE),TAUN(NMIE)
      REAL*8 PPP(NPL,6) !Add for the use of main program
      Integer L1MAX     !Add for the use of main program
      COMMON /COEFF/ COEFF1, COEFF2, COEFF3
      COMMON /COEF/ COEF1,COEF2,COEF3,COEF4,COEF5,COEF6,COEF7,COEF8,D6
      COMMON /P/ P1,P2,P3,P4
      MRI=-MRII
      PI=3.1415926535897932D0
      WN=2D0*PI*REFMED/LAM
      RX=R1*WN
      M=IDINT(RX+4.05D0*RX**0.33333D0+8D0)
      IF (M.GT.NMIE) PRINT 3335
      IF (M.GT.NMIE) STOP
 3335 FORMAT ('TOO MANY MIE COEFFICIENTS. INCREASE NMIE.')
      DO I=1,M
         DD=DFLOAT(I)
         DD1=DD+1D0
         COEFF1(I)=DD1/DD
         DD2=(2D0*DD+1D0)
         COEFF2(I)=DD2
         COEFF3(I)=0.5D0*DD2/(DD*DD1)
      END DO
      NG=2*M-1
      L1MAX=2*M
      CM=1D0/(MRR*MRR+MRI*MRI)
      RMR=MRR*CM
      RMI=-MRI*CM
      CEXT=0D0
      CSCA=0D0
        CALL GAUSS (NG,0,0,X,W)
      DO I=1,NG
         F11(I)=0D0
         F33(I)=0D0
         F12(I)=0D0
         F34(I)=0D0
      END DO
          Y = R1
          ZW = 1D0
          RXR=MRR*RX
          RXI=MRI*RX
          CDD=RXR*RXR+RXI*RXI
          CD=DSQRT(CDD)
          DC=DCOS(RX)
          DS=DSIN(RX)
          CX=1D0/RX
          CXR=RXR/CDD
          CXI=-RXI/CDD
!  CALCULATION OF THE MIE COEFFICIENTS  ******************************
          M1=IDINT(RX+4.05D0*RX**0.33333D0+8D0)
          M2=M1+2+IDINT(1.2D0*DSQRT(RX))+5
          M3=M2-1
          IF (M2.GT.NDRDI) PRINT 3338
          IF (M2.GT.NDRDI) STOP
 3338     FORMAT ('M2.GT.NDRDI. EXECUTION TERMINATED')
          QMAX=DMAX1(DFLOAT(M1),CD)
          M4=IDINT(6.4D0*QMAX**0.33333D0+QMAX)+8
          IF (M4.GT.NDRDI) PRINT 3337
          IF (M4.GT.NDRDI) STOP
 3337     FORMAT ('M4.GT.NDRDI. EXECUTION TERMINATED')
          D4=DFLOAT(M4+1)
          DR(M4)=D4*CXR
          DI(M4)=D4*CXI
```

```
HI(1)=DS+DC*CX
HI(2)=3.0D0*HI(1)*CX-DC
PSI(1)=CX*DS-DC
RPSI(M2)=RX/DFLOAT(2*M2+1)
DO J=2,M3
    J1=M2-J+1
    RPSI(J1)=1D0/(DFLOAT(2*J1+1)*CX-RPSI(J1+1))
END DO
DO J=2,M4
    J1=M4-J+2
    J2=J1-1
    DJ=DFLOAT(J1)
    FR=DJ*CXR
    FI=DJ*CXI
    OR=DR(J1)+FR
    OI=DI(J1)+FI
    ORI=1D0/(OR*OR+OI*OI)
    DR(J2)=FR-OR*ORI
    DI(J2)=FI+OI*ORI
END DO
M2=M1-1
DO J=2,M2
    J1=J-1
    J2=J+1
    HI(J2)=DFLOAT(2*J+1)*HI(J)*CX-HI(J1)
end do
DO J=2,M1
    PSI(J)=RPSI(J)*PSI(J-1)
end do
PSI1=PSI(1)
DR1=DR(1)
DI1=DI(1)
HI1=HI(1)
OR=DR1*RMR-DI1*RMI+CX
OR1=OR*PSI1-DS
OI=DR1*RMI+DI1*RMR
OI1=OI*PSI1
OR2=OR*PSI1-OI*HI1-DS
OI2=OR*HI1+OI*PSI1-DC
OAB=1D0/(OR2*OR2+OI2*OI2)
AR(1)=(OR1*OR2+OI1*OI2)*OAB
AI(1)=(OR2*OI1-OR1*OI2)*OAB
OR=MRR*DR1-MRI*DI1+CX
OI=MRR*DI1+MRI*DR1
OR1=OR*PSI1-DS
OR2=OR*PSI1-OI*HI1-DS
OI1=OI*PSI1
OI2=OR*HI1+OI*PSI1-DC
OAB=1D0/(OR2*OR2+OI2*OI2)
BR(1)=(OR1*OR2+OI1*OI2)*OAB
BI(1)=(OR2*OI1-OR1*OI2)*OAB
DO J=2,M1
    J1=J-1
    DJ=DFLOAT(J)*CX
    PSI1=PSI(J)
    PSI2=PSI(J1)
    HI1=HI(J)
    HI2=HI(J1)
    DR1=DR(J)
    DI1=DI(J)
    OR=DR1*RMR-DI1*RMI+DJ
    OI=DR1*RMI+DI1*RMR
    OR1=OR*PSI1-PSI2
```

```
                OI1=OI*PSI1
                OR2=OR*PSI1-OI*HI1-PSI2
                OI2=OR*HI1+OI*PSI1-HI2
                OAB=1D0/(OR2*OR2+OI2*OI2)
                YAR=(OR1*OR2+OI1*OI2)*OAB
                YAI=(OR2*OI1-OR1*OI2)*OAB
                AR(J)=YAR
                AI(J)=YAI
                OR=MRR*DR1-MRI*DI1+DJ
                OI=MRR*DI1+MRI*DR1
                OR1=OR*PSI1-PSI2
                OR2=OR*PSI1-OI*HI1-PSI2
                OI1=OI*PSI1
                OI2=OR*HI1+OI*PSI1-HI2
                OAB=1D0/(OR2*OR2+OI2*OI2)
                YBR=(OR1*OR2+OI1*OI2)*OAB
                YBI=(OR2*OI1-OR1*OI2)*OAB
                BR(J)=YBR
                BI(J)=YBI
                YAR=YAR*YAR+YAI*YAI+YBR*YBR+YBI*YBI
            end do

!  END OF COMPUTING THE MIE COEFFICIENTS  *************************

            CE=0D0
            CS=0D0
            DO J=1,M1
                CJ=COEFF2(J)
                ARJ=AR(J)
                AIJ=AI(J)
                BRJ=BR(J)
                BIJ=BI(J)
                CDA=ARJ*ARJ+AIJ*AIJ
                CDB=BRJ*BRJ+BIJ*BIJ
                CE=CE+CJ*(ARJ+BRJ)
                CS=CS+CJ*(CDA+CDB)
                CJ=COEFF3(J)
                AR(J)=CJ*(ARJ+BRJ)
                AI(J)=CJ*(AIJ+BIJ)
                BR(J)=CJ*(ARJ-BRJ)
                BI(J)=CJ*(AIJ-BIJ)
            end do
            CEXT=CE
            CSCA=CS

            DO K=1,NG
                CALL ANGL (M1,X(K),PIN,TAUN)
                SPR=0D0
                SPI=0D0
                SMR=0D0
                SMI=0D0
                DO J=1,M1
                    PJ=PIN(J)
                    TJ=TAUN(J)
                    PP=TJ+PJ
                    PM=TJ-PJ
                    SPR=SPR+AR(J)*PP
                    SPI=SPI+AI(J)*PP
                    SMR=SMR+BR(J)*PM
                    SMI=SMI+BI(J)*PM
                end do
                D1=SPR*SPR+SPI*SPI
                D2=SMR*SMR+SMI*SMI
```

```
              F11(K)=F11(K)+D1+D2
              F33(K)=F33(K)+D1-D2
              F12(K)=F12(K)+(SPR*SMR+SPI*SMI)*2D0
              F34(K)=F34(K)+(SPR*SMI-SPI*SMR)*2D0

           end do
           DD=2D0/CSCA
           DO I=1,NG
              F11(I)=F11(I)*DD
              F12(I)=F12(I)*DD
              F33(I)=F33(I)*DD
              F34(I)=F34(I)*DD
           end do

!  CROSS SECTIONS AND SINGLE SCATTERING ALBEDO  ***************

         VOL=2D0*PI/(WN*WN) !WN is changed by Ni
         CEXT=CEXT*VOL
         CSCA=CSCA*VOL
         ALB=CSCA/CEXT

!  CALCULATION OF THE EXPANSION COEFFICIENTS  *******************

      DO L1=3,L1MAX
          L=L1-1
          COEF1(L1)=1D0/DFLOAT(L+1)
          COEF2(L1)=DFLOAT(2*L+1)
          COEF3(L1)=1D0/DSQRT(DFLOAT((L+1)*(L+1)-4))
          COEF4(L1)=DSQRT(DFLOAT(L*L-4))
          COEF5(L1)=1D0/(DFLOAT(L)*DFLOAT((L+1)*(L+1)-4))
          COEF6(L1)=DFLOAT(2*L+1)*DFLOAT(L*(L+1))
          COEF7(L1)=DFLOAT((2*L+1)*4)
          COEF8(L1)=DFLOAT(L+1)*DFLOAT(L*L-4)
      end do
      DO L1=1,L1MAX
          AL1(L1)=0D0
          AL2(L1)=0D0
          AL3(L1)=0D0
          AL4(L1)=0D0
          BET1(L1)=0D0
          BET2(L1)=0D0
      end do
      D6=0.25D0*DSQRT(6D0)

      DO I=1,NG
          CALL GENER (X(I),L1MAX)
          WI=W(I)
          FF11=F11(I)*WI
          FF33=F33(I)*WI
          FF12=F12(I)*WI
          FF34=F34(I)*WI
          FP=FF11+FF33
          FM=FF11-FF33
          DO L1=1,L1MAX
              P1L1=P1(L1)
              P4L1=P4(L1)
              AL1(L1)=AL1(L1)+FF11*P1L1
              AL4(L1)=AL4(L1)+FF33*P1L1
              AL2(L1)=AL2(L1)+FP*P2(L1)
              AL3(L1)=AL3(L1)+FM*P3(L1)
              BET1(L1)=BET1(L1)+FF12*P4L1
              BET2(L1)=BET2(L1)+FF34*P4L1
          end do
```

```
      end do

      DO L1=1,L1MAX
          CL=DFLOAT(L1-1)+0.5D0
          L=L1
!   Questinable, the formula is different as W.A.de Rooij's equ.(54)-(59)
!   coefficient are compared with table (4) in W. A. Rooij, etc.,
!                  Astron. Astrophys. 131, 237-248 (1984)
          AL1(L1)=AL1(L1)*CL
          A2=AL2(L1)*CL*0.5D0
          A3=AL3(L1)*CL*0.5D0
          AL2(L1)=A2+A3
          AL3(L1)=A2-A3
          AL4(L1)=AL4(L1)*CL
          BET1(L1)=BET1(L1)*CL
               !Questionable, following Equ.(4.85) in Michael's book,
               !it should be BET1(L1) = -BET2(L1)*CL
          BET2(L1)=-BET2(L1)*CL
          PPP(L1,1) = (AL2(L1)+AL3(L1))*0.5D0
          PPP(L1,2) = (AL1(L1 )+AL4(L1))*0.5D0
          PPP(L1,3) = (AL2(L1)-AL3(L1))*0.5D0
          PPP(L1,4) = (AL1(L1)-AL4(L1))*0.5D0
          PPP(L1,5) = BET1(L1)*0.5D0
          PPP(L1,6) = BET2(L1)*0.5D0
          IF (DABS(AL1(L1)).LE.DDELT) GO TO 400
      end do
  400 L1MAX=L
      Q1=AL1(2)/3D0
      PRINT 511,Q1,CSCA,CEXT
  511 FORMAT('Q1,Csca, Cext =',3d12.6)
      RETURN
      END

      SUBROUTINE GAUSS ( N,IND1,IND2,Z,W )
      IMPLICIT REAL*8 (A-H,P-Z)
      REAL*8 Z(N),W(N)
      DATA A,B,C /1D0,2D0,3D0/
      IND=MOD(N,2)
      K=N/2+IND
      F=DFLOAT(N)
      DO 100 I=1,K
          M=N+1-I
          IF(I.EQ.1) X=A-B/((F+A)*F)
          IF(I.EQ.2) X=(Z(N)-A)*4D0+Z(N)
          IF(I.EQ.3) X=(Z(N-1)-Z(N))*1.6D0+Z(N-1)
          IF(I.GT.3) X=(Z(M+1)-Z(M+2))*C+Z(M+3)
          IF(I.EQ.K.AND.IND.EQ.1) X=0D0
          NITER=0
          CHECK=1D-16
   10     PB=1D0
          NITER=NITER+1
          IF (NITER.LE.100) GO TO 15
          CHECK=CHECK*10D0
   15     PC=X
          DJ=A
          DO 20 J=2,N
              DJ=DJ+A
              PA=PB
              PB=PC
   20         PC=X*PB+(X*PB-PA)*(DJ-A)/DJ
          PA=A/((PB-X*PC)*F)
          PB=PA*PC*(A-X*X)
          X=X-PB
```

```
          IF(DABS(PB).GT.check*DABS(X)) GO TO 10
          Z(M)=X
          W(M)=PA*PA*(A-X*X)
          IF(IND1.EQ.0) W(M)=B*W(M)
          IF(I.EQ.K.AND.IND.EQ.1) GO TO 100
          Z(I)=-Z(M)
          W(I)=W(M)
  !questionable
  100 CONTINUE
  !100 END DO
       IF(IND2.NE.1) GO TO 110
       PRINT 1100,N
 1100 FORMAT(' ***  POINTS AND WEIGHTS OF GAUSSIAN QUADRATURE FORMULA',&
       ' OF ',I4,'-TH ORDER')
       DO I=1,K
           ZZ=-Z(I)
       END DO
       GO TO 115
  110 CONTINUE
      PRINT 1300,N
 1300 FORMAT(' GAUSSIAN QUADRATURE FORMULA OF ',I4,'-TH ORDER IS USED')
  115 CONTINUE
       IF(IND1.EQ.0) GO TO 140
       DO 120 I=1,N
  120     Z(I)=(A+Z(I))/B
  140 CONTINUE

       RETURN
       END


!**********************************************************************

!  CALCULATION OF THE GENERALIZED SPHERICAL FUNCTIONS Pmnl
!P1 --- P0,0, P2 --- P2,2, P3 --- P2,-2, P4 --- P0,2

       SUBROUTINE GENER (U,L1MAX)
       PARAMETER (NMIE=200, NPL=2*NMIE)
       IMPLICIT REAL*8 (A-H,O-Z)
       REAL*8 P1(NPL),P2(NPL),P3(NPL),P4(NPL),&
             COEF1(NPL),COEF2(NPL),COEF3(NPL),COEF4(NPL),&
             COEF5(NPL),COEF6(NPL),COEF7(NPL),COEF8(NPL)
       COMMON /COEF/ COEF1,COEF2,COEF3,COEF4,COEF5,COEF6,COEF7,COEF8,D6
       COMMON /P/ P1,P2,P3,P4
       DUP=1D0+U
       DUM=1D0-U
       DU=U*U
       P1(1)=1D0
       P1(2)=U
       P1(3)=0.5D0*(3D0*DU-1D0)
       P2(1)=0D0
       P2(2)=0D0
       P2(3)=0.25D0*DUP*DUP
       P3(1)=0D0
       P3(2)=0D0
       P3(3)=0.25D0*DUM*DUM
       P4(1)=0D0
       P4(2)=0D0
       P4(3)=D6*(DU-1D0)
       LMAX=L1MAX-1
       DO L1=3,LMAX
          C1=COEF1(L1)
          C2=COEF2(L1)
```

```
         C3=COEF3(L1)
         C4=COEF4(L1)
         C5=COEF5(L1)
         C6=COEF6(L1)
         C7=COEF7(L1)
         C8=COEF8(L1)
         CU1=C2*U
         CU2=C6*U
         L2=L1+1
         L3=L1-1
         DL=DFLOAT(L3)
         P1(L2)=C1*(CU1*P1(L1)-DL*P1(L3))
         P2(L2)=C5*((CU2-C7)*P2(L1)-C8*P2(L3))
         P3(L2)=C5*((CU2+C7)*P3(L1)-C8*P3(L3))
         P4(L2)=C3*(CU1*P4(L1)-C4*P4(L3))
      END DO
      RETURN
      END

!*********************************************************************

!   CALCULATION OF THE ANGULAR FUNCTIONS PI(N) AND TAU(N) FOR
!   GIVEN ARGUMENT U=COS(THETA)
!   N.LE.NMAX

      SUBROUTINE ANGL (NMAX,U,PIN,TAUN)
      PARAMETER (NMIE=200)
      IMPLICIT REAL*8 (A-H,O-Z)
      REAL*8 PIN(NMAX),TAUN(NMAX),COEFF1(NMIE),COEFF2(NMIE), COEFF3(NMIE)
      COMMON /COEFF/ COEFF1, COEFF2, COEFF3
      !    COMMON /COEFF/ COEFF1
      !modified by Ni for avoid the inconsistent definition
      P1=0D0
      P2=1D0
      do N=1,NMAX
        S=U*P2
        T=S-P1
        TAUN(N)=DFLOAT(N)*T-P1
        PIN(N)=P2
        P1=P2
        P2=S+COEFF1(N)*T
      end do
      RETURN
      END

!Program calculating Clebsch-Gordan coefficients [Equ.(A.20)]
!Consistant with the result from website
!http://www.gostick.co.uk/cleb/cgjava.html
 Real*8 function CCG(N,N1,M,M1,NN,MM)
      IMPLICIT REAL*8 (A-H,O-Z)
      REAL*8 temp,sign
      INTEGER N,N1,M,M1,NN,MM
      IF((NN .GT. (N+N1)) .OR. (NN .LT. IABS(N-N1)) &
         .OR. (MM .NE. (M+M1)) &
         .OR. (IABS(M) .GT. N) &
         .OR. (IABS(M1) .GT. N1) &
         .OR. (IABS(MM) .GT. NN) &
         .OR. ((M+N) .LT. 0) &
         .OR. ((M1+N1) .LT. 0) &
         .OR. ((NN+MM) .LT. 0) &
         .OR. ((N+N1+NN) .LT. 0)) Then
!        PRINT 5001
!        STOP
```

```
!    5001 FORMAT(' ERROR IN SUBROUTINE CCG')
       CCG = 0.0D0
       return
     else
       if(M1==-1) then
           if((NN-N)==1) then
               sign=1
               temp=dfloat((NN-M)*(NN-M+1))/dfloat((2*NN-1)*2*NN)
           else
               if((NN-N)==0) then
                   sign=1
                   temp=dfloat((NN+M)*(NN-M+1))/dfloat((NN+1)*2*NN)
               else
                   sign=1
                   temp=dfloat((NN+M)*(NN+M+1))/dfloat((2*NN+2)*(2*NN+3))
                end if
           end if
       else
           if(M1==0) then
               if((NN-N)==1) then
                   sign=1
                   temp=dfloat((NN-M)*(NN+M))/dfloat((2*NN-1)*NN)
                else
                   if((NN-N)==0) then
                       sign=M
                       temp=1./dfloat((NN+1)*NN)
                   else
                       sign=-1
                       temp=dfloat((NN+M+1)*(NN-M+1))/dfloat((NN+1)*(2*NN+3))
                   end if
                end if
            else
               if((NN-N)==1) then
                   sign=1
                   temp=dfloat((NN+M)*(NN+M+1))/dfloat((2*NN-1)*2*NN)
               else
                   if((NN-N)==0) then
                       sign=-1
                       temp=dfloat((NN-M)*(NN+M+1))/dfloat((NN+1)*2*NN)
                   else
                       sign=1
                       temp=dfloat((NN-M)*(NN-M+1))/dfloat((2*NN+2)*(2*NN+3))
                   end if
               end if
           end if
        end if
      end if
      CCG=sign*dsqrt(temp)
      END function


!   eigen
!   calculate pii after Equ. (A.7), eigen-value lambda Equ. (A.10)
!   and eigen-vector bb, in Appendix A
!   Input:
!   mus        the scattering coefficient
!   ppp(LL,6)   the generalized spherical expension of phase function
!   ppp(1)->ppp(2,2), ppp(2)->ppp(0,0), ppp(3)->ppp(2,-2), ppp(4)->ppp(0,-0)
!   ppp(5)->Re[ppp(2,0)]  ppp(6)->Im[ppp(2,0)]
!   |ppp(1)          ppp(5)+i*ppp(6)    ppp(5)-i*ppp(6)   ppp(3)         |
!   |ppp(5)+i*ppp(6) ppp(2)             ppp(4)            ppp(5)-i*ppp(6)|
!   |ppp(5)-i*ppp(6) ppp(4)             ppp(2)            ppp(5)+i*ppp(6)|
!   |ppp(3)          ppp(5)-i*ppp(6)    ppp(5)+i*ppp(6)   ppp(1)         |
```

```
!
!   output:
!   Pii(LL,4,4) m4,n4=1,2,3,4  for m,n=2,0,-0,-2
!   lambda(LL,4)  i=1,2,3,4
!   bb(LL,4,4,4), where (4,4,4) for i,m4,n0
subroutine eigen(mus,ppp,lambda,bb,L1MAX)
implicit integer (a-z)
    INTEGER           LDA, LDB, M, N, NRHS, LDAA,LDBB,MM,NN,NRHSS
    PARAMETER        (M = 16)
    PARAMETER        (N = 16)
    PARAMETER        (NRHS = 1)
    PARAMETER        (LDA = M)
    PARAMETER        (LDB = LDA)
    PARAMETER        (MM = 4)
    PARAMETER        (NN = 4)
    PARAMETER        (NRHSS = 1)
    PARAMETER        (LDAA = MM)
    PARAMETER        (LDBB = LDAA)
PARAMETER (NMIE=200, NPL=2*NMIE)
real*8 mus,ppp(NPL,6),pip(NPL,6),tt1,tt2,tt3,tt4
real*8
ar(16,16),ai(16,16),br(16),bi(16),cr(16),ci(16),ar0(4,4),ai0(4,4),br0(4), &
       bi0(4),cr0(4),ci0(4)   !ar0,ai0,br0,bi0,cr0,ci0 represent l = 0,1 case
complex*16 pii(NPL,4,4),lambda(NPL,4),bb(NPL,4,4,4),a(16,16),a0(4,4)
integer l,m4,n4,n0,i,j,LL
complex*16  A1(LDA,N), B1(LDB,NRHS), AA1(LDAA,NN),BB1(LDBB,NRHSS)
INTEGER           INFO, IROW, IPIVOT(N)
INTEGER           INFOO, IROWW, IPIVOTT(N)
EXTERNAL          ZGESV
LL = L1MAX
do l=1,LL
   pip(l,1)=mus*(1.0d0-ppp(l,1)/real(2*l-1))   !II(2,2)
   pii(l,1,1)=dcmplx(pip(l,1),0)
   pii(l,4,4)=pii(l,1,1)
   pip(l,2)=mus*(1.0d0-ppp(l,2)/real(2*l-1))   !II(0,0)
   pii(l,2,2)=dcmplx(pip(l,2),0)
   pii(l,3,3)=pii(l,2,2)
   pip(l,3)=-mus*ppp(l,3)/real(2*l-1)          !II(2,-2)
   pii(l,1,4)=dcmplx(pip(l,3),0)
   pii(l,4,1)=pii(l,1,4)
   pip(l,4)=-mus*ppp(l,4)/real(2*l-1)          !II(0,-0)
   pii(l,2,3)=dcmplx(pip(l,4),0)
   pii(l,3,2)=pii(l,2,3)
   pip(l,5)=-mus*ppp(l,5)/real(2*l-1)          !ReII(2,0)
   pip(l,6)=-mus*ppp(l,6)/real(2*l-1)          !ImII(2,0)
   pii(l,1,2)=dcmplx(pip(l,5),pip(l,6))
   pii(l,2,1)=pii(l,1,2)
   pii(l,3,4)=pii(l,1,2)
   pii(l,4,3)=pii(l,1,2)
   pii(l,1,3)=dcmplx(pip(l,5), -pip(l,6))
   pii(l,3,1)=pii(l,1,3)
   pii(l,2,4)=pii(l,1,3)
   pii(l,4,2)=pii(l,1,3)
end do  !end l_loop

! calculate the eigen value lambda(LL,4)
! l = 1,2 is special since the the 4 X 4 degenerate to 2 X 2 matrix and we need
! to gurantee the lambda(l,2) and lambda(l,4)
! is what we need for the following calculation
do l=1,2
    tt1=pip(l,2)+pip(l,1)+pip(l,4)         !II(0,0)+II(2,2)+II(0,-0)
    tt2=pip(l,2)+pip(l,1)-pip(l,4)         !II(0,0)+II(2,2)-II(0,-0)
    tt3=pip(l,2)-pip(l,1)+pip(l,4)         !II(0,0)-II(2,2)+II(0,-0)
```

```
    tt4=pip(l,2)-pip(l,1)-pip(l,4)         !II(0,0)-II(2,2)-II(0,-0)
    lambda(l,1)=dcmplx(0.5d0*(tt1-tt3),0)  ! Lamda(1) = mus
    lambda(l,2)=dcmplx(0.5d0*(tt1+tt3),0)  ! Lamda(2) = II(0,0)+II(0,-0)
    lambda(l,3)=dcmplx(0.5d0*(tt2-tt4),0)  ! Lamda(3) = mus
    lambda(l,4)=dcmplx(0.5d0*(tt2+tt4),0)  ! Lamda(4) = II(0,0)-II(0,-0)
end do  !end l_loop
do l=3,LL           !Calculate of eigenvalues according Eq.(16)

   tt1=pip(l,2)+pip(l,1)+pip(l,4)+pip(l,3)
   tt2=pip(l,2)+pip(l,1)-pip(l,4)-pip(l,3)
   tt3=(pip(l,2)-pip(l,1)+pip(l,4)-pip(l,3))**2+16*pip(l,5)**2
   tt4=(pip(l,2)-pip(l,1)-pip(l,4)+pip(l,3))**2-16*pip(l,6)**2
   if(tt3 >= 0.0d0) then
     tt3=dsqrt(tt3)
     lambda(l,1)=dcmplx(0.5d0*(tt1+tt3),0)
     lambda(l,2)=dcmplx(0.5d0*(tt1-tt3),0)
   else
     tt3=dsqrt(-tt3)
     lambda(l,1)=dcmplx(0.5d0*tt1, 0.5d0*tt3)
     lambda(l,2)=dcmplx(0.5d0*tt1,-0.5d0*tt3)
   end if
   if(tt4 >= 0.0d0) then
     tt4=dsqrt(tt4)
     lambda(l,3)=dcmplx(0.5d0*(tt2+tt4),0)
     lambda(l,4)=dcmplx(0.5d0*(tt2-tt4),0)
   else
     tt4=dsqrt(-tt4)
     lambda(l,3)=dcmplx(0.5*tt2, 0.5*tt4)
     lambda(l,4)=dcmplx(0.5*tt2,-0.5*tt4)
   end if
end do  !end l_loop
do l=1,2
 do n0=1,4
  do i=1,2
   do m4=1,2
    do j=1,2
     do n4=1,2
      if(i==j) then
        a0((i-1)*2+m4,(j-1)*2+n4)=pii(l,m4+1,n4+1)
        if(m4==n4) then
            a0((i-1)*2+m4,(j-1)*2+n4)=a0((i-1)*2+m4,(j-1)*2+n4)-lambda(l,i*2)
        end if
      else
         a0((i-1)*2+m4,(j-1)*2+n4)=dcmplx(0.0d0, 0.0d0)
      end if
      if(m4==n4)  then
        a0((i-1)*2+m4,(j-1)*2+n4)=a0((i-1)*2+m4,(j-1)*2+n4)+dcmplx(1.0d0,0.0d0)
      end if
     end do !end n4_loop
    end do ! j_loop
    if((m4+1)==n0) then
        cr0((i-1)*2+m4)=1.0d0
    else
        cr0((i-1)*2+m4)=0.0d0
    end if
   end do    !end m4_loop
  end do     !end i_loop
  do i=1,4
   ci0(i)=0.0d0
   do j=1,4
    AA1(i,j) = a0(i,j)
   end do
   BB1(i,NRHSS)=dcmplx(cr0(i),ci0(i))
```

```
  end do
 CALL ZGESV (NN, NRHSS, AA1, LDAA, IPIVOTT, BB1, LDBB, INFOO)
    do i=1,4
        do m4=1,4
           bb(l,i,m4,n0)=dcmplx(0.0d0,0.0d0)
        end do
    end do
    do i=1,2
        do m4=1,2
            bb(l,i*2,m4+1,n0) = BB1((i-1)*2+m4,1);
        end do
    end do
  end do !end n0_loop
end do  !end l_loop

! calculate the eigenvectors bb(LL,4,4,4)
!{{[II(m4,n4)-
Lambda(i)*Delta(m4,n4)]*Delta(i,j)+Delta(n4,i)}*B(n4xi)}\n0=Delta(m4,n0)
!(4x4)x(4x4) matrix
do l=3,LL        !exclude l = 0, 1
 do n0=1,4
  do i=1,4
   do m4=1,4
    do j=1,4
     do n4=1,4
      if(i==j) then
        a((i-1)*4+m4,(j-1)*4+n4)=pii(l,m4,n4)
        if(m4==n4) then
            a((i-1)*4+m4,(j-1)*4+n4)=a((i-1)*4+m4,(j-1)*4+n4)-lambda(l,i)
        end if
      else
         a((i-1)*4+m4,(j-1)*4+n4)=dcmplx(0, 0)
      end if
      if(m4==n4)  then
         a((i-1)*4+m4,(j-1)*4+n4)=a((i-1)*4+m4,(j-1)*4+n4)+dcmplx(1,0)
      end if
     end do !end n4_loop
    end do ! j_loop
   if(m4==n0) then
     cr((i-1)*4+m4)=1
   else
     cr((i-1)*4+m4)=0
   end if
   end do    !end m4_loop
  end do     !end i_loop
  do i=1,16
   ci(i)=0
  end do
   do i = 1,16
    do j = 1,16
      A1(i,j) = a(i,j)
    end do
    B1(i,1) = dcmplx(cr(i),ci(i))
  end do
  CALL ZGESV (N, NRHS, A1, LDA, IPIVOT, B1, LDB, INFO)
   do i=1,4
    do m4=1,4
       bb(l,i,m4,n0) = B1((i-1)*4+m4,1);
    end do
   end do
   end do !end n0_loop
 end do  !end l_loop
 return
```

```
 end

! dclinq.r
subroutine dclinq (n,ar,ai,br,bi,xr,xi)
!
! solution of a set of complex linear equations
!
!  method - qr decomposition of a by householder transformations
!           followed by back substitution
!
!  input
!
!    n    - the number of equations
!    ar   - the real part of the matrix
!    ai   - the imaginary part of the matrix
!    br   - the real part of the right-hand sides
!    bi   - the imaginary part of the right-hand sides
!
!  output
!
!    ar   - both the real and imaginary parts of the
!    ai   - matrix have been clobbered.
!    br   - both the real and imaginary parts of the
!    bi   - matrix have been clobbered.
!    xr   - the real part of the solution vectors
!    xi   - the imaginary part of the solution vectors
!
!  method - qr decomposition of a by householder transformations.
!
double precision ar(n,n),br(n),xr(n)
double precision ai(n,n),bi(n),xi(n)
double precision d(n)
integer n
call dcl2sd(n,ar,ai,d)
call dcl2ss(n,ar,ai,br,bi,d,xr,xi)
return
end

subroutine dcl2sd(n,ar,ai,d)
!
!  to obtain the q*u decomposition of a complex matrix a.
!
!  method - householder transformations.
!
!  input
!
!    n    - the number of equation
!    ar   - the real part of the matrix a.
!    ai   - the imaginary part of the matrix a.
!
!  output
!
!    ar   - the real part of the decomposed matrix a.
!    ai   - the imaginary part of the decomposed matrix a.
!           let v(j)(i)=0      for i=1,...,j-1
!           and v(j)(i)=a(i,j) for i=j,...,m, then
!
!           q = product(j=1,...,n)(i-beta(j)*v(j)*v(j)-transpose)
!
!           where beta(j)=1/(d(j)*abs(a(j,j)))
!           a(i,j) for i.lt.j gives the off-diagonal elements of u.
!    d    - the diagonal entries of u are given by
!           u(i,i)=-d(i)*a(i,i)/cabs(a(i,i)), for i=1,...,n.
```

```
!
double precision ar(n,n),ai(n,n),d(n)
double precision qr,qi,z,w,dsqrt
integer l,i,j,lp1,n
do l=1,n
 z=0.d0
 do i=l,n
   z=z+ar(i,l)**2+ai(i,l)**2
 end do
 z=dsqrt(z)
 d(l)=z
 w=dsqrt(ar(l,l)**2+ai(l,l)**2)
 if(w==0.d0) then
    qr=1.d0
    qi=0.d0
 else
    qr=ar(l,l)/w
    qi=ai(l,l)/w
 end if
 ar(l,l)=qr*(z+w)
 ai(l,l)=qi*(z+w)
 if (l < n) then
   lp1=l+1
   do j=lp1,n
      qr=0.d0
      qi=0.d0
      do  i=l,n
          qr=qr+ar(i,l)*ar(i,j)+ai(i,l)*ai(i,j)
          qi=qi+ar(i,l)*ai(i,j)-ai(i,l)*ar(i,j)
         end do
      qr=qr/(z*(z+w))
      qi=qi/(z*(z+w))
      do i=l,n
         ar(i,j)=ar(i,j)-qr*ar(i,l)+qi*ai(i,l)
         ai(i,j)=ai(i,j)-qr*ai(i,l)-qi*ar(i,l)
     end do
    end do  !end j_loop
  end if   ! end_if
end do   !end l_loop
return
end

subroutine dcl2ss(n,ar,ai,br,bi,d,xr,xi)
!  least squares solution of the complex linear system of algebraic
!  equations a*x=b, where a has been factored by a call to dcl2sd.
!
!  input
!
!    n    - the number of equations.
!    ar   - the real part of the decomposed matrix a.
!    ai   - the imaginary part of the decomposed matrix a.
!    br   - the real part of vector b.
!    bi   - the imaginary part of vector b.
!    d    - as given by dcl2sd.
!
!  output
!
!    br   - both br and bi have been clobbered.
!           sqrt(sum(i=n+1,m)(br(i)**2+bi(i)**2)) is the
!    bi   - l2 norm of the residual in the solution of the equations.
!    xr   - the real part of the solution vector x.
!    xi   - the imaginary part of the solution vector x.
!           x=b is ok.
```

```
double precision ar(n,n),ai(n,n),br(n),bi(n),xr(n),xi(n),d(n)
double precision z,zpw,qr,qi,dsqrt
integer l,i,ii,j,ip1,n
! ... apply q-star to the right-hand-side b.
do l=1,n
 z=d(l)
 zpw=dsqrt(ar(l,l)**2+ai(l,l)**2)
 qr=0.d0
 qi=0.d0
 do i=l,n
    qr=qr+ar(i,l)*br(i)+ai(i,l)*bi(i)
    qi=qi+ar(i,l)*bi(i)-ai(i,l)*br(i)
 end do
 qr=qr/(z*zpw)
 qi=qi/(z*zpw)
 do i=l,n
   br(i)=br(i)-qr*ar(i,l)+qi*ai(i,l)
   bi(i)=bi(i)-qr*ai(i,l)-qi*ar(i,l)
 end do
 xr(l)=br(l)
 xi(l)=bi(l)
 end do  !end l_loop
! ... back-solve the upper-triangular system u*x=(q-star)*b.
do ii=1,n
  i=n+1-ii
  zpw=dsqrt(ar(i,i)**2+ai(i,i)**2)
  qr=xr(i)
  qi=xi(i)
  ip1=i+1
  if(ip1 <= n) then
    do j=ip1,n
       qr=qr-ar(i,j)*xr(j)+ai(i,j)*xi(j)
       qi=qi-ar(i,j)*xi(j)-ai(i,j)*xr(j)
    end do
   end if !end_if
  xr(i)=-( qr*ar(i,i)+qi*ai(i,i))/(zpw*d(i))
  xi(i)=-(-qr*ai(i,i)+qi*ar(i,i))/(zpw*d(i))
  end do
return
end

!  Inverse OF A 3x3 COMPLEX MATRIX
!
!  SYMBOLS:
!  -------
!
!  AR: real part of the input matrix
!  AI: imaginary part of the input matrix
!  BR:       real part of the output matrix
!  BI:  imaging of the output matrix

subroutine inverse_33c(AR,AI,BC,DetR,DetI)
implicit none
real*8 AR(3,3),AI(3,3),BR(3,3),BI(3,3),DetR,DetI,Det,CR,CI
complex*16 BC(3,3)
Integer i,j
call Det_33c(AR,AI,DetR,DetI)
Det = DetR**2+DetI**2
BR(1,1) = AR(2,2)*AR(3,3)-AI(2,2)*AI(3,3)-AR(3,2)*AR(2,3)+AI(3,2)*AI(2,3)
BI(1,1)      = AR(2,2)*AI(3,3)+AI(2,2)*AR(3,3)-AR(3,2)*AI(2,3)-AI(3,2)*AR(2,3)
BR(1,2) = -(AR(1,2)*AR(3,3)-AI(1,2)*AI(3,3)-AR(1,3)*AR(3,2)+AI(1,3)*AI(3,2))
BI(1,2) = -(AR(1,2)*AI(3,3)+AI(1,2)*AR(3,3)-AR(1,3)*AI(3,2)-AI(1,3)*AR(3,2))
BR(1,3) = AR(1,2)*AR(2,3)-AI(1,2)*AI(2,3)-AR(1,3)*AR(2,2)+AI(1,3)*AI(2,2)
```

```
BI(1,3) = AR(1,2)*AI(2,3)+AI(1,2)*AR(2,3)-AR(1,3)*AI(2,2)-AI(1,3)*AR(2,2)
BR(2,1) = -(AR(2,1)*AR(3,3)-AI(2,1)*AI(3,3)-AR(2,3)*AR(3,1)+AI(2,3)*AI(3,1))
BI(2,1) = -(AR(2,1)*AI(3,3)+AI(2,1)*AR(3,3)-AR(2,3)*AI(3,1)-AI(2,3)*AR(3,1))
BR(2,2) = AR(1,1)*AR(3,3)-AI(1,1)*AI(3,3)-AR(1,3)*AR(3,1)+AI(1,3)*AI(3,1)
BI(2,2) = AR(1,1)*AI(3,3)+AI(1,1)*AR(3,3)-AR(1,3)*AI(3,1)-AI(1,3)*AR(3,1)
BR(2,3) = -(AR(1,1)*AR(2,3)-AI(1,1)*AI(2,3)-AR(1,3)*AR(2,1)+AI(1,3)*AI(2,1))
BI(2,3) = -(AR(1,1)*AI(2,3)+AI(1,1)*AR(2,3)-AR(1,3)*AI(2,1)-AI(1,3)*AR(2,1))
BR(3,1) = AR(2,1)*AR(3,2)-AI(2,1)*AI(3,2)-AR(2,2)*AR(3,1)+AI(2,2)*AI(3,1)
BI(3,1) = AR(2,1)*AI(3,2)+AI(2,1)*AR(3,2)-AR(2,2)*AI(3,1)-AI(2,2)*AR(3,1)
BR(3,2) = -(AR(1,1)*AR(3,2)-AI(1,1)*AI(3,2)-AR(1,2)*AR(3,1)+AI(1,2)*AI(3,1))
BI(3,2) = -(AR(1,1)*AI(3,2)+AI(1,1)*AR(3,2)-AR(1,2)*AI(3,1)-AI(1,2)*AR(3,1))
BR(3,3) = AR(1,1)*AR(2,2)-AI(1,1)*AI(2,2)-AR(1,2)*AR(2,1)+AI(1,2)*AI(2,1)
BI(3,3) = AR(1,1)*AI(2,2)+AI(1,1)*AR(2,2)-AR(1,2)*AI(2,1)-AI(1,2)*AR(2,1)
do i=1,3
    do j=1,3
    !   if (dsqrt((Det)) > 1.0e-13) then
            cr = (BR(i,j)*DetR+BI(i,j)*DetI)/Det
            ci = (BI(i,j)*DetR-BR(i,j)*DetI)/Det
            BC(i,j)= dcmplx(cr,ci)
    !   else
    !      BC(i,j) = dcmplx(0.0d0,0.0d0)
    !   end if
    end do
end do
end

!  DETERMINANT OF A 3x3 COMPLEX MATRIX
!
!  SYMBOLS:
!  -------
!
!  AR: real part of the matrix
!  AI: imaginary part of the matrix
!
!  DetR:  real part of the determinant
!  DetI:  imaginary part of the determinant

!Implicit Double Precision (A-H,O-Z)
!DIMENSION AR(3,3),AI(3,3)
!example
!(1.0,0.0), (1.0,2.0), (2.0,10.0)
!(1.0,1.0), (0.0,3.0), (-5.0,14.0)
!(1.0,1.0),  (0.0,5.0),(-8.0,20.0)
! Result (1.0, 0.0)

subroutine Det_33c(AR,AI,DetR,DetI)
Implicit real*8 (A-H,O-Z)
real*8 AR(3,3),AI(3,3)
      SMR1 = AR(2,2)*AR(3,3)-AI(2,2)*AI(3,3)
      SMI1 = AR(2,2)*AI(3,3)+AI(2,2)*AR(3,3)
      SMR2 = AR(2,3)*AR(3,2)-AI(2,3)*AI(3,2)
      SMI2 = AR(2,3)*AI(3,2)+AI(2,3)*AR(3,2)
      SMR  = SMR1-SMR2
      SMI  = SMI1-SMI2
      DTR1 = AR(1,1)*SMR - AI(1,1)*SMI
      DTI1 = AR(1,1)*SMI + AI(1,1)*SMR
      SMR1 = AR(2,1)*AR(3,3)-AI(2,1)*AI(3,3)
      SMI1 = AR(2,1)*AI(3,3)+AI(2,1)*AR(3,3)
      SMR2 = AR(2,3)*AR(3,1)-AI(2,3)*AI(3,1)
      SMI2 = AR(2,3)*AI(3,1)+AI(2,3)*AR(3,1)
      SMR  = SMR1-SMR2
      SMI  = SMI1-SMI2
      DTR2 = AR(1,2)*SMR - AI(1,2)*SMI
```

```
      DTI2 = AR(1,2)*SMI + AI(1,2)*SMR
      SMR1 = AR(2,1)*AR(3,2)-AI(2,1)*AI(3,2)
      SMI1 = AR(2,1)*AI(3,2)+AI(2,1)*AR(3,2)
      SMR2 = AR(2,2)*AR(3,1)-AI(2,2)*AI(3,1)
      SMI2 = AR(2,2)*AI(3,1)+AI(2,2)*AR(3,1)
      SMR  = SMR1-SMR2
      SMI  = SMI1-SMI2
      DTR3 = AR(1,3)*SMR - AI(1,3)*SMI
      DTI3 = AR(1,3)*SMI + AI(1,3)*SMR
      DetR = DTR1-DTR2+DTR3
      DetI = DTI1-DTI2+DTI3
Return
End
```

Appendix C

PATENTS

1. R. R. Alfano and **X. Ni**, "Methods to improve backscattering imaging through large particle suspensions using circular polarization memory," U.S. Patent Application Serial No. #60/675,479 (Provisional patent application)
2. R. R. Alfano, and **X. Ni**, "Changing skin-color using quantum and optical principles in cosmetic preparations" (Provisional patent application) Filed on Jan. 19, 2006

LIST OF PUBLICATIONS

1. R. R. Alfano, J. L. Birman, **X. Ni**, M. Alrubaiee, and B. B. Das, "Comment on: observation of optical precursors in water," Phys. Rev. Lett. **94**, 239401 (2005).

2. S. A. Kartazayeva, **X. Ni**, and R. R. Alfano, "Backscattering target detection in a turbid medium by use of circularly and linearly polarized light," Opt. Lett. **30**, 1168 (2005).
3. **X. Ni**, X. Xing, W. Cai, and R. R. Alfano, "Time-resolved polarization to extract coded information from early ballistic and snake signal through turbid media," Opt. Lett**. 28,** 343 (2003).
4. **X. Ni**, Q. R. Xing, W. Cai, and R. R. Alfano, "Wireless propagation of optical coded pulse streams through turbid media," Wave scattering in complex media: from theory to applications, edited by Bart van Tiggelen and Sergey Skipetrov (Kluwer Academic Publishers), 607 (2003).

5. **X. Ni**, and R. R. Alfano, “Free-space laser optical communication using pulse-coded data stream,” Appl. Opt. **42**, 6980 (2003).
6. **X. Ni**, and R. R. Alfano, “ Time-resolved backscattering of circularly and linearly polarized light in turbid media,” Opt. Lett. **29**, 2773 (2004).
7. **X. Ni**, C. Wang, X. Liang, M. Al-Rubaiee and R. R. Alfano, “Fresnel diffraction supercontinuum generation,” IEEE *JSTQE* **10**, 1229 (2004).

MANUSCRIPTS SUBMITTED

1. W. Cai, **X. Ni**, and R. R. Alfano, “Backscattering of polarized light from turbid media using an analytical cumultant solution of the vector radiative transfer equation,” Phys. Rev. E (Submitted).
2. **X. Ni** and R. R. Alfano, “Brillouin precursors propagation in the THz region in Lorentz media,” Optics Express (Submitted).

PRESENTATIONS:

1. **X. Ni**, S. A. Kartazayeva, and R. R. Alfano, “Polarization memory in the backscattering of light from turbid media,” CLEO/QELS, May 22, 2005, Baltimore, Maryland
2. **X. Ni**, C. Wang, X. Liang, M. Alrubauee, and R. R. Alfano, “Supercontinuum interference from Fresnel diffraction caused by periodic filamentation,” CLEO/QELS, May 22, 2005, Baltimore, Maryland

3. **X. Ni**, Q. R. Xing, W. Cai, and R. R. Alfano, “Free-space optical propagation of pulse coded data stream,” The 87th OSA Annual Meeting, Oct. 5, 2003, Tucson, Arizona
4. **X. Ni** and R. R. Alfano, “Wireless optical propagation with pulsed coded data streams,” Wave Scattering in Complex Media, June 2002, Corsica, France.

BIBLIOGRAPHY

CHAPTER 1

1. M. P. Silverman, *Waves and grains* (Princeton U.P., Princeton, NJ,1998) pp.288.
2. Nelson A. Logan, *Survey of some early studies of the scattering of plane waves by a sphere*, Selected papers on light scattering, Milton Kerker, editor, pp.3-15(1988).
3. L. Rayleigh, Phil. Mag. **41**, 447 (1871).
4. G. Mie, Ann. Phys. **25**, 377 (1908).
5. J. A. Stratton, *Electromagnetic Theory* (McGraw-Hill, New York, 1941).
6. D. T. Thomas, *Scattering by plasma and dielectric bodies*, Ph.D. dissertation, Ohio State University, Columbus, Antenna Lab. Rept., no. 1116 (1962).
7. D. Atlas and K. M. Glover, "Backscattering by dielectric spheres with and without metal caps", Proc. Inter-Disciplinary Conf. Electromagnetic scattering (Potsdam, N. Y., 1962).
8. R. G. Kouyoumjian, L. Peters, Jr., and D. T. Thomas, IEEE Trans. Ant. Prop., **AP-11**, 690 (1963).
9. H. Inada, Appl. Opt. 13, 1928 (1974).
10. H. Inada, Appl. Opt. **12**, 1516 (1973).
11. H. Inada, M. A. Plonus, IEEE Trans. Ant. Prop. **AP-18**, 89 (1970).
12. G. N. Watson, Proc. Roy. Soc. London, **A95**, 83 (1918).
13. H. Inada, M. A. Plonus, IEEE Trans. Ant. Prop. **AP-18**, 649 (1970).
14. P. S. Ray and J. J. Stephens, Radio Sci. **9**, 43 (1974).
15. J. Rheinstein, IEEE Trans. Ant. Prop. **AP-16**, 89 (1968).
16. R. A. Chevile and D. Grischkowsky, Appl. Phys. Lett. **67**, 1960 (1995).

17. R. A. Cheville, R. W. McGowan, and D. R. Grischkowsky, IEEE Trans. Ant. Prop. **45**, 1518 (1997).

18. R. R. Alfano and S. L. Shapiro, Phys. Rev. Lett. **24**, 592 (1970).

19. H. C. van de Hulst, *Light scattering by small particles* (Dover, New York, 1981).

20. M. Kerker, *The scattering of light and other electromagnetic radiation* (Academic, New York, 1969).

21. F. Bohren, D. R. Huffmann, *Absorption and scattering of light by small particles* (Wiley-Innterscience, New York, 1983).

22. M. I. Mishchenko, L. D. Travis, and A. A. Lacis, *Scattering, Absorption, and Emission of light by Small Particles* (Cambridge University Press, UK, 2002).

23. G. C. Stokes, Trans. Cambridge Philos. Soc. **9**, 399 (1852).

24. L. G. Henyey, J. L. Greenstein, The Astrophysical Journal, **93**, 70 (1941).

25. A. Ishimaru, Appl. Opt. **28**, 2210 (1989).

26. A. Ishimaru, *Theory and application of wave propagation in random media* (NJ:IEEE Press, Piscataway, 1997).

27. P. M. Morse and H. Feshbach, *Methods of the theoretical physics* (McGraw-Hill, New York, 1953).

28. J. Crank, *The mathematics of diffusion* (Clarendon Press, Oxford, 1956).

29. W. Cai, M. Xu, M. Lax, and R. R. Alfano, Opt. Lett. **27**, 731 (2002).

30. M. Lax, V. Narayanamurti, and R. C. Fulton, "Classical diffusive photon transport in a slab", in Proc. Symp. on Laser Optics and Condensed Matter, Leningrad, June 1987, edited by J. L. Birman and H. Z. Cummins (Plenum, New York).

31. R. Garg, R. K. Prud'homme, A. Aksay, F. Liu, and R. R. Alfano, JOSA **15**, 932 (1998).

32. R. Garg, R. K. Prud'homme, A. Aksay, F. Liu, and R. R. Alfano, J. Mater. Res. 13, 3463 (1998).

33. K. M. Yoo, F. Liu, and R. R. Alfano, Phys. Rev. Lett. **64**, 2647 (1990).

34. W. Cai, M. Lax, and R. R. Alfano, Phys. Rev. E **61**, 3871 (2000).

35. W. Cai, M. Xu, and R. R. Alfano, Phys. Rev. E **71**, 041202 (2005).

CHAPTER 2

1. S. G. Demos and R. R. Alfano, Appl. Opt. **36**, 150 (1997).
2. S. G. Demos and R. R. Alfano, Opt. Lett. **21**, 161 (1996).
3. A. H. Hielscher, A. A. Eick, J. R. Mourant, and I. J. Bigo, Appl. Opt. **26**, 125 (1997).
4. B. D. Cameron, M. J. Rakovic, M. Mehrubeoglu, G. Kattawar, S. Rastegar, L. V. Wang, and G. Cote, Opt. Lett. **23**, 485 (1998).
5. S. R. Pal and A. I. Carswell, Appl. Opt. **24**, 3464 (1985).
6. X. Ni and R. R. Alfano, Appl. Opt. **42**, 6980 (2003).
7. R. Gans, Ann. Phys. (Leipzig) **75**, 1 (1925).
8. S. Chandrasekhar, *Radiative Transfer* (Clarendon, Oxford, 1950).
9. A. D. Kim and M. Moscoso, SIAM J. Comput. Sci. **23**, 2075 (2002).
10. Ambirajan, D. C. Look, J. Quant. Spectrosc. Radiat. Transfer. **58**, p171-192 (1997).
11. W. Cai, M. Lax, R. R. Alfano, Phys. Rev. E. **61**, 3871 (2000).
12. W. Cai, M. Lax, R. R. Alfano, Phys. Rev. E. **63**, 016606 (2000).
13. W. Cai, M. Xu, R. R. Alfano, Phys. Rev. E **71**, 041202 (2005).
14. H. C. van de Hulst, *Light Scattering by Small Particles* (Dover Publications, New York, 1981).

15. J. W. Hovenier, C. V. M. van der Mee, Astron. Astrophys. **128**, 1(1983).
16. I. Kuščer, M. Ribarič, Optica Acta **6**, 42 (1959).
17. W. A. de Rooij and C. C. A. H. van der Stap, Astron. Astrophys. **131**, 237 (1984).
18. E. P. Wigner, *Group theory and its application to the quantum mechanics of atomic spectra* (Academic Press, New York, 1959).
19. B. M. Brink, G. M. Satchler, *Angular Momentum* (Clarendon Press, Oxford, 1962).
20. M. I. Mishchenko, L. D. Travis, A. A. Lacis, *Scattering, absorption, and emission of light by small particles* (Cambridge University Press, Cambridge, 2002).

CHAPTER 3

1. L. Wang, P. P. Ho, G. Liu, G. Zhang, and R. R. Alfano, Science **253**, 769 (1991).
2. D. Huang, E. A. Swanson, C. P. Lin, J. S. Schuman, W. G. Stinson, W. Chang, M. R. Hee, T. Flotte, K. Gregory, C. A. Puliafito, and J. G. Fujimoto, Science **254**, 1178 (1991).
3. M. A. O'Leary, D. A. Boas, B. Chance, and A. G. Yodh, Opt. Lett. **20**,426 (1995).
4. Y. Guo, H. E. Savage, F. Liu, S. P. Schantz, P. P. Ho, and R. R. Alfano, Proc. Natl. Acad. Sci. **96**, 10854-10856 (1999).
5. A. Schmidt, R. Corey, and P. Saulnier, Opt. Lett. **20**, 404 (1995).
6. B. R. Masters, A. Kriete, and J. Kukulies, Appl. Opt. **32**, 592 (1993).
7. P. Clemenceau, A. Dogariu, J. S. Stryjewski, *Polarization active imaging*, in *Laser Radar Technology and Applications V*, G. W. Kamerman, U. N. Singh, C. H. Werner, and V. V. Molebny, Eds., Proc. SPIE **4035**, 401 (2000).
8. P. Y. Gerligand, M. H. Smith, R. A. Chipman, Opt. Express **4**, 420 (1999).
9. S. G. Demos, R. R. Alfano, Appl. Opt. **36**, 150 (1997).

10. S. P. Morgan, M. E. Ridgway, Opt. Express **7**, 395 (2000).

11. G. D. Lewis, D. L. Jordan, and P. J. Roberts, Appl. Opt. **38**, 3937 (1999).

12. G. D. Gilbert, J. C. Pernicka, Appl. Opt. **6**, 741 (1967).

13. F. C. MacKintosh, J. X. Zhu, D. J. Pine, D. A. Weitz, Phys. Rev. B. **40**, 9342 (1989).

14. E. E. Gorodnichev, A. I. Kuzovlev, and D. B. Rogozkin, JETP Lett. **68**, 22 (1998).

15. D. Bicout, C. Brosseau, A. S. Martinez, and J. M. Schmitt, Phys. Rev. E **49**, 1767 (1994).

16. A. D. Kim, M. Moscoso, Opt. Let. **27**, 1589 (2002).

17. R. R. Alfano and X. Ni, "Methods to improve backscattering imaging through large particle suspensions using circular polarization memory", U.S. Patent Application Serial No. #60/675,479 (Provisional patent application).

CHAPTER 4

1. D. Killinger, Opt. Photon. News **13** 10, 36 (2002).

2. A. Acampora, Scientific American, 49 (July, 2002).

3. K. M. Yoo and R. R. Alfano, Opt. Lett. **15,** 320 (1990).

4. L. Wang, P. P. Ho, C. Liu, G. Zhang, and R. R. Alfano, Science **253,** 769 (1991).

5. J. J. Dolne, K. M. Yoo, F. Liu and R. R. Alfano, Laser Life Sci. **6**, 131 (1994).

6. H. Horinaka, K. Hashimoto, K. Wada, Y. Cho, and M. Osawa, Opt. Lett. **20,** 1501 (1995).

7. L. Wang, P. P. Ho, X. Liang, H. Dai, and R. R. Alfano, Opt. Lett. **18**, 241 (1993).

8. K. C. Young, *Microphysical Processes in Clounds* (Oxford University Press, New York, 1993).

9. Kuo-Nan Liou, *An Introduction to Atmospheric Radiation* (Academic Press, New York, 1980).

10. I. Kim, R. Stieger, J. A. Koontz, C. Moursund, M. Barclay, P. Adhikari, J. Schuster, E. Korevaar, R. Ruigrok, and C. DeCusatis, Opt. Eng. **37** 12, 3143 (1998).

11. X. H, Ni, Q. R. Xing, W. Cai, and R. R. Alfano, Opt. Lett. **28**, 343 (2003).

12. K. M. Yoo, Feng Liu, and R. R. Alfano, Opt. Lett. **16**, 1068 (1991).

13. A. Sea, V. Petričević, and R. R. Alfano, Opt. Lett.**18**, 891 (1993).

14. A. D. Kim and M. Moscoso, Phys. Rev. E. **64** 026612 (2001).

15. E. E. Gorodnichev, A. I. Kuzovlev, and D. B. Rogozkin, JETP Lett., **68,** 22 (1998).

16. S. G. Demos and R. R. Alfano, Opt. Lett. **21,** 161 (1996).

17. S. P. Morgan, M. P. Khong, M. G. Somekh, Appl. Opt. **36,** 1560 (1997).

18. M. J. Rakovic, G. W. Kattawar, M. Mehrubeoglu, B. D. Cameron, L. V. Wang, S. Rastegar, G. L. Cote, Appl. Opt. **38,** 3399 (1999).

19. G. Yao, L. V. Wang, Opt. Lett. **24,** 537 (1999).

20. J. M. Schmitt, A. H. Gandjbakhche, and R. F. Bonner, Appl. Opt. **31,** 6535 (1992).

21. W. Cai, M. Lax, R. R. Alfano, Phys. Rev. E **63,** 016606 (2001).

22. Smith, F., The Infrared and Electro-Optical Systems Handbook *Atmospheric Propagation of Radiation*, Vol. 2, SPIE Press (1993).

23. E. P. Zege, A. P. Ivanov, and I. L. Katsev, *Image transfer through a scattering medium* (Springer-Verlag, Berlin-Heidelberg, 1991).

CHAPTER 5

1. L. Brillouin, *Wave propagation and group velocity* (Academic, New York, 1960).
2. A. Sommerfeld, Ann. Phys. (Leipzig) **44**, 177 (1914).
3. L. Brillouin, Ann. Phys. (Leipzig) **44**,203 (1914).
4. H. G. Baewald, Ann. Phys. (Leipzig) **7**, 731(1930).
5. J. L. Birman and M. J. Frankel, Opt. Commun. 13, 303 (1975).
6. M. J. Frankel and J. L. Birman, Phys. Rev. A **15**, 2000 (1977).
7. T. A. Weber and D. B. Trizna, Phys. Rev. **144**, 277 (1966).
8. D. L. Johnson, Phys. Rev. Lett. **41**, 417 (1978).
9. E. Varoquaux, G. A. Williams, and O. Avenel, Phys. Rev. **B** 34,7617 (1986).
10. P. Pleshko and I. Palócz, Phys. Rev. Let. **22**, 1201 (1969).
11. S. -H. Choi and U. Österberg, Phys. Rev. Lett. **92**, 193903 (2004) ; Also see, S. Chasteen, "Light wave outlasts itself", Phys. Rev. focus, **13** (12 May 2004); J. R. Minkel, "Splinters of light", Science News (20 May 2004); T. M. Roberts, Phys. Rev. Lett. **93**, 269401 (2004); R. R. Alfano, J. L. Birman, X. Ni, M. Alrubaiee, and B. B. Das, Phys. Rev. Lett. **94**, 239401 (2005).
12. J. D. Jackson, *Classical Electrodynamics* 2nd ed. (Wiley, New York, 1975).
13. K. E. Oughstun, and J. E. K. Laurens, Radio Science **26**, 245 (1991).
14. U. J. Gibson, and U. L. Österberg, Opt. Express **13**, 2105 (2005).
15. R. R. Alfano, Interaction of picosecond laser pulses with matter (Ph.D. dissertation, GTE Laboratories, Bayside, New Yok); R. R. Alfano, J. I. Gersten, G. A. Zawadzkas, and N. Tzoar, Phys. Rev. A **10**, 698 (1974).
16. K. E. Oughstun, Proc. IEEE **79**, 1379 (1991).

17. A. Karlsson and S. Rikte, J. Opt. Soc. Am. A **15**, 487 (1998).

18. N. C. Nielsen, S. Linden, J. Kuhl, J. Förstner, A. Knorr, S. W. Koch, and H. Giessen, Phys. Rev. B **64**, 245202 (2001).

19. J. Aaviksoo, J. Kuhl, and K. Ploog, Phys. Rev. A **44**, R5353 (1991).

20. M. Sakai, R. Nakahara, J. Kawase, H. Kunugita, and K. Ema, Phys. Rev. B **66**, 033302 (2002).

21. D. Grischkowsky, S. Keiding, M. van Exter, and Ch. Fattinger, J. Opt.Soc. Am. B **7**, 2006 (1990).

22. X. -C. Zhang, B. B. Hu, J. T. Darrow and D. H. Auston, Appl. Phys. Lett. **56**, 1011 (1990).

23. M. van Exter, C. Fattinger, and D. Grischkowsky, Appl. Phys. Lett. **55**, 337 (1989).

24. Q. Wu and X.-C Zhang, Appl. Phys. Lett. **70**, 1784 (1997).

25. H. J. bakker, G. C. Cho, H. Kurz, Q. Wu, and X.-C. Zhang, J. Opt. Soc. Am. B **15**, 1795 (1998).

26. A. Nahata, A. S. Weling, and T. F. Heinz, Appl. Phys. Lett. **69**, 2321 (1996).

27. T. Hattori, Y. Homma, A. Mitsuishi, and M. Tacke, Opt. Commun. **7**, 229 (1973).

28. S. Chu and S. Wong, Phys. Rev. Lett. **48**, 738 (1982); Also see comment: A. Katz and R. R. Alfano, Phys. Rev. Lett. **49**, 1292 (1982); and reply: S. Chu and S. Wong, Phys. Rev. Lett. **49**, 1293 (1982).

29. R. Y. Chiao, Phys. Rev. A 48, R34 (1993).

30. S. L. McCall and E. L. Hahn, Phys. Rev. **183**, 457 (1969).

31. M. D. Crisp, Phys. Rev. A 1, 1604 (1970).

32. M. D. Crisp, Phys. Rev. A 5, 1365 (1972).

33. F. A. Hopf, G. L. Lamb, C. K. Rhodes, and M. O. Scully, Phys. Rev. A **3**, 758 (1971).

34. O. Avenel, E. Varoquaux, and G. A. Williams, Phys. Rev. Lett. **53**, 2058 (1984).

CHAPTER 6

1. R. R. Alfano and S. L. Shapiro, Phys. Rev. Lett. **24**, 592 (1970).
2. R. R. Alfano and S. L. Shapiro, Phys. Rev. Lett. **24**, 584 (1970).
3. R. R. Alfano and S. L. Shapiro, Phys. Rev. Lett. **24**, 1217 (1970).
4. R. R. Alfano and S. L. Shapiro, Scientific American, **228**, no. 6, 42-55, 58, 60, (1973).
5. R. R. Alfano, *The Supercontinuum Laser Source* (New York: Springer-Verlag, 1989).
6. Y. Takushima and K. Kikuchi, IEEE Photon. Technol. Lett., **11**, 322 (1999).
7. A. Braun, G. Korn, X. Liu, D. Du, J. Squier, and G. Mourou, Opt. Lett. **20**, 73 (1995).
8. P. Rairoux, H. Schillinger, S. Niedermeier, M. Rodriguez, F. Ronneberger, R. Sauerbrey, B. Stein, D. Waite, C. Wedekind, H. Wille, and L. Wöste, and C. Ziener, Appl. Phys. B **71**, 573 (2000).
9. Q. Luo, W. Liu, and S. L. Chin, Appl. Phys. B **76**, 337 (2003).
10. G. Méchain, J. Kasparian, J. Yu, S. Frey, E. Salmon, and J-P. Wolf, Appl. Phys. B. 78, 535 (2004).
11. A. Baltuška, M. Uiberacker, E. Goulielmakis, R. Kienberger, V. S. Yakovlev, T. Udem, T. W. Hänsch, F. Krausz, IEEE JSTQE **9**, 972 (2003).
12. I. Zeylikovich and R. R. Alfano, Appl. Phys. B **77**, 265 (2003).
13. K. Cook, A. K. Kar, and R. A. Lamb, Appl. Phys. Lett. **83**, 3861 (2003).
14. S. L. Chin, S. Petit, W. Liu, A. Iwasaki, M. –C. Nadeau, V. P. Kandidov, O. G. Kosareva, K. Yu. Andrianov, Opt. Comm. **15**, 329 (2002).

15. W. Watanbe and K. Itoh, Jpn. J. Appl. Phys. **40**, 592 (2001).

16. F. Courvoisier, V. Boutou, J. asparian, E. Salmon, Appl. Phys. Lett. 83, 213 (2003).

17. H. Wille, M. Rodriguez, J. Kasparian, D. Mondelain, J. Yu, A. Mysyrowicz, R. Sauerbrey, J-P. Wolf and L. Wöste, Eur. Phys. J. AP. 20, 183 (2002).

18. G. Méchain, A. Couairon, M. Franco, B. Prade and A. Mysyrowicz, Phys. Rev. Lett. **93**, 035003 (2004).

19. H. Schroeder, J. Liu, and S. L. Chin, Opt. Express **12**, 4789 (2004).

20. K. Cook, R. McGeorge, A. K. Kar, M. R. Taghizadeh, and R. A. Lamb, Appl. Phys. Lett. **86**, 021105 (2005).

21. G. Fibich, S. Eisenmann, B. Ilan and A. Zigler, Optics Letters **29**, 1772 (2004).

22. A. D. Dubietis, G. Tamošauskas, G. Fibich and B. Ilan, Opt. Lett. **29**, 1126 (2004).

23. R. Y. Chiao, E. Garmire, and C. H. Townes, Phys. Rev. Lett. **13**, 479 (1964).

24. P. L. Kelley, Phys. Rev. Lett. **15**, 1005 (1965).

25. M. Centurion, Y. Pu, M. Tsang, and D. Psaltis, Phys. Rev. A **71**, 063811 (2005).

26. R. R. Alfano, "Interaction of picosecond laser pulses with matter", GTE Technical Report TR 72-330. Published as Ph.D. thesis at New York University (1972).

27. M. Born and E. Wolf, *Principles of Optics*, 6th ed. (Oxford: Pergamon Press, 1980).

28. K. Cook, A. K. Kar, and R. A. Lamb, Opt. Express **13**, 2025 (2005).

29. X. Ni, C. Wang, X. Liang, M. Alrubaiee and R. R. Alfano, IEEE *JSTQE* **10**, 1229 (2004).

30. A. J. Campillo, J. E. Pearson, S. L. Shapiro, and N. J. Terrell, Jr., Appl. Phys. Lett. **23**, 85 (1973).

31. J. A. Fleck, Jr. and C. Layne, Appl. Phys. Lett. **22**, 467 (1973).

32. A. J. Campillo, S. L. Shapiro, and B. R. Suydam, Appl. Phys. Lett. **23**, 628 (1973).

33. Y. R. Shen, *The principles of nonlinear optics* (Wiley, New York, 1984).

Appendix A

1. W. Cai, M. Lax, R. R. Alfano, Phys. Rev. E. **63**, 016606 (2000).
2. W. Cai, M. Xu, R. R. Alfano, Phys. Rev. E **71**, 041202 (2005).
3. J. W. Hovenier, C. V. M. van der Mee, Astron. Astrophys. **128**, 1 (1983).
4. R. P. Feynman, Phys. Rev. **84**, 108 (1951).
5. F. Dyson, *ibid*. **75**, 486 (1949).
6. S. H. Ma, *Statistical Mechanics* (World Scientific, Philadephia, 1985).
7. M. G. Kendall and A. Stuart, *The advanced theory of statistics* 3rd ed. (Hafner, New York, 1969), Vol.1.
8. B. M. Brink, G. M. Satchler, *Angular Momentum* (Clarendon Press, Oxford, 1962).
9. M. Gel'fand, Z. Ya. Sapiro, Amer. Math. Soc. Translations **2**, 207 (1956).